DYNAMICS OF RIGID FIBERS IN A PLANAR CONVERGING CHANNEL

A Dissertation
Presented to the
Academic Faculty

by

Matthew L. Brown

In Partial Fulfillment
of the Requirements for the Degree
Doctor of Philosophy

School of Chemical and Biomolecular Engineering
Georgia Institute of Technology
March 29, 2005

DYNAMICS OF RIGID FIBERS IN A PLANAR CONVERGING CHANNEL

Approved By:

Professor Jeff Empie, Committee chair
School of Chemical and Biomolecular Engineering
Georgia Institute of Technology

Professor Cyrus Aidun, Advisor
School of Mechanical Engineering
Georgia Institute of Technology

Professor Larry Forney
School of Chemical and Biomolecular Engineering
Georgia Institute of Technology

Professor Mostafa Ghiaasiaan
School of Mechanical Engineering
Georgia Institute of Technology

Professor Victor Breedveld
School of Chemical and Biomolecular Engineering
Georgia Institute of Technology

Date Approved: 03/29/2005

ACKNOWLEDGMENTS

There are many people that have contributed to the successful completion of this work. First of all, I would like to express my sincere gratitude for the diligent assistance of my advisor, Dr. Cyrus Aidun, in helping me complete my doctorate degree. He has shown continued support and provided valuable advice though out my graduate studies. I would also like to give thanks to Dr. Mehran Parsheh, my lab-mate, for sharing his expertise in both fluid mechanics and experimental techniques. I have learned a great deal from Dr. Parsheh and his assistance has proven invaluable to the successful completion of this work. Special thanks to Dr. Barry Crouse, whose guidance and support were instrumental in me coming coming to Atlanta and achieving this degree. A special note of appreciation to my predecessor Chang Park, who has given me much assistance early on with the design and construction of the flow facility.

I would also like to extend my gratitude for the technical input and guidance of the rest of my thesis reading committee as well.

I am also grateful for the friends that I have made during my studies: Thank you Mehran Parsheh, Eric Schmidt, Chang Park, John Xu, Venkata Bandhakavi, Jagbir Hooda, Paul McKay, Akay Islek, and Gorkem Bedir for making my time here enjoyable.

TABLE OF CONTENTS

LIST OF TABLES

LIST OF FIGURES

xiv

NOMENCLATURE

a_{ij}	Second order orientation tensor
a_{ijkl}	Fourth order orientation tensor
$a_{ijkl,0}$	Initial fiber orientation tensor
a_p	Fiber aspect ratio
b	Grid bar width
B	Effective bending rigidity
c_o	Constant based on grid geometry
c_1	Empirical constant
C	Local contraction ratio
C_e	Equivalent contraction ratio
d	fiber diameter
D_r	Rotational diffusion coefficient
$\overline{D_r}$	Dimensionless rotational diffusion parameter
D_t	Translational diffusion coefficient
e_{ijkl}	Closure approximation error
E	Symmetric mean velocity gradient tensor
h	Local contraction height
h_0	Inlet contraction height
I	Second moment of fiber area
K	Turbulent kinetic energy
K_p	Production of turbulent kinetic energy
l	Downstream distance from the grid
l_r	Grid position

L	Fiber half length
m	index of refraction
M	Mesh size
n	Number density of fibers
$\mathbf{p}$	Unit orientation vector
$\dot{\mathbf{p}}$	Time rate of change of orientation vector
P_{ij}	turbulent energy production
$\mathrm{Pe_r}$	Rotational Peclet number
R	Dimensionless Reynolds number
R_{11}	Autocorrelation coefficient
Re	Macroscopic Reynolds number
$\mathrm{Re_f}$	Microscopic Reynolds number
St	Stokes number
t	time
u'_1, u'_2, u'_3	Fluctuating velocity components
$u'_{1,0}, u'_{2,0}, u'_{3,0}$	Inlet fluctuating velocity components
u_1, u_2, u_3	Instantaneous velocity components
U_1, U_2, U_3	Mean velocity components
$U_{1,p}, U_{2,p}, U_{3,p}$	Mean velocity components based on potential flow
$U_{1,0}$	Inlet mean streamwise velocity component
w	Contraction width
x_1, x_2, x_3	Position components
Y	Accumulative fiber fraction
Z	Dimensionless fiber bending parameter
β	Contraction half angle
χ	Index of refraction
δ_{ij}	Kronecker delta
ϵ	Dimensionless acceleration
ϵ_t	Dissipation rate of turbulent energy

ϕ	Fiber orientation angle
ϕ_c	Fiber volume fraction
Γ	Gamma function
λ	Hydrodynamic interaction coefficient
Λ	Integral length scale
μ	Fluid dynamic viscosity
μ_{eff}	Effective suspension viscosity
μ_{fiber}	fiber phase viscosity
ν	Kinematic viscosity
θ	Fiber orientation angle
ρ	Fluid density
ρ_f	Fiber density
σ	Dimensionless time of flight
τ	Integral time scale
τ_a	Flow time constant
τ_b	Burst time
τ_p	Particle time constant
ω	Component of mean vorticity
ω_0	Dimensionless frequency constant
ω_i'	Component of fluctuating vorticity
Ω	Antisymmetric mean velocity gradient tensor
ψ	Orientation distribution function
Υ	Adjustable parameter
ϖ	Shape factor

SUMMARY

The influence of turbulence on the orientation state of a dilute suspension of stiff fibers at high Reynolds number in a planar contraction is investigated. High speed imaging and LDV techniques are used to quantify fiber orientation distribution and turbulent characteristics. A nearly homogenous, isotropic grid generated turbulent flow is introduced at the contraction inlet. Flow Reynolds number and inlet turbulent characteristics are varied in order to determine their effects on orientation distribution. The orientation anisotropy is shown to be accurately modelled by a Fokker-Planck type equation. Results show that rotational diffusion is highly influenced by inlet turbulent characteristics and decays exponentially with convergence ratio. Furthermore, the effect of turbulent energy production in the contraction is shown to be negligible. Also, the results show that the flow Reynolds number has negligible effect on the development of orientation anisotropy. It was concluded that inertia induced fiber motion played a negligible role in the experiments.

CHAPTER 1

INTRODUCTION

In many industrial processes, the behavior and orientation of fibers in a turbulent flow affects the transport, rheology, and turbulent characteristics of suspensions. Fibers suspended in flow undergo mean motion due to the mean fluid velocity, random motion due to the fluctuating component of fluid velocity and inertia driven motion. The resulting change in the suspension microstructure can have a significant effect on the material's bulk properties. In the paper industry, mechanical properties of manufactured paper are known to be anisotropic due to the anisotropic orientation of fibers induced by the flow kinematics while passing through a planar contraction with flat walls. The degree of fiber orientation anisotropy has a significant impact on paper quality. Defects due to fiber orientation anisotropy, such as paper curl, result in paper jamming in copier machines and printers. Therefore, in addition to the fundamental importance of understanding the influence of turbulence on fiber orientation, this problem is of practical interest in the paper manufacturing process.

The objective of this work is to investigate the effect of turbulence on the rotational diffusion of an infinite-dilute suspension of stiff fibers in a planar contraction, the

1

idealized version of systems used in manufacturing paper and other fiber composite webs. The approach is to carry out turbulence measurements and fiber visualization to couple the effect of turbulence on fiber orientation. Experiments are designed such that the influence of particle-particle interactions and fiber inertia on fiber dynamics becomes negligible.

Nearly isotropic homogeneous turbulent flow is introduced at the inlet of the converging channel. It is known that integral time scale and normal Reynolds stress components are important turbulent parameters to characterize the effect of turbulence on the rotational diffusion of fibers. These turbulent characteristics may be altered by changing the geometry of the flow conditioning section and the contraction geometry itself. In order to investigate the effect of turbulent flow characteristics, the turbulent intensity at the contraction inlet is varied by adjusting the position of the grid relative to the inlet. Since the turbulent intensity decays in the contraction and eventually the flow becomes nearly laminar, this approach provides an opportunity to examine the effect of turbulence on dynamics of fiber orientation.

To understand the impact of turbulence on orientation anisotropy requires measurement of orientation at different streamwise positions in the contraction with clearly defined turbulent conditions at the inlet and knowledge of turbulent flow variations along the contraction.

We have predicted flow induced orientation of a dilute fiber suspension for arbitrary contraction shape for Re of $O(10^5)$. Analogous to suspension flows with fiber-fiber interaction and Brownian motion, a Fokker-Planck type equation is shown

to accurately model the orientation state of fibers in turbulent nonhomogenous flow. To solve this equation, a relation for rotational diffusion coefficient, D_r, is required. Since the influence of turbulence on orientation anisotropy can be expressed by an orientational diffusion coefficient, in this thesis we also examine the factors affecting this coefficient. Fiber orientation in a contraction with flat walls is measured to determine this parameter. In order to obtain reliable average data, the orientation state of a large population of fibers is quantified and the development of the orientation distribution function inside the converging channel is obtained. These measurements show that the orientation distribution function can be accurately measured using image analysis techniques. Experiments are carried out in a closed flow loop at the Georgia Institute of Technology using water as the medium. LDV is used to quantify the mean and fluctuating velocity field.

CHAPTER 2

LITERATURE REVIEW

The mean and fluctuating velocity field and suspension parameters (*i.e.* fiber geometry, carrier fluid viscosity, fiber concentration, fiber density, etc.) are known to influence fiber orientation state in suspension flow.

The prediction of flow-induced alignment of a fiber suspension is of interest in many high volume industrial processes including fiber-reinforced composites, polymer extrusions, compression molding and paper manufacture. The development of suspension microstructure based on flow kinematics is among the primary concerns in understanding complex suspension flow. Due to the practical importance of these predictions, dilute suspension theory of rigid, neutrally buoyant, axisymmetric particles suspended in Newtonion fluid subjected to homogenous simple shear flows is well understood. However, many practical suspension flows are turbulent. Currently, the influence of turbulence on fiber dynamics is not well understood. Below is a brief review of dilute suspension theory focusing on suspension flow in axisymmetric and planar contractions.

2.1 Flow induced orientation of inertialess fibers

The focus of this study is on the dynamics and orientation of a dilute fiber suspension in turbulent contraction flow. Fiber motion in dilute suspension flow is controlled by surface and body forces on the fiber. In such dilute systems, $(nL)^3 << 1$, and, $\phi_c << 1$ where n is the number density of fibers, L is the fiber half length, and ϕ_c is the fiber volume fraction. Clearly, no suspension flow is completely dilute with absolutely no particle-particle collisions or interactions taking place. However, suspensions in the dilute regime display similar behavior, which differs from the behavior of semi-dilute, and concentrated suspensions (Crowe 1982). According to Doi & Edwards (1978), the transition from an infinite-dilute non-interacting suspension to a semi-dilute interacting suspension occurs at $\phi_c a_p^2 = O(1)$, where a_p is the ratio of fiber length to diameter. In order to investigate the dynamics of suspensions in turbulent flow, it is first necessary to understand the physics governing the motion of fibers in laminar Stokes flow.

The shape of a fiber may be approximated as a large aspect ratio ellipsoid. The dynamics and orientation of an isolated inertialess ellipsoid in the dilute regime in homogenous flow is given by Jeffery (1922). Jeffery's relation governs the motion of a rigid ellipsoidal particle suspended in an incompressible Newtonian fluid, and forms the basis of most of the research performed in this field. The dynamics and orientation of an ellipsoid in a homogeneous flow field, (i.e. the mean velocity gradient is constant in all directions) can be obtained from Jeffery's relation and its generalization to any axisymmetric particle by Brenner (1964). An isolated inertialess ellipsoid in

simple shear flow rotates in a periodic orbit while the center of mass translates with the bulk flow. The period or rotation is a function of aspect ratio, a_p and shear rate, while the orbit depends on the initial orientation of the ellipsoid relative to the shear plane. Also, fibers in an extensional flow field will tend to orient along the principal axis of strain. In the Jeffery's analysis it is assumed that the particle size is much smaller than the length scale of the constant gradient flow. Thus, the disturbances produced by the particle cannot affect the bulk flow motion. The particle Reynolds number must be small implying either very slow flow or very small particle. Jeffery's equation gives the physical behavior of dilute inertialess suspension flows in which $nL^3 << 1$, where L denotes the fiber half length and n the fiber number density. However, it may not predict the behavior of semi-dilute suspension flow where the fibers are hydrodynamically coupled and the flow rheology is non-Newtonian. Visualization of rigid fibers in Taylor-Couette flow showed that isolated inertialess fibers rotate in the same orbit indefinitely, as predicted by Jeffery. However, Jeffery's theory overpredicted the period of rotation, suggesting that the relation be modified to account for different particle shapes

The rotation of rigid spheres in this flow agreed well with predictions by Jeffery. Several investigators have extended Jeffery's solution to consider the effect of different particle shapes on particle motion in various homogenous flows. (i.e. Okagawa & Mason, 1973 and Goldsmith & Mason, 1967). Chaffey, Takano & Mason, 1965 derived the angular velocity of a spheroid in a Newtonian fluid subjected to slow two-dimensional shear flow. The analytical solution agreed quantitatively with

experimental results.

The above investigations developed rheological theory for a specific particle shape and flow (i.e. simple shear and extensional flows). Brenner (1974) provided a general method to determine the angular velocity of any axisymmetric particle in arbitrary simple shear flow. The rheology of these suspensions is expressed in terms of the volume fraction of suspended particles, the carrier fluid viscosity, and five scalar material constants representing particle shape. The period of particle rotation in simple shear flow is directly proportional to the particle aspect ratio, and inversely proportional to the shear rate and shape factor, β.

Jeffery's relation is a steady state solution of particle orientation. However, suspension flow is transient in nature. An initially random orientation state subjected to simple shear experiences damped oscillations which eventually lead to an equilibrium distribution (Okagawa, Cox & Mason, 1973). This damping is attributed to difference in particle shape and particle-particle interactions. Vincent & Agassant (1986) and Folgar & Tucker (1984) investigated the validity of existing models and the factors affecting fiber behavior.

Givler (1981) was the first to provide a numerical scheme for the solution of Jeffery's orientation equations for isolated ellipsoidal particles suspended in flow with non-uniform velocity gradients. Local velocity gradients were used to solve the Stokes equation along the streamlines to predict planar orientation angle. Orientation development is given as the time rate of change of the orientation angles ϕ , and θ for planar and three-dimensional orientation. Pittman & Kasiri (1992) used a different

approach to modify Jeffery's solution for non-homogeneous flows. They evaluated the drag forces parallel and transverse to the particle axis by using the first approximation of Batchelor's (1971) slender body theory. The rotational and translational velocities of fibers are given for arbitrary Stokes flow.

The most general description of fiber orientation state is the orientation distribution function, ψ. An exact evolution equation of orientation distribution function may be used to evaluate the orientation field. Advani & Tucker (1987) and Akbar & Altan (1992) presented an analytical technique to describe the orientation behavior of a large number of non-interacting fibers in two-dimensional homogeneous Stokes flow. The two-dimensional rotation rate of a slender fiber is given as a function of fiber aspect ratio and mean velocity gradients. Thus, fiber orientation in Stokes flow can be determined at any instant given initial fiber orientation, fiber geometry, and mean velocity gradients are known. This technique was then used to evaluate orientation behavior of a large number of fibers starting from different initial orientations. An orientation distribution function was evaluated by considering the orientation of the large number of fibers at a given point downstream.

2.2 Flow induced microstructure and rheology of dilute suspensions

It is well known that the hydrodynamic coupling between fibers leads to non-newtonian flow behavior with increasing ϕ_c. The bulk stresses created by the presence of fibers depends on the orientation state of the suspension. Suspension viscosity becomes anisotropic when fibers are preferentially aligned in one direction. Fortunately,

the prediction of suspension microstructure and rheology of a dilute suspension of inertialess fibers from relevant suspension parameters is possible.

The preferential alignment of fibers in one direction changes the suspensions bulk properties and makes the transport tensors anisotropic. Several anisotropic constitutive models are available to predict suspension microstructure and rheology as a function of flow kinematics and relevant suspension parameters (*i.e.* fiber geometry, carrier fluid viscosity, fiber concentration, fiber density, etc.). Batchelor (1970) was the first to model the influence of relevant suspension parameters (i.e. ϕ_c, ψ, and L) on the average transport behavior of a dilute inertialess fiber suspension. His analysis is based on replacing the viscous forces from a suspended body by a line distribution of stokelets. This approach, known as slender body theory, is often used as a starting point for the analysis of two-phase flow problems. The bulk average stress of a dilute fiber suspension is given by

$$\sigma_s = \mu_{fiber}(< \mathbf{pppp} > -\frac{1}{3}\delta_{i,j} < \mathbf{pp} >) : \mathbf{E} + 2\mu\mathbf{E}, \tag{1}$$

where $\mathbf{p}$ is the unit fiber orientation vector, $\mathbf{E}$ is the mean rate of strain tensor, δ is the unit tensor, μ is the fluid viscosity (Batchelor, 1971). The transport coefficient, μ_{fiber}, given by

$$u_{fiber} \approx \frac{4\pi\, nL^3\mu}{3\ln((4nL)^{1/2}/d)}, \tag{2}$$

represents the contribution of relevant suspension parameters to the average stress. The fiber viscosity is inversely proportional to the log of the fiber aspect ratio, a_p

$= L/d$ and d is the fiber diameter. This constitutive relation, known as the cell model, is based on the idea that at some distance from the fiber $nL^3 << 1$ and the fiber may be considered as surrounded by pure solvent. Therefore the average suspension properties must gradually change from those of screened fluid to purely viscous behavior as the distance from a fiber increases. Batchelor's model shows that orientation anisotropy alters the rheology of the fiber suspension and predicts high extensional viscosity for a suspension with fibers strongly aligned in the flow direction.

Lipscomb et. al. (1988) coupled the orientation distribution function, ψ, to the stress equation to investigate the behavior of a large number of fibers in suspension flow. They found that dilute fiber suspensions exhibit stresses in extension that are substantially larger than those in shear at the same deformation rates, leading to differences in flow of dilute suspensions versus the flow of the suspending fluid. Lipscomb developed a continuum theory for dilute suspensions of large aspect-ratio particles and applied the theory to flow of fiber suspensions through sudden contractions. Experiments with glass fibers in contractions showed good agreement with the model.

The above models use slender body theory to represent fiber hydrodynamic interactions. The limitation of slender body theory is that it does not account for short range lubrication forces. Consequently, these models are strictly valid only for dilute suspensions where neighboring fibers rarely come into close contact. In the semi-dilute regime , defined as $nL^3 >> 1$ and $\phi_c << 1$, fibers are likely to have many more close interactions. These short range interactions serve to reduce the amount of

orientation dispersion. Therefore, including these short-range forces in the analysis leads to an increase in the average stress of the suspension relative to the previous models. Measurements by Mewis & Metzner (1974) show that orientation dispersion increases with fiber concentration for $nL^3 < 40$, and then decreases slightly as the suspension approaches the semi-dilute regime. The above constitutive models are useful in predicting semi-dilute flow behavior. However, it is important to note that their accuracy depends on ϕ_c and the type of flow considered.

Shaqfeh and Koch (1990) investigated the orientation dispersion of a semi-dilute fiber suspension in extensional flow. Their model considered both long range hydrodynamic interactions and lubrication forces. The influence of short range interactions was based on an estimate of the number of fiber collisions due to translational and rotational motion. They found that short range interactions tended to orient fibers along the principal axis of strain. This model shows that the mean square displacement for a dilute and semi-dilute fiber suspension is $O(nL^3/\ln a_p^2$ and $O(\ln(nL^3)/nL^3)$, respectively. In the dilute regime, it was found that as the concentration increases the rate of dispersion increases. The dispersion rate decreased with increasing fiber concentration in the semi-dilute regime. It was also observed that fiber dispersion in a planar extensional flow is slightly anisotropic in the dilute regime. They found the dispersion in the transverse direction was larger than that in the extensional direction. Measurements by Mewis & Metzner show that highly oriented semi-dilute fiber suspensions have extensional viscosity up to one hundred times the fluid viscosity. Koch & Rahnamam (1995) have visualized the fiber orientation state of a semi-dilute

fiber suspensions in planar extensional flow. Results were in good agreement with the model of Shaqfeh & Koch. Cox & Brenner (1971) showed that suspensions of large aspect ratio prolate spheroids exhibit shear thickening behavior (i.e. the intrinsic viscosity increases with increasing shear rate) up to a critical shear rate at which the suspension reverts to shear thinning behavior. The normal stress of the suspension, σ, increases linearly up to a critical deformation rate, at which point it remains constant.

A rheological constitutive equation of state valid for both dilute and semi-dilute suspensions was developed by Dinh & Armstrong (1984). Their model is based on a continuous variation of the fiber orientation angle. Later, Shaqfeh & Fredricksson (1990) improved upon Dinh and Armstrong's model by providing higher order correction terms in the hydrodynamic stresses.

The above rheological models represent the orientation state with the orientation distribution function, ψ. The orientation distribution function provides the most general description of orientation state. However, numerical simulations of the evolution of ψ are computationally expensive. Therefore, it is desirable to use a more compact description of the fiber orientation state. Giesekus (1982) and Bretherton (1964) expressed Jeffery's solution in a more general form using a third rank shape tensor to facilitate numerical calculations of three-dimensional fiber orientation in complex geometries. Advani & Tucker (1987) show that even-order tensors give a concise description of ψ. The second- and fourth-order planar orientation tensors represent moments of the orientation distribution function. The diagonal components

of orientation tensor show the degree of the alignment and the off-diagonal terms represent the skewness of the orientation distribution function. Orientation distribution functions can be accurately reproduced given the orientation tensor components. However, higher order tensors lead to a increasingly accurate representation of ψ. The use of orientation tensors speeds up numerical simulations considerably. This approach allows for orientation predictions in more complex geometries and higher Reynolds number flows. The disadvantage of this approach is that the equations are no longer exact. For example, the evolution equation for the second order tensor contains an unknown fourth order tensor component. This equation may be closed by introducing a closure approximation which relates fourth-order tensor components to the lower-order tensor components.

A number of closure approximations have been put forth to predict the effect of flow field on fiber orientation using the orientation tensor approach.

Hand (1962) introduced a linear closure approximation based on the linear terms resulting from combining products of the second order tensor, a_{ij} and the unit tensor δ_{ij}. This expression is exact for weak flows with randomly distributed fibers. This model satisfies all the symmetry and projection properties of the second and fourth order orientation tensors. However, the model performs poorly at intermediate to highly aligned orientation states.

The quadratic closure approximation is one of the most widely used and simplest closure models. Doi (1981) represented the fourth order tensor by the dyadic product of two second order tensors. This expression is exact for strong flows where fibers

are uniformly aligned in one direction. The model is shown to be inadequate for orientation predictions for weak flows with random to intermediately aligned orientation state (Advani & Tucker 1990). This model does not satisfy all the symmetry conditions of the fourth order orientation tensor and only two of the six projection properties.

Additional closure approximations have been put forth seeking to improve the robustness of the linear and quadratic models. Hinch & Leal (1976) combined the desirable features of the linear and quadratic approximation to form a composite closure approximation which is exact for both limits of orientation state. The composite closure approximation fulfills two of the six symmetry properties and no projection properties. Following a similar approach, a hybrid closure approximation was introduced by Advani & Tucker, (1990). Strongly aligned fiber suspensions are represented well by the hybrid closure approximation. Verieye and Dupret (1993) based their natural closure approximation on a particular solution of fiber orientation dynamics.

Recently, a new set of closure approximations has been introduced for predicting flow-induced fiber orientation. It is known that an approximate fourth order orientation tensor must be orthotropic, that is the principal axis of the fourth order tensor must be the same as the principal axis of the second order tensor. The advantage of this approach is that the orthotropic orientation tensor becomes diagonal, where many of its components are zero. This result leads to a new set of orthotropic closure approximations for predicting flow-induced fiber orientation.

The symmetric orthotropic fourth order orientation tensor (i.e. $a_{ijkl} = a_{klij}$) has

nine independent scalar components. Considering additional symmetry and normalization requirements given by Cintra and Tucker (1995), the tensor is composed of three independent components. In other words, each principle fourth order component of the orthotropic orientation tensor is a function of two principle values of the second order tensor. Three functions may be chosen by linear interpolation between the limits of fiber orientation state to obtain a fitted orthotropic closure approximation. Another approach is to choose the functions which best fit the exact solution of the orientation probability distribution function for a particular flow. This results in an orthotropic smooth closure reported by Cintra and Tucker. Both the orthotropic smooth and fitted closures have all the symmetry and normalization properties of the exact fourth order tensor.

The advantage of this approach is that the solution is exact. However solving the exact ODF evolution equation is computationally expensive and its application is limited to relatively simple flows. Another approach to solve practical suspension flow problems involves numerically solving the coupled orientation tensor evolution equation, momentum and continuity equations, and a constitutive model for the non-Newtonian stresses generated by the suspension. Several researchers have investigated the coupled fiber orientation and flow problem in complex geometries using this approach.

Most of these studies utilized orientation tensors to represent the flow-induced orientation field. The orientation tensor approach leads to a more compact form of the orientation distribution function in order to facilitate the numerical solution of the

coupled fiber orientation and flow problem. Altan *et. al.* (1989) and Akbar & Altan (1992) utilized fiber orientation tensors to reduce the complexity of the constitutive expression. Recently, progress has been made in understanding the dynamics of inertial two-phase flows by finite element simulations.

Papanastasiou (1985) developed a numerical methodology for analyzing fiber orientation in complex flow fields. The motion of isolated fibers suspended in an incompressible Newtonian fluid was determined by solving the Navier-Stokes equation using a finite element technique. Orientation of fibers of varying aspect ratio in the presence of shear and extensional forces was solved for a two-dimensional free jet exiting an axisymmetric channel. Results showed that fibers located near the free surface tended to orient parallel to the free surface regardless of initial orientation inside the channel. Fibers located at the axial mid-line maintained their initial orientation inside the channel.

Chiba & Nakamura (1998) carried out numerical simulations and fiber orientation observations to investigate two-dimensional fiber orientation through a backwards-facing step channel. Suspension flow with high and low aspect ratio fibers in a Newtonian low Re flow were computed rigorously by coupling the flow field with fiber orientation. The model assumed that a fiber may be represented by an ellipsoid, no-slip conditions prevail at the surface of the fibers, the velocity field is only locally perturbed by the motion of the fiber, there is no interaction between fibers, motion is sufficiently slow that inertia forces are negligible, and the fiber translates with the fluid velocity. Large aspect-ratio fibers were found to completely align along the stream-

lines in recirculating flow. However, small aspect-ratio fibers aligned obliquely to the streamlines. In the core flow, the preferred angle lied obliquely to the streamlines in the central region of the channel. Furthermore, the fibers were less oriented and their preferred angles tilted away from the streamlines as the Reynolds number decreased. They found that predictions of flow induced suspension microstructure based on the single-phase fluid viscosity and deformation tensor could lead to significant error even at low ϕ_c.

Despite their potential drawbacks, the use of closure approximations is generally considered an acceptable method for prediction of complex suspension flows. In fact, nearly all simulations concerning practical suspension flows use closure approximations and do not consider the effect of the particles on the flow (i.e. Bay & Tucker, 1992 and Gupta & Wang, 1993).

Secondary factors including non-Newtonian flow behavior, fiber volume fraction and interaction between fibers often have a slight and sometimes negligible influence on the orientation state Altan & Rao (1995). The flow-induced orientation structure in short fiber reinforced injection moldings may be accurately predicted by using suspension theories developed for a non-Brownian, neutrally buoyant, rigid, and hydrodynamically isolated ellipsoidal particle. The orientation equations, however, need to be accurately solved without additional approximations. Altan & Rao show that both quadratic and hybrid closure approximations yield significant errors in complex suspension flows. Their use in conjunction with differential evolution equations in geometrically complex moldings yield errors large enough to distort or falsify the

resulting orientation predictions. A number of researchers have modelled the development of fiber orientation in planar contraction flow by using experimental and numerical techniques.

Harris & Pittman (1976) have done the most relevant experimental investigation of fiber orientation in this geometry. They studied a dilute suspension of fibers in laminar flow through a planar converging channel, with Re = 1000. Due to low microscopic Reynolds number, the effect of fiber inertia was negligible. The fiber orientation anisotropy was found to vary with C and to be independent of Re, μ, a_p and contraction half angle, β. Fiber orientation followed the theory of inertialess fibers in homogenous Stokes flow. However, in most fiber suspension flows of interest, the influence of fiber inertia and turbulence on orientation cannot be neglected. Ullmar & Norman (1997) and Ullmar (1998) measured the orientation anisotropy of nylon fibers in the $x_1 - x_3$ plane (see figure 4) in a straight channel downstream of the contraction outlet. The flow inlet to the contraction consists of a series of turbulence generating step expansion tubes positioned immediately upstream of the inlet. In these studies, the influence of flow Reynolds number, contraction ratio and fiber concentration on the orientation anisotropy was investigated. They concluded that the orientation anisotropy is strongly dependent on the contraction ratio and almost independent of the fluid Reynolds number. However, the turbulent fluctuations in these studies were not measured; therefore, they could not relate the orientation anisotropy to the turbulent flow characteristics. It should be noted that in their studies the measured orientation distribution is an average over the entire height of a straight channel

attached to the downstream of the contraction outlet. It is known that the turbulent properties change in the straight channel downstream of a contraction and thus the measured orientation distribution would be different from that at the outlet of the contraction (see Harris & Pittman, 1976).

Kacir et. al. (1975) studied the fiber orientation of suspension flow at the outlet of a converging channel. They suggested that the experimental accumulative curves can be described by an exponential equation $\psi(\phi) = 1 - \exp^{(c_1\phi)}$ where c_1 is an empirical constant. Fiber dispersion increased and fiber orientation became more isotropic with increasing turbulent intensity due to the increase in streamwise component of fluctuation velocity in fiber suspension flow. This was found to also change the rheology of the fiber suspension flow.

Bernstein & Shapiro (1994) measured the orientation of a glass fiber suspension in laminar and turbulent pipe flow. They found that at low Reynolds number laminar flow, the fibers are randomly distributed near the pipe center. The fibers become more oriented in the streamwise direction with increasing Reynolds number in the laminar regime. At high Reynolds number turbulent flow, the randomizing effect of the turbulence lead to an almost random orientation.

2.3 Flow induced fiber orientation with inertia

In the specific case where inertia can be neglected, the dynamics of single particle motion, interaction with other particles, and effects on the bulk properties are well understood. However, most particle transport applications of practical interest

involve suspension flow with inertia. In addition to turbulence and strain, finite fiber inertia affects the motion of rigid fibers in suspension. Particle inertia is important when particle Reynolds number is greater than one and the Stokes flow simplifications cannot be used. Consider a gas- particle suspension where the particle Reynolds number is high and the fluid Reynolds number is relatively small. In this case, the particle inertia is important and the fluid inertia is negligible. Thus, the fluid equation can be simplified to the linear Stokes equation while the complete Navier-Stokes equations should be solved for the flow adjacent to the particles surface (Koch & Hill, 2001). However, in many industrial applications the macroscopic Reynolds number based on the local mean streamwise velocity in the contraction, U_1, and the contraction local height, h, is defined as

$$\mathrm{Re} = \frac{U_1 h}{\nu},$$ (3)

where ν is the fluid kinematic viscosity (water in this study), and the microscopic Reynolds number based on the streamwise mean local rate of strain, $\partial U_1/\partial x_1$, and fiber half length, L, defined as

$$\mathrm{Re_f} = \frac{(\partial U_1/\partial x_1)L^2}{\nu},$$ (4)

are of $O(10^5)$ and $O(10^2)$, respectively. Thus, the inertia of both the continuous and discrete phases cannot be neglected. The governing equations become more complex when the Reynolds number of both particle and the fluid are $O(1)$ or greater. This presents a challenge, as the full equations governing the motion of a particle suspended

20

in a fluid are non-linear when considering inertia. Exact analytical results are available for only a few simple flows. In order to study the fundamental effect of inertia on particle motion, particle interaction and suspension microstructure, the full non-linear momentum equation must be solved to analyze the dynamics of individual particles in suspension. At present, researchers are using numerical simulation techniques to predict the behavior of two-phase particulate suspensions with inertia. Direct numerical simulation has been proven to be capable to simulate the behavior of inertial suspensions (Bunner & Tryggvason, 1999).

In many investigations (e.g. Cox, 1970, Harris & Pittman, 1976, Olson & Kerekes, 1998 and Olson, 2001) the microscopic Reynolds number is based on fiber half length as given in equation 4. However, Bernstein & Shapiro (1994) used the fiber diameter as the length scale and concluded that since the microscopic Reynolds number based on this length scale is small, the effect of fiber inertia in their experiments is negligible. Since these investigations do not include the motion of fibers with large fluid Reynolds number, it is not clear which length scale can effectively describe the effect of fiber inertia. The appropriate choice of length scale is important in determining the validity of the orientation model used in this work.

Feng & Leal (1997) reported the result of a two-dimensional finite element direct simulation of the motion of a neutral and non-neutrally buoyant isolated circular particle suspended in a Newtonian incompressible fluid in Couette and Poiseuille flow. Fluid flow is computed from the nonlinear Navier-Stokes equations, and the motion of the particle is determined by Newton's equations for rigid bodies under

21

the action of hydrodynamic force and torque arising from the fluid flow. Particle Reynolds numbers were large enough to include nonlinear inertial effects and wall effects. The driving forces of particle migration were identified.

A relatively new simulation method has been proposed for analysis of suspensions with inertia. This method involves a numerical simulation of particulate suspensions by coupling the solution of the discrete Boltzmann equation for the fluid phase to the translation and rotation of solid particles suspended in fluid. The most important feature of this technique is that the algorithm is efficient, and computation cost scales linearly with the number of particles considered. An early application of the discrete Boltzmann method to analyze the motion of particles suspended in fluid was presented by Ladd (1988, 1994). His results agreed quite well with both known analytical results for Stokes flow and finite element results for finite Reynolds number flows. The streamlines for steady incompressible flow past a column of circular cylinders at Reynolds numbers varying from 10-100 were computed. The recirculation region behind the cylinder grew with increasing Reynolds number, as expected. The momentum being removed from the system due to the force applied to the stationary particles is directly proportional to particle Reynolds number. Ladd was able to simulate suspensions of up to a particle Reynolds number of 200, and particle number of 1024 spheres. This method allows for simulation of suspensions of various particle size, particle shape, electrostatic interactions, flow geometry, Péclet number, and Reynolds number. However, it is limited to particles of density greater than the fluid.

Aidun, Lu, & Ding (1995, 1998) improved upon Ladd's simulation by accounting

for the excluded volume in the fluid phase due to the presence of particles. This results in improved accuracy and robustness of the simulation, allowing for analysis of suspensions of arbitrary particle-liquid density ratio. Aidun used direct numerical analysis of the discrete Boltzmann equation for the analysis of impermeable ellipsoid particles suspended in an incompressible Newtonian fluid with inertia.

Two interesting observations were obtained from simulation of a 2-D ellipsoid in simple shear flow at particle Reynolds numbers ranging from 0 to 40. First, a critical Reynolds number existed where the particle ceased to rotate. Physically, this shows that at a given orientation angle relative to the flow, the positive torque on the top and bottom surfaces of the ellipsoid is exactly counterbalanced by the negative torque at the recirculation zones. Thus, at the critical particle Reynolds number the particle will cease to rotate, and orient at a fixed angle to the flow. Second, the period of rotation scales universally to the half power of the particle Reynolds number. Here, particle Reynolds number is based on the length of the major axis of the ellipsoid.

Additional application of the finite element method to simulate complex particle motions of sedimenting spheres and ellipses is found in work done by Huang, Hu, & Joseph (1998). Their simulation provides basic information on particle motion and interaction at non-zero particle Reynolds number. This method is based on coupling the solution of the Navier-Stokes equation for the fluid domain to the motion of a suspended particle. They conducted numerical simulations of the settling of ellipsoids suspended in Newtonian and elastic fluids in a narrow two dimensional channel at finite Reynolds number. It was found that inertia tends to turn the long side of the

ellipse across the stream. At a Reynolds number 0.31 the ellipsoid turns vertical and drifts towards the channel center with a damped oscillation. At a Reynolds number of 0.82 the ellipse turns horizontal as it migrates to the channel center. At high Reynolds numbers, stagnation forces dominate and cause the particle to orient in the cross-stream direction. At lower Reynolds number, both lubrication and stagnation forces determine the rotation and translation of the ellipsoid. This reveals that a small change in the particle Reynolds number can significantly change the dynamics of particle motion in suspension.

Zettner & Yoda (2000) studied the effects of fluid inertia, geometry and flow confinement upon the dynamics of neutrally buoyant elliptical and non-elliptical cylinders over a wide range of aspect ratios in simple shear flow using particle image velocimetry (PIV). They found that elliptical cylinders of moderate aspect ratio cease to rotate, coming to rest at a nearly horizontal equilibrium orientation, above a critical Reynolds number. Their experimental results were in good agreement with the lattice-Boltzman results by Ding and Aidun (2000).

2.4 Turbulence development in a contraction

Considering the flow is turbulent, in order to study the dynamics of fiber motion inside this contraction, it is necessary to first understand development of single phase turbulent flow in this geometry. In most cases, turbulence consists of random motion having coherent structures of varying scale. Analytical theories governing the dynamics of turbulence are available only for simplified cases where the governing

equations are linear.

Among the fundamental unsolved problems of fluid mechanics is how contracting a vortex filament effects turbulence. Isotropic turbulence can be thought of as a collection of randomly oriented three-dimensional cylindrical vortex filaments. Streamwise velocity fluctuations are caused by vortices aligned perpendicular to the flow axis and lateral velocity fluctuations are caused by vortices aligned along the axis of flow. Anisotropic turbulence is produced by stretching randomly oriented vortices at the contraction inlet and aligning them in the streamwise direction. This results in suppression of streamwise turbulent component and enhancement of the lateral turbulent components.

Applying Kelvin's circulation theorem to predict the intensity of turbulent vortices in an axisymmetric contraction, it can be shown that the streamwise component of turbulence decays through the contraction, whereas the transverse component grows (Prandtl, 1933). However, the streamwise and transverse components of turbulent intensity decrease monotonically with increasing contraction ratio. The contraction ratio, C, is defined as the ratio of local mean streamwise velocity to the inlet mean streamwise velocity. The limitation of this Lagrangian approach is that the model does not account for interaction of vortices.

A distribution of vortex cells more representative of turbulent flow may be considered using Cauchy's equations (Taylor, 1935). Taylor's model predicts a slower rate of decay for the fluctuating component of turbulence in the streamwise direction, and a slower rate of growth for the transverse fluctuating component. Taylor's result may

25

be extended by integrating over all wave numbers to predict the effect of contraction on turbulence (Batchelor & Proudman, 1954, Ribner & Tucker, 1952). In this model, inlet turbulence is assumed isotropic, for which the turbulent spectra may be represented by a simple analytical expression. Viscous dissipation of turbulent energy is neglected. This assumption should not lead to significant error since it is known that the majority of turbulent energy is contained in large scale eddies. Also, the time scale of the flow is assumed to be much smaller than the time scale of eddy interaction. This important assumption makes the problem linear. Consequently, this approach is referred to as 'linear theory' or 'rapid distortion theory'. The model predicts streamwise and transverse turbulent energy components as a function of local contraction ratio only. Based on comparison with experimental data, the model developed by Batchelor & Proudman and Ribner & Tucker more accurately predicts the development of turbulent energy components in a contraction. The major limitation of linear theory is that no contraction of practical interest completely satisfies the requirement of rapid distortion.

Several investigators have studied different aspects of flow through axisymmetric contractions (Uberoi, 1956, Hussain & Ramjee, 1976). Experimental studies of the development of components of fluctuation velocity in an axisymmetric contraction show that linear theory is valid for predicting streamwise velocity fluctuations for contraction ratios, $C < 4$. According to Uberoi, initially isotropic turbulence becomes increasingly anisotropic and the measured streamwise component of fluctuation velocity becomes significantly higher than predicted at $C > 4$. This behavior directly

26

contradicts linear theory. As the contraction ratio increases, bulk flow inhomogeneity also increases, leading to the deviation seen between linear theory and experimental results. Measured transverse turbulent energy components slightly deviate from linear theory. This is attributed to the transfer of energy between streamwise and transverse velocity fluctuations. Goldstein & Durbin (1980) showed that the amplification of the streamwise turbulent energy component in the range $C > 4$, depends strongly on the spatial scale of turbulence. Another interesting finding is that the interaction between the turbulence and the mean flow also depends on the spatial scale of turbulence. Streamwise and lateral components of turbulent intensity remain nearly constant for $C > 40$ (Hussain & Ramjee, 1976). However, contradictions exist in the streamwise and lateral fluctuating velocity components reported by Uberoi (1956), Hussain & Ramjee (1976), and Tulapurkara & Ramjee (1980). Durbunovich (1987) showed that the principal reason for the disagreement was the presence of unsteady flow caused by boundary layer seperation and periodic shedding of vortices at the outlet of the contraction. Measurements with unsteady flow yielded similar results as previous investigators. However, when the unsteady flow was removed from the system the streamwise velocity fluctuations followed a power law form similar to linear theory given by $\overline{u_1'^2}/\overline{u_{1,0}'^2} \propto C^{4/3}$. This shows a weaker influence of C on development of streamwise velocity fluctuations than follows from linear theory. It is clear that linear theory is inadequate to predict the effect of contractions on turbulent characteristics. Experimental results show that small eddies are exposed to the stretching and shearing motions of large eddies in turbulent flow. Therefore, a

non-linear theory taking into account the precontraction turbulence is needed.

Hussein & Ramjee (1976) investigated the effect of contraction shape on turbulence. They measured the velocity fluctuation in four different axisymmetric contractions with identical total acceleration. They concluded that the total strain, $(\partial U_i/\partial x_j)$ is the primary parameter influencing the development of turbulent energy components. Townsend (1954), and Tucker & Reynolds (1968) investigated the effect of contraction on the core turbulent flow with constant mean rate of strain. Townsend found that after certain degree of strain, an equilibrium structure of turbulence is established. The mechanisms that transfer energy between the different components are then so effective that further strain produces only a small alteration in the structure. However, Tucker & Reynolds argue that the flow never reaches an equilibrium structure.

Hunt & Carruthers (1990) showed that the interaction between the turbulence and the mean flow, which is responsible for the amplification, increases with decreasing wave number. The mean square streamwise velocity component along with its spectra are inversely proportional to C, while the mean-square transverse velocities and spectra are inversely proportional to C. Thus, the turbulent velocity ratio is independent of contraction ratio. They showed that the amplification effect of the contraction is reduced when the turbulent scale increases. It was observed that the acceleration, through the contraction, suppresses the relative turbulent intensity, which therefore has almost no effect on the mean velocity distribution in the contraction. Convective acceleration causes the turbulence intensity to decay monotonically with increasing

C. The lateral normal components of the Reynolds stress tensor were shown to have nearly the same magnitude in the region $C > 4$. This is most likely due to the streamwise alignment of initially random oriented turbulent vortices. The decay rate of turbulent energy decreases with increasing turbulence scale. Conversely, decreasing the contraction half angle was shown to increase the decay rate of turbulent kinetic energy. This is most likely due to the differences in residence time between the two contractions, as viscous dissipation of turbulent energy increases with residence time.

Tsuge (1984) found that small eddies decay through the contraction in agreement with Batchelor & Proudman. However, large eddies are amplified due to the stretching of vortices. Comparison of predicted streamwise velocity fluctuations to experimental results showed good agreement, with the exception of low Reynolds number flow and long pre-contraction distances leading to exaggerated dissipation of small eddies in the initial constant flow section due to the assumption of no energy cascading made in formulating the model.

A limited amount of work has been done on the development of turbulence in a planar contraction. Parsheh (2001) found that the intensity of the normal Reynolds stress components decreases in this geometry. He also showed that the normal Reynolds stress components have a minimum at $C = 2$.

Recently, several researchers have used turbulence models found in commercial codes to model turbulence in a planar contraction (Parsheh, 2001). Computations showed that the differential Reynolds stress model and the algebraic Reynolds stress model qualitatively predict the behavior of turbulent flow in this geometry. Inlet

dissipation scale was the primary turbulent parameter influencing the development of turbulent quantities. When compared to measurements, the $K - \epsilon$ model was found to be inadequate in quantitatively predicting turbulent flow behavior in this geometry. The model overpredicts the decay of mean square component of fluctuating velocity and sometimes resulted in unrealistic values.

Existing analytical models used to predict turbulence in contractions are shown to be inaccurate for large C. Several numerical simulations of turbulent plane strain flow have been performed to investigate the structure of homogeneous turbulence subject to irrotational strain. It is well known that the range of turbulent scales increases rapidly with flow Reynolds number. Therefore, due to limitations of computer capacity, these simulations are restricted to low Reynolds number flow and simple geometries. Recently, several numerical simulations of turbulent plane strain flow have been performed to investigate the structure of homogeneous turbulence subject to irrotational strain (Lee & Reynolds 1985, Kwak et al. 1975, and Rogallo & Moin 1984). Lee & Reynolds (1985) were the first to provide complete Reynolds stress budgets for axisymmetric and plane strain contraction flow. They observed that the Reynolds stress anisotropy that develops under slow deformation is larger than that predicted by RDT. The stress anisotropy continued to increase when the straining was removed. This result contradicts the idea that isotropy will be restored when straining is removed. Therefore, the traditional theory of return to isotropy is not necessarily valid. At present, the computational power is not available to run accurate numerical simulations of the motion of suspended fibers at Reynolds numbers

$O(10^5)$.

Currently, no proven model is available to accurately predict turbulent parameters in a contraction in the region $C > 4$. Therefore, in order to relate turbulence in the contraction to fiber orientation it is necessary to directly measure the turbulence in the contraction.

2.5 Rotational diffusion of fibers in turbulent contraction flow

A limited number of studies have been done concerning the motion of rigid fibers in turbulent flows. In these flows the dispersion of individual fibers is altered due to the presence of velocity fluctuations.

Analogous to suspension flows with Brownian motion and fiber-fiber interaction, the effect of turbulence on orientation anisotropy have been modelled by a rotational diffusion coefficient tensor (e.g. Krushkal & Gallily, 1988 and Olson & Kerekes, 1998 and Olson et. al., 2004). Olson & Kerekes expressed the turbulence induced rotational diffusion coefficient in an isotropic turbulent flow as a function of turbulent integral time and length scales, turbulent intensity and fiber length. They found that by increasing the ratio of the fiber length to the Lagrangian integral length scale, the diffusion coefficient decreases. Recently, Olson et. al. (2004) numerically solved the Fokker-Planck equation governing the orientation distribution of fibers at the centerline of a planar contraction. They state that the rotational diffusion coefficient, D_r, is constant throughout the contraction and, that $D_r = 2\sec^{-1}$ gives the best agreement with experimental studies of Ullmar (1998). A quantitative comparison

requires orientation measurements at the contraction centerline (as done in this study) where the equations are derived for. The measurement of fiber orientation distribution at a straight channel downstream of the contraction outlet represents an average of all fibers and therefore, inconsistent with the governing equations for the centerline.

The rotational and translational diffusion of particles is controlled by the local velocity fluctuations due to turbulence and by the ordered motion of large-scale turbulent structures. Olson & Kerekes (1998) expressed the rotational diffusion coefficient as a function of turbulence integral time and length scales and fiber length. They found that the diffusion coefficient decreases as fiber length decreases. Recently, Olson et al. (2004) numerically solved the Fokker-Planck equation governing the orientation distribution of fibers in a planar converging channel. They assume that the rotational diffusion coefficient, D_r, is constant throughout the contraction. They concluded that $D_r = 2 \sec^{-1}$ gives the best agreement with experimental results. The rotational Péclet number, which is function of the contraction ratio, inlet velocity, contraction length and rotational diffusion coefficient, governs fiber orientation development in this geometry.

A kinetic theory predicting the dispersion of fibers oriented along the extensional axis of axisymmetric and planar contractions was developed by Shaqfeh & Koch (1990). This model shows that the mean square displacement for a dilute fiber suspension is $O(nL^3/\ln^2 a_p)$. They found that the rate of dispersion increases to a maximum with increasing concentration in the dilute regime. The dispersion rate then decreases as concentration approaches the semi-dilute regime. It was also observed

that fiber dispersion inside a planar contraction is anisotropic in the dilute regime. Dispersion in the transverse direction was greater than dispersion in the streamwise direction.

Few researchers have studied the motion of rod-like rigid particles (fibers) in turbulent flows. Cho et. al. (1980) studied the orientation of high aspect ratio ice crystals in atmospheric turbulence. They compared the estimated average time required for the fibers to become oriented and the time of the eddy interactions and observed that the effect of the atmospheric turbulence on the fiber orientation is negligible.

Krushkal & Gallily used the Fokker-Planck equation to determine the orientation distribution of small fibers in turbulent shear flow. They concluded that particles become randomly oriented in the presence of strong turbulence. However, for flow with mean velocity gradients, the orientation distribution function is anisotropic if the turbulent intensity is not large enough to randomize the particles.

Olson & Kerekes (1998) developed expressions for the translational and rotational dispersion coefficients, which can be used in the convection-dispersion equation of the orientation distribution. They coupled the translational and rotational dispersion coefficients to the properties of the turbulence. Expressions were given for the dispersion coefficients as a function of fiber length, streamwise fluctuation velocity component, integral length scale, and integral time scale. In their study it was assumed that integral length and time scales were isotropic and thus could be shown by single scalars. This assumption leads to a significant error for flow in contractions in which the flow undergoes a large extension in one direction and compression in another direction.

They concluded that the dispersion coefficients are dramatically damped by increase of the fiber length or decrease of the turbulent length scale. They showed that the dependence of rotational dispersion to the fiber length is more significant. In plane contractions, with decreasing the integral scale, this can imply that the effect of the flow fluctuations on the fiber dispersion is negligible at high contraction ratios. Few experimental studies of fiber orientation of suspensions can be found in the literature. Koch & Rahnama (1995) visualized the orientation of an opaque tracer fiber in an index of refraction and density matched fiber suspension in planar extensional flow.

2.6 Particle-turbulence interaction

It is important to consider the effect of fibers on the turbulence of the fluid in developing models for two-phase flows. Most models relating turbulent parameters to fiber diffusion assume that the presence of fibers has a negligible effect on the dynamics of the turbulent fluid flow. This one-way coupling is usually valid for small fiber volume fractions ($\phi_c << 1$) or high Stokes numbers (Gore & Crowe, 1991). The two-way coupling of turbulence and fiber motion also considers the effect of fibers on turbulent velocity fluctuations of the fluid. The presence of fibers results in either turbulent energy production or an increase in the dissipation rate depending on ϕ_c. The change in fluid Reynolds stresses influences particle diffusion and the hydrodynamic drag between the fiber and fluid. Squires & Eaton (1990) used direct numerical simulation of a gas-particle suspension in low Re homogeneous, isotropic turbulence to consider the effect of two-way coupling. They determined that the fluid turbulent energy and

dissipation rate increased by as much as a factor of three due to the presence of particles. Particles also caused the energy in the highest wave numbers to increase relative to the lower wave numbers.

Recently, the two-way coupling of turbulent flow dynamics and fiber motion has drawn increasing interest in the field of two-phase flow research. It has been observed that particles on the order of the smallest scales of turbulence tend to dissipate turbulent energy, while larger particles have a tendency to produce turbulent energy (Gore & Crowe, 1989). The presence of boundary layers on the fiber surface has been shown to alter the Reynolds stresses of the fluid for fibers larger than the smallest scales of turbulence (Elghobashi, 1992). Turbulence production is likely due to wake formation behind a moving particle (Hetsroni, 1989). The transition between energy dissipation and production occurs when the particle size is of the order of the turbulent integral length scale. Two-way coupling has been shown to be negligible for particle volume fractions smaller than $O(10^{-6})$. For larger particle volume fractions, $O(10^{-6}$ - $10^{-4})$, the change in turbulent energy is determined by the ratio of particle response time to the turnover time of a large eddy (Elghobashi, 1993). Also, there is an increased tendency for particles to move towards regions of high strain rate and low vorticity with increasing ϕ_c. Yuan & Michaelides (1992) assumed that the damping motion of an individual particle was responsible for turbulence dissipation and that the wake behind the particle was responsible for turbulence generation. Based on these assumptions they have developed a model which predicts the change of fluid turbulent kinetic energy as a function of particle diameter, fluid density, wake length,

and local normal Reynolds stresses. Yarin & Hetsroni (1994) improve upon the model of Yuan & Michaelides by providing a more detailed account of the influence of the particle wake. These models are shown to be accurate for flows with no turbulent production due to mean velocity gradients. Crowe (1993) gives a good overview of the existing models for particle induced turbulence generation and dissipation in two-phase flows.

2.7 Application to paper forming

In the paper industry, mechanical properties of manufactured paper are known to be anisotropic due to the fiber orientation induced by the flow kinematics while passing through a planar contraction with flat walls. Therefore, enhancement of material properties and reduced manufacturing costs can be achieved if the final fiber orientation can be predicted accurately. Predicting the orientation behavior of fibers suspended in water during the paper forming process is of specific interest in this research. Control of fiber orientation is of great importance in paper forming.

Normally, it is advantageous to manufacture paper with isotropic mechanical properties. Substantial strength gains can be obtained in the forming process by manipulating the fiber suspension microstructure through hydrodynamic means. Increasing the fiber orientation isotropy of a finished sheet of paper generally results in increased strength uniformity and reduced fiber consumption. Printing grades characterized by a high degree of isotropy demonstrate a high degree of dimensional stability. This reduces end use problems such as such as twist warp and sheet curl. On the other
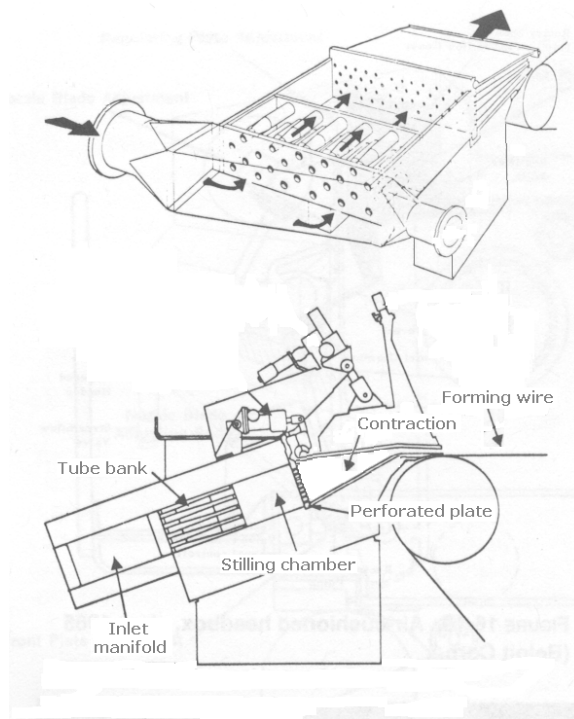
Figure 1: Schematic of a Beloit Converflo hydraulic headbox (Smook, 1992)

hand, in certain paper grades it is desirable to achieve a highly anisotropic orientation state. Newsprint is an example of a paper grade which primarily requires strength in one direction. Therefore, fiber consumption may be reduced by producing a highly oriented sheet of paper.

A hydraulic headbox, the primary component of the forming zone of a modern paper machine, is illustrated in figure 1. The primary function of the headbox is to transfer suspension flow in a pipe into a wide rectangular free jet with uniform velocity in the streamwise direction. For instance, a flow from a pipe with diameter 0.800 m will be diverted to a .01 m thick and 10 m wide liquid jet with uniform velocity. A typical fiber suspension volume fraction found in paper manufacture is

0.1 to 1%. Fiber suspension flow typically enters the forming zone by a tapered manifold which distributes the flow evenly over the width of the paper machine. A series of step diffuser tubes produces turbulent flow which serves to break up small flocs and mix the suspension before entering the contraction. The suspension is then contracted in one direction and exits the contraction in a rectangular free jet. The jet from the nozzle impinges onto a finely woven plastic belt called a wire moving at speeds up to 2000 m/min. The wire serves to increase the suspension concentration through drainage.

CHAPTER 3

EXPERIMENTAL METHODS

It is well known that flow induced alignment of dilute fiber suspensions in con-
tractions is influenced by mean velocity gradients, turbulence, and finite fiber inertia.
The main purpose of this thesis it to understand the physics governing aspects of
turbulent flow and fiber orientation inside a planar two-dimensional contraction with
application to paper manufacturing. It is necessary to quantify the turbulent flow
characteristics and fiber orientation state inside the contraction in order to under-
stand the coupling of fiber dynamics and turbulence. The effect of particle-particle
interaction is not considered, and it is assumed that the dilute suspension does not
significantly alter the bulk single phase flow.

3.1   Flow Facility

In the present study, high speed imaging and laser Doppler velocimetry techniques
are used to investigate the influence of turbulence on the orientation state of a fiber
suspension in high Reynolds number flow. Velocity field measurements of single phase
flow and visualization of dilute fiber suspension flow were carried out in a closed water
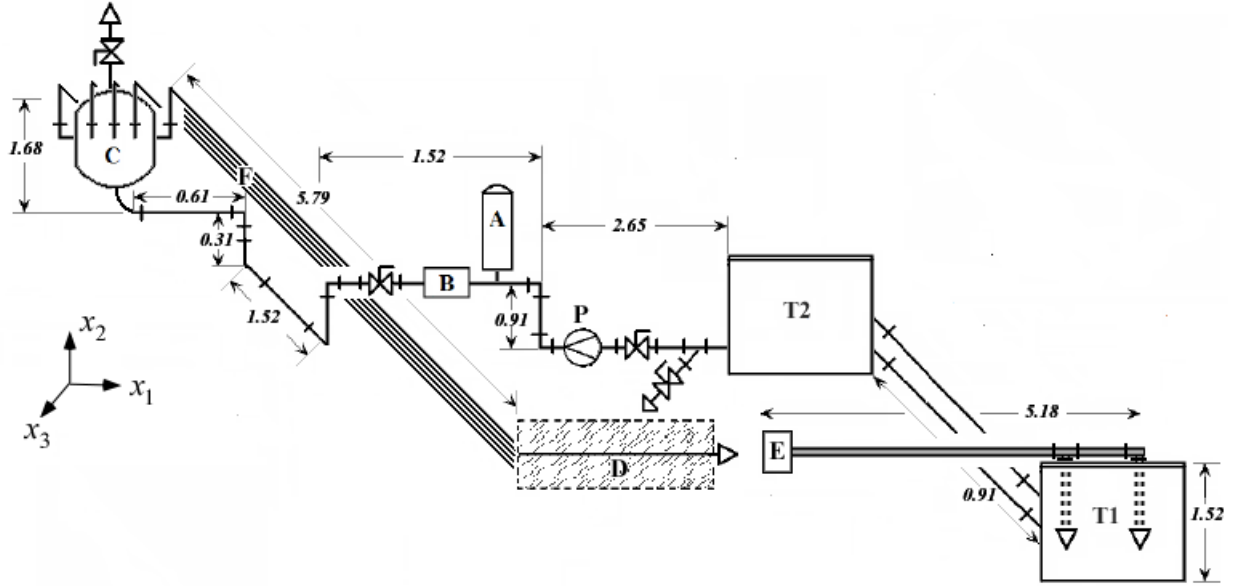
Figure 2: Schematic of flow loop (Dimensions in meters, not to scale)

loop at the Georgia Institute of Technology. The general experimental set-up is shown in figure 2 with flow components listed in table 1.

The flow was generated in a 56 cm long rectangular cross section recirculating closed channel. The fluid exits the contraction in a free jet which is diverted to two 300 gallon collection tanks in series. Fluid is recirculated by a 40 HP variable speed Ahlstrom centrifugal pump, with a capacity of 500 gal/min at 257 kPa.

The volumetric flow rate is measured using a magnetic flow meter (B) with ± 0.5% accuracy. From the flow meter, the fluid then travels to a pressure equalization vessel (C) where it is distributed equally to 20 individual 1" PVC Pipes (F) and is carried to the entrance of the rectangular channel. A constant cross-section channel with a flow straightener and a turbulence damping screen conditions the flow prior to entering the contraction. Flow first passes through a hexagonal flow straightener.

Table 1: Description of flow components

Label	Description	Manufacturer & (Model #)	Properties
A	Surge tank	Capacity: 18.1 L	
B	Flow Meter	Krohne IFC 110 (IFS-4000)	Range: 0 - 350 GPM
C	Pressure equalization vessel	──	Capacity: 227 L
D	Test section	──	See figures 5 & 4%
E	Flow deflector	──	10" O.D. Schedule 80 PVC pipe
F	Tube bundle	──	20 1" PVC tubes
P	Pump	Sulzer (Apt 21-2B)	Capacity: 500 GPM
	Pump motor	Reliance electric (P3260397H)	40 HP, 60 Hz, 3560 RPM
	Controller	Danfoss	
T1 & T2	Collection tanks	───	304 SS, Capacity: 300 GPM
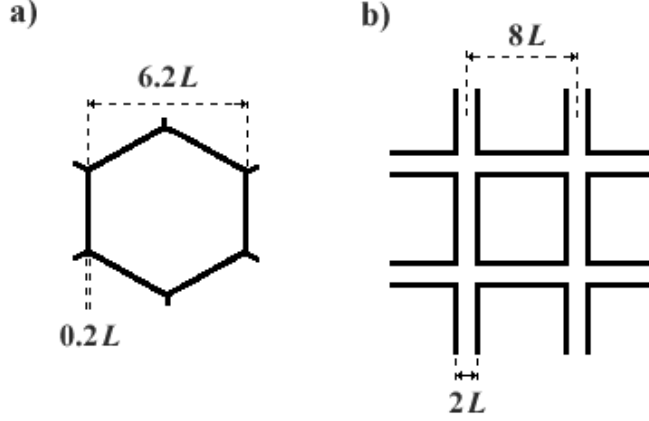
Figure 3: Grid & Honeycomb dimensions.

The flow straightener has an open width of $6.2L$, a closed width of $0.2L$, and is $44L$ in length. The fiber half length, L, is used as the characteristic length scale. Once the flow is straightened, nearly isotropic, homogenous turbulence is generated by a square monoplanar grid. The grid is located a distance $80L$ upstream of the contraction inlet in order to achieve nearly isotropic turbulence entering the contraction. The center distance of the grid, M, is $8L$ with a bar width of $2L$, resulting in a solidity of 0.56 (the solidity is defined as the grid geometric blockage area divided by the total area). The dimensions of these flow conditioning devices are illustrated in figure 3 and outlined in table 2.

The contraction is $344L$ in length, $96L$ wide, inlet height is $112L$, and the outlet height is $10L$ giving the contraction half angle, $\beta = 8.4^o$, and maximum contraction ratio of 11.7. The constant cross sectional channel and contraction are constructed of Plexiglass to allow for visual access to the flow. The streamwise and lateral directions are denoted x_1, x_2, and x_3, respectively. The origin of the coordinate system is located at the inlet centerline of the converging channel, see figure 4.

42

Grid	
Geometry	planar,square
Side	9.525 mm
Center distance	12.7 mm
Open area	56 %
Honeycomb	
Geometry	Hexagon
Open width	10 mm
Closed width	0.4 mm
Length	70 mm

Table 2: Grid & Honeycomb Dimensions
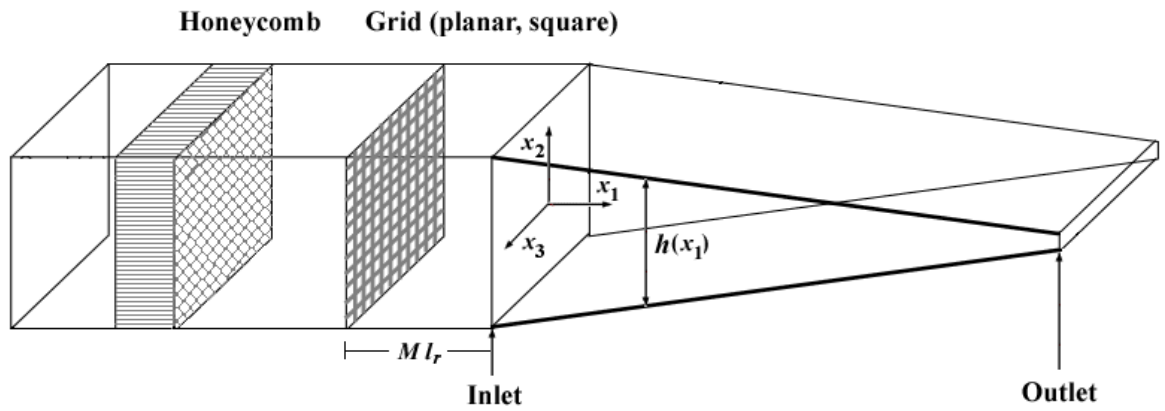
Figure 4: Schematic of grid generated turbulence experimental set-up with coordinate system.
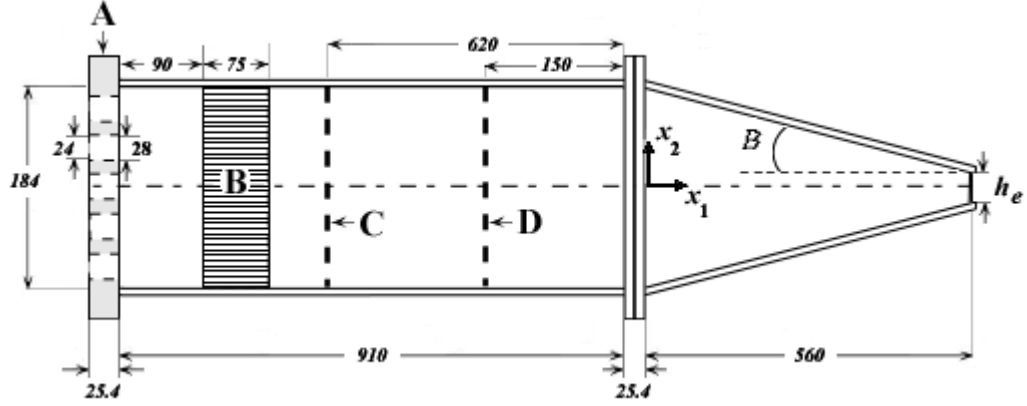
Figure 5: Cutaway schematic of the planar contraction and constant cross section channel (not to scale, dimensions in mm). Flow is in the positive x_1- direction. A) Tube block, B) Honeycomb, C) Grid position $l_r = 60$ and D) Grid position $l_r = 20$

We consider turbulent flow under plain strain, where the flow is contracted only in the x_2 direction. The mean velocity gradient tensor for the core flow through the planar contraction (see figure 4) is given by

$$\frac{\partial U_i}{\partial x_j} = \begin{pmatrix} \frac{\partial U_1}{\partial x_1} & \frac{\partial U_1}{\partial x_2} \approx 0 & \frac{\partial U_1}{\partial x_3} \approx 0 \\ \frac{\partial U_2}{\partial x_1} & -\frac{\partial U_1}{\partial x_1} & 0 \\ 0 & 0 & 0 \end{pmatrix}. \tag{5}$$

If the effect of the side walls is negligible, the nozzle contraction may be considered two-dimensional to simplify the analysis. Thus, the mean velocity in x_3-direction, U_3, is zero. Far downstream of the grid, the streamwise mean velocity profiles along the x_2- and x_3-directions are uniform. In the contraction, the mean velocity profile remains uniform except at the boundary layer region. Thus, $\partial U_1 / \partial x_2$ and $\partial U_1 / \partial x_3$ are approximately zero in the core flow. It is expected that the streamwise rate of strain, $\partial U_1 / \partial x_1$, is the dominant term influencing fiber orientation in the contrac-

44

tion. The only non-zero component of mean vorticity vector, which is responsible for production of turbulence in a contraction, is given by

$$\omega_3 = \frac{\partial U_2}{\partial x_1}.$$ (6)

However, this term is zero at the contraction centerline because of symmetry.

The local contraction ratio is defined as

$$C = \frac{U_1}{U_{1,0}}$$ (7)

where U_1 and $U_{1,0}$ are the local streamwise mean velocity and the inlet streamwise mean velocity, respectively. The estimated velocity components $U_{1,p}$ and $U_{2,p}$ based on potential flow are given by

$$U_{1,p} = \frac{\nu \mathrm{Re}}{h_0 - 2x_1 \tan \beta},$$ (8)

$$U_{2,p} = -\frac{2\nu \tan \beta \mathrm{Re}}{(h_0 - 2x_1 \tan \beta)^2} x_2,$$ (9)

where h_0 is contraction inlet height and Re is the flow Reynolds number, given by equation 3, is constant throughout the contraction.

The relationship between $\partial U_{1,p}/\partial x_1$ and $\partial U_{2,p}/\partial x_1$ from equation 8, is given by

$$\frac{\partial U_{2,p}}{\partial x_1} = -\frac{4 \tan \beta}{h(x_1)} \frac{\partial U_{1,p}}{\partial x_1} x_2.$$ (10)
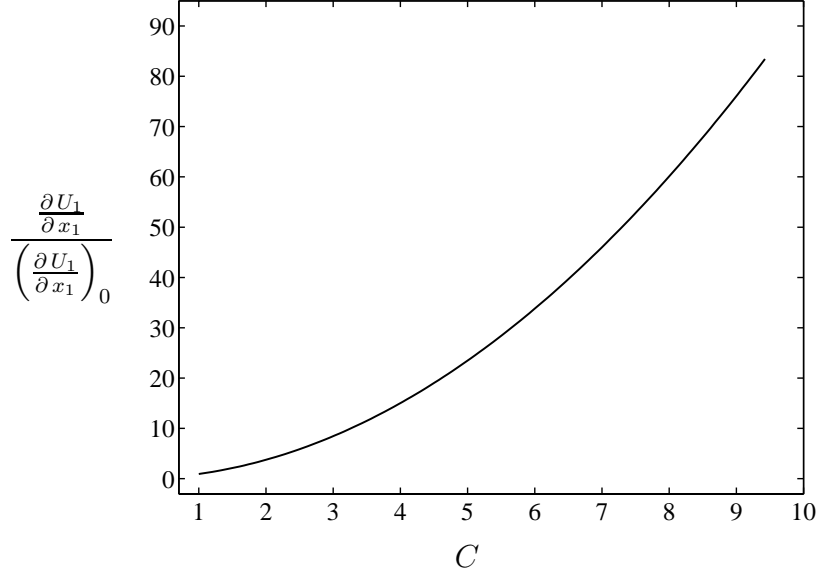
Figure 6: Normalized mean streamwise rate of strain along the centerline of the contraction.

This equation shows that when, $|x_2| \leq 0.3(h/2)$, $\partial U_{2,p}/\partial x_1$ is at least one order of magnitude smaller than $\partial U_{1,p}/\partial x_1$. The nozzle produces a variable streamwise rate of strain in the streamwise direction, which increased significantly close to the nozzle outlet. There is no rate of strain in the lateral directions.

The development of streamwise mean rate of strain for a contraction with above dimensions is shown in figure 6. The effect of convective acceleration dominates the development of mean and turbulent flow parameters inside a contraction. The contraction delivers a free jet, which is captured in a large pipe about 40 cm downstream from the outlet. To reduce the amount of air bubbles in the suspension, two 300 gallon tanks with weirs were incorporated into the flow loop.

3.2 LDV measurement technique

We are interested in the fundamental hydrodynamics of turbulent extensional flow in a planar contraction with inlet conditions similar to those found in paper forming. Laser Doppler velocimetry is a well established non-intrusive technique for fluid velocity measurement. LDV has been used to make velocity measurements in a variety of complex flow fields (Goldstein, 1996).

LDV provides information on the mean velocity and Reynolds stress components with a high degree of accuracy over a large range of velocity magnitudes. Mean flow and turbulent flow characteristics inside a planar contraction are measured in an effort to better understand the underlying hydrodynamics of this flow. Analysis of the instantaneous velocity signal yields the following turbulent parameters: x_1-, x_2-, and x_3- components of turbulent intensity, Reynolds stress components, integral time scale and turbulent kinetic energy. LDV is primarily a single point measurement technique and does not directly provide information on the spatial structure of the flow. However, some researchers have incorporated two or more systems simultaneously to directly measure the spatial scale of the flow. Direct measurement of the spatial scale is extremely challenging, requiring specialized alignment techniques. Therefore, an indirect measurement of the Eulerian integral length scale, based on Taylor's hypothesis is often considered.

A two-component fiber-optic LDV system of standard design (TSI Inc.) powered by a 5W argon-ion laser (Coherent, Innova 70) was used to measure mean velocity and Reynolds stress components in the test section. The optical head consists of a

lens with a focal length of $219L$. The beam spacing is $31L$ giving a beam half-angle of 4.09^o. The elliptical measurement volume at the beam intersection is approximately 6.25×10^{-3} in diameter and $2.5L$ in length. The system is operated in a backward scatter mode. Prior to the start of the measurements, water was filtered with a 5 μm filtering system, following which no measurements were possible due to the absence of scattering particles. The flow was then seeded with 0.3 μm TiO_2 particles. The particle time constant is $O(10^5) - O(10^6)$ smaller than the fluid time constant (based on the local height of the contraction and the free stream velocity) indicating that the particles follow the flow field.

A colorburst multiple beam separator serves to split the incident beam, shift the beam frequency, and couple the laser light to the fiber-optic cables. The x_2- and x_3- velocity components are shifted by 200 kHz to account for the one-dimensionality of the flow and to specify the directionality of the flow. The colorlink signal processor filters out low and high frequency signals to minimize noise and prevent aliasing of the instantaneous velocity data. The signal processor correlates the signals to determine instantaneous velocity components. Finally, the data is post-processed using flow information display software.

The optical head was traversed automatically using a three dimensional linear traversing system with accuracy $\pm$ 0.1 mm. Data measurement rates of instantaneous velocity were of the order 500-1500 Hz depending on position. For consistency, measurements were sampled at a constant rate of 50 Hz. for a period of 90 seconds. At each measurement location, three sets of 4,500 instantaneous velocity samples were

Table 3: LDV parameters

LDV Manufacturer	TSI
Laser power source (Coherent Innova)	5 W argon laser
Transmitting lens focal length	$219L$
Beam spacing	$31L$
Initial beam diameter	$1.3L$
Beam half angle	4.09^o
Laser Wavelength (x_1- component)	514 nm
Laser Wavelength (x_2-, x_3- components)	488 nm
Number of Fringes (x_1- component)	41
Number of Fringes (x_2-, x_3- components)	44
Probe volume	150 μm × $2.5L$
Frequency shift (x_1- component)	none
Frequency shift (x_2-, x_3- components)	200 kHz
Seeding particles (alumina)	0.3 μm

collected. A standard residence time averaging procedure was used to account for velocity biasing. In these experiments, Re was varied between 85×10^3 and 170×10^3, corresponding to exit velocities ranging from 4.9 m/s to 9.8 m/s. Table 3 summarizes the LDV parameters used in collecting instantaneous velocity measurements.

3.3 Visualization and image processing technique

Fiber orientation in the contraction was visualized using well defined rigid red rayon fibers with mean length, $2L$, and diameter, d, of 3.2 mm and 57μ m, respectively (see figure 7).

The suspension's $\phi_c\, a_p^2-$ and nL^3-values were 0.05 and 0.0053, respectively. This suggests fiber-fiber interactions and the effects of fibers on flow rheology are negligible. The fibers were dried by placing them in an oven at temperature $105\,^o$C for at least 24 hours. The density of dry rayon fibers is 1.14 kg/m^3. The suspended fibers were

Figure 7: Image of rayon fibers used in experiments

visualized in the $x_1 - x_3$ plane using a laser sheet and high speed camera, see figure 8. The light source is very important in this application since the fiber velocity is high relative to the fiber diameter. A pulsed infra-red laser, Oxford HSI1000, with a pulse duration of 15 μsec was synchronized with a Phantom V5 high speed camera. Images were collected at a rate of 25 images/sec to insure that individual fibers were not visualized multiple times. A lens was used to project a 3 mm thick, 100 mm wide rectangular laser sheet into the contraction. The laser head was translated linearly in the x_2- direction with resolution $\pm$ 0.01 mm. The camera was translated linearly in x_1-, x_2- and x_3- directions with resolution $\pm$ 1 mm. Images were taken at the centerplane of the contraction, defined as the region where $|x_2| = 0.47L$ and $|x_3| = 2.27L$. Images have dimension of 9.6 mm in the x_1-direction with 341 x 512 pixel resolution. A total of 8190 image files were analyzed at each position. The orientation distribution state at a given position was evaluated from a succession of
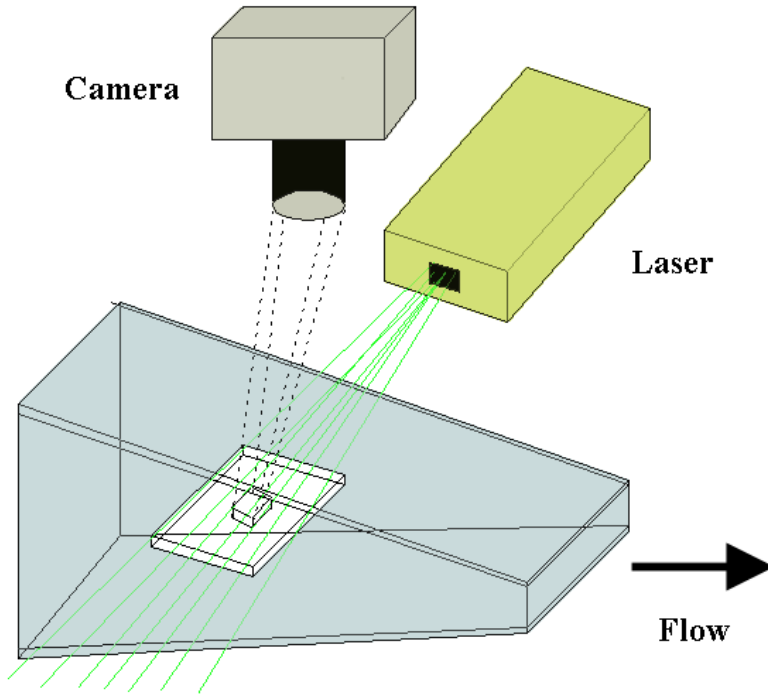
Figure 8: The experimental set-up for fiber suspension visualization.

approximately 4200 randomly imaged fibers at each position along the centerplane.

A complete software suite for analyzing these images has been developed. This software inverts the raw image, scans the frame, and identifies each fiber in the image. Although the fibers are rigid, they are not all perfectly linear. Thus, to accurately evaluate the orientation of an observed fiber, it is necessary to divide the fiber into a number of segments, 1/10th of the total fiber length, of equal length as shown in figure 9. Linear curves are fitted to each segment, and the angle distribution of the segments is evaluated and used to determine the fiber orientation distribution.

The following is a more detailed explanation of the data processing procedure mentioned above. The original images obtained from the visualization have 1024^2 pixel resolution and are $16.8L \times 16.8L$ in dimension. The original images were
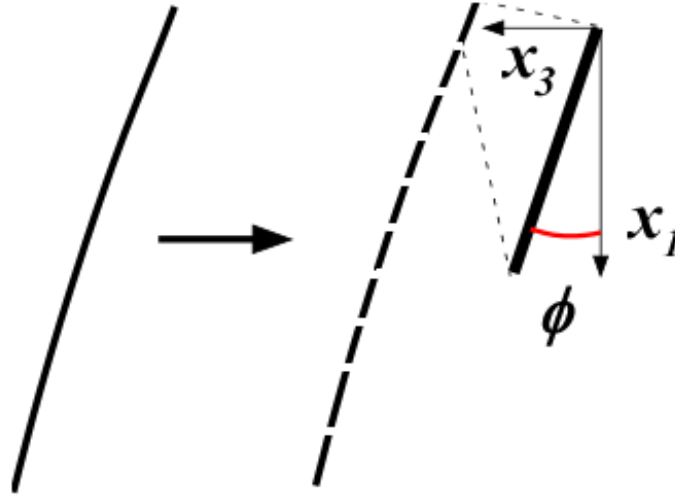
Figure 9: Schematic of the division of each fiber into segments and fitting lines by least square technique.

cropped into six equally sized images in order to achieve increased spatial resolution. The images are then inverted such that the black pixels become white and white pixels become black. Next, the background is removed from each image in a series, thus isolating the fibers on a clear background. This is accomplished by progressively loading a series of twenty-one consecutive frames and then averaging the frames to extract the background. This averaged background is then subtracted from each of the twenty-one frames, eliminating the effect of lighting gradients as well as dirt and other artifacts. The image is then binarized by assigning every pixel with a value lighter than an arbitrary threshold to be white and every one darker to be black. The resulting image is saved as a bitmap. Binarizing the image serves to simplify the subsequent orientation analysis. The next set of twenty- one images is then loaded and averaged. The process continues until every image in the series has been binarized

as shown in figure 10.

Once the images are properly conditioned, the position and orientation of each observed fiber is evaluated. This is accomplished by loading, in turn, each of the binarized frame images and scanning the image to isolate each fiber. Each binarized image of a fiber is eroded, using a skeletonizing algorithm, to single-pixel-width segments. Each skeletonized fiber in the frame is then scanned to locate and eliminate each pixel that represents the intersection of two fibers. The remaining fiber segments are traced to determine their length as well as the direction of each pixel-to-pixel intersection. Each fiber of less than $0.1L$ in length is discarded as being a non-fiber image artifact or an air bubble in the flow. Data files are then written to save the raw fiber count and position of each fiber in the frame. This process is repeated for each frame in the sequence. Figure 10 shows the raw image and the resulting processed image.

The orientation angle, ϕ, of each fiber is quantified once the images are properly conditioned and the position of each observed fiber has been evaluated. This is done by starting from the head of the fiber to divide them into segments 24 pixels (0.64 mm) in length. Once the remaining part of the fiber is smaller than 48 pixels the division of the fiber is stopped and the remaining part is considered as a segment. Then, a line is fitted to each segment by the least square method. The orientation angle of measured fibers was arranged in bins of 3 degree increment to evaluate the orientation distribution function, ψ. Finally, the obtained orientation distribution function was normalized and plotted versus the bin centers.
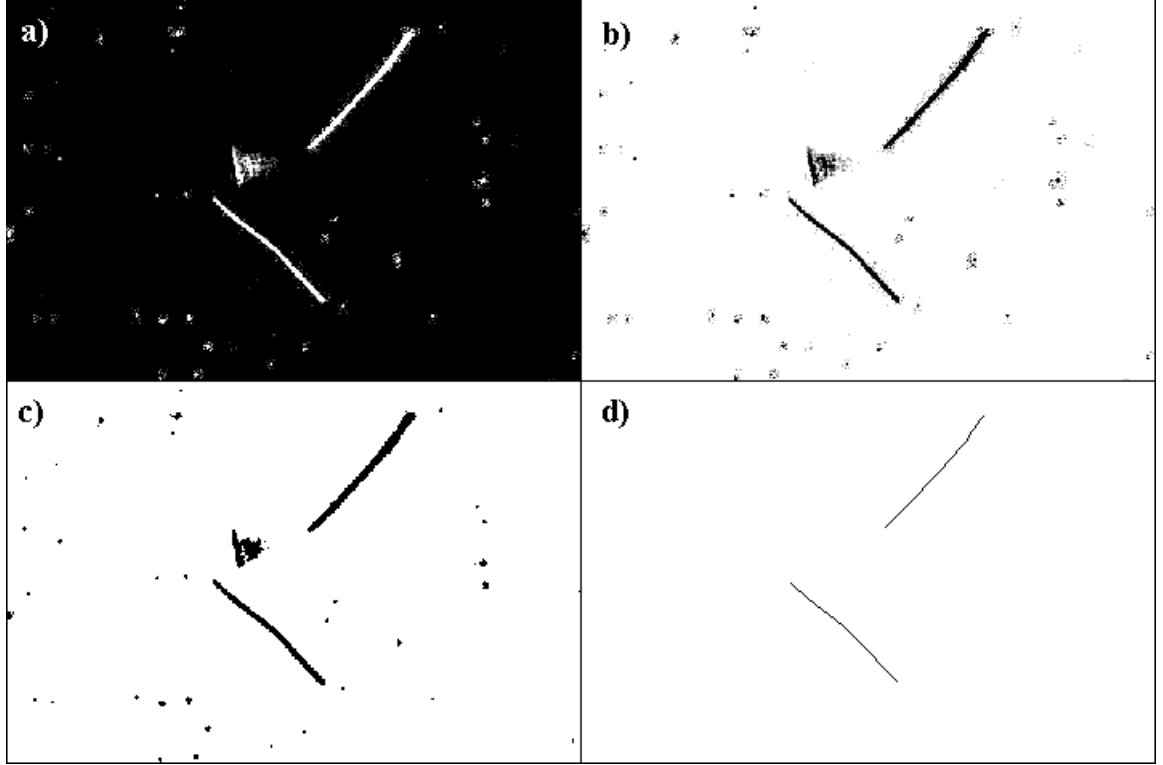
Figure 10: Overview of image analysis technique a) Sample of raw images obtained from the visualization; b) Image after inverting, c) background removal, and d) skeletonization. The flow direction is from down to up.

In these measurements, the streamwise length of images is chosen to be three times the fiber length. The contraction ratio varies slightly along this length and therefore the effective contraction ratio is defined as

$$C_e = \frac{1}{\Delta x_1} \int_{x_{1,1}}^{x_{1,2}} C(x_1)\mathrm{d}x_1, \tag{11}$$

where $\Delta x_1 = 9.6$ mm and $x_{1,1}$ and $x_{1,2}$ are the upstream and downstream edge positions of the image, respectively. The straight channel upstream of the contraction inlet and the contraction are joined by a set of opaque flanges $15.8L$ in length length. Due to the presence of these flanges and the finite length of images, the first position

downstream of the contraction inlet is $C_e = 1.1$.

3.4 LDV data correction procedure

Generally, mean and fluctuating velocity components are obtained relative to a zero position in the test section using LDV. This is due to the change in optical path of the incident laser beam due to refraction as shown in figure 11. In this case, the zero position is at the contraction sidewall. The displacement of the beam intersection in the test section is related to the displacement of the traverse in the x_3-direction by equation 12 (Durst, Melling & Whitelaw, 1981). Here, $\Delta x_3'$ denotes the displacement of the beam intersection in the test section and Δx_3 denotes the displacement of the traverse. The location of the beam intersection is a function of the optical properties of the three media the beam crosses, air, plexiglass, and water, as well as the thickness of the plexiglass. The index of refraction of air, plexiglass, and water are $m_1 = 1$, $m_2 = 1.5$, and $m_3 = 1.33$, respectively. The half angle of the beam exiting the probe head, χ_1, is 4.1^o. Subsequently, χ_2 and χ_3 are 2.73^o and 3.08^o, respectively. Therefore, the change of position of the beam intersection inside the contraction as a function of change of position of the LDV translator is given by

$$\Delta x_3' = \frac{\Delta x_3}{\cos\chi_1}\sqrt{(\frac{m_3}{m_1})^2 - \sin^2\chi_1}. \tag{12}$$

For the test section considered in this study, the above equation reduces to

$$\Delta x_3' = 1.33(\Delta x_3). \tag{13}$$
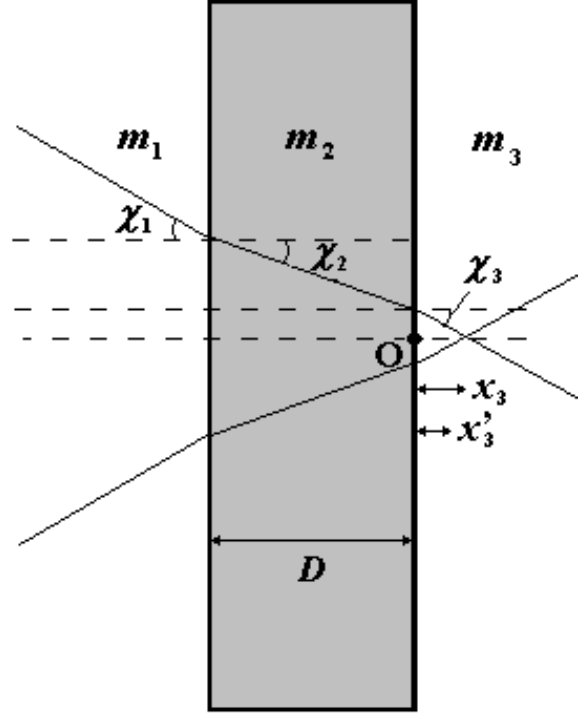
Figure 11: Optical path of the incident laser beam due to refraction.

The position corrections were applied after completion of the experiments. Another concern in computing the instantaneous velocity statistics is velocity bias. It is well known that the LDV technique introduces an inherent biasing of the velocity data towards higher values of mean velocity. This is due to the fact that faster moving seed particles have a shorter residence time in the measurement volume relative to the slower moving particles. This is corrected by weighting the instantaneous velocity signal with the corresponding burst time, τ_b. The equations used to compute turbulent quantities from the instantaneous velocity signal are given by

$$U_i = \frac{\sum u_i \, \tau_b}{\tau_b},$$

(14)
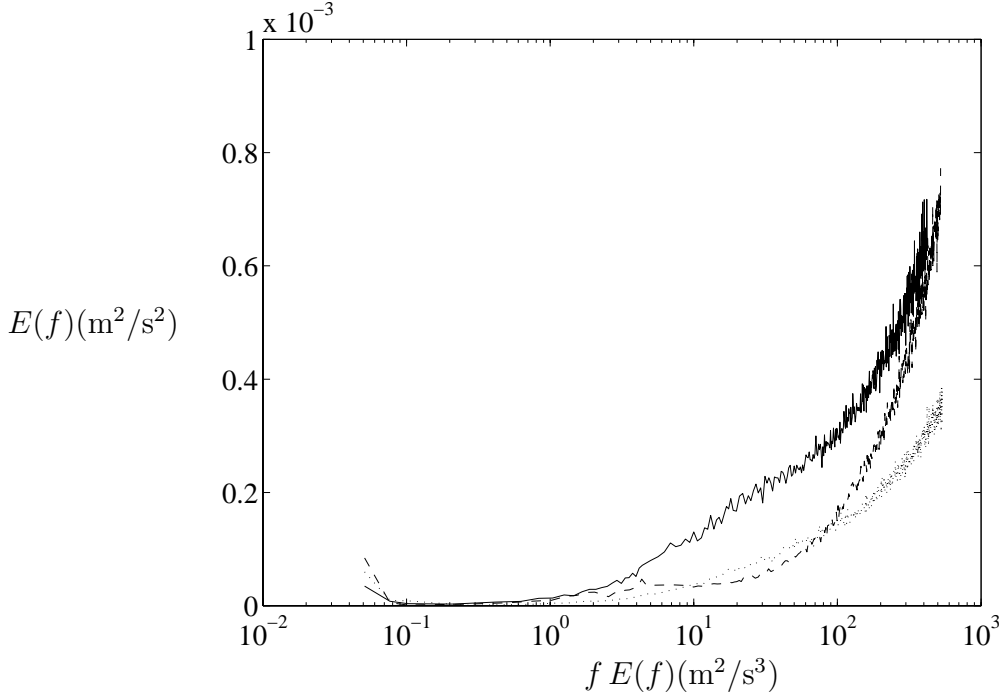
Figure 12: Power spectrum of streamwise component of velocity at $C = 1.65$ (—), $C = 2.8$ ($\cdots$) and $C = 9$ ($--$).

and

$$\sqrt{\overline{u_i'^2}} = \sqrt{\frac{\sum u_i^2 \, \tau_b}{\sum \tau_b} - U_i^2}, \tag{15}$$

Despite the presence of a surge tank immediately downstream of the pump, it was noticed that a low-frequency cycling of the mean flow rate was present (see figure 12). The frequency and amplitude of the low-frequency pulses was approximately 0.03 Hz and ± 2% of the streamwise mean velocity component, respectively. This low-frequency variation in flow rate had a negligible effect on components of fluctuation velocity near the contraction inlet. In this region the turbulent intensity is high and the streamwise component of mean velocity is a minimum. However, at the contraction outlet the turbulence intensity is damped and the streamwise component

57

of mean velocity is a maximum. In the region, $C > 6$, this pulsation introduced significant error in measured component of fluctuation velocity near the contraction outlet. In order to achieve reliable measurements of fluctuation velocity components, fluctuations less than 6 Hz are filtered out of the instantaneous velocity signal. This is accomplished by sampling the instantaneous velocity signal at 0.1 sec. intervals and averaging over the duration of the signal.

3.5 Flow conditioning

Mean velocity measurements vs. potential theory

Figure 13 illustrates a comparison of the measured streamwise mean velocity component, U_1, development down the nozzle centerline to the mean streamwise velocity predicted by potential theory, which assumes inviscid flow. At Reynolds numbers varying from 85×10^3 to 170×10^3 for this particular geometry, the viscous forces should be negligible a safe distance away from the nozzle sidewalls and thus it would be expected that the measured values agree with potential theory. The individual points correspond to measured values of U_1, and the solid lines represent U_1 evaluated from equation 8. It appears the measured values of U_1 agree well with theory, with the exception of immediately upstream of the nozzle exit where it appears the change in boundary conditions at the nozzle exit cause U_1 to slightly deviate from theory. The nozzle entrance corresponds to $C = 1$ and the nozzle exit corresponds to $C = 11.7$. However, due to optical access restrictions near the nozzle exit, it is only possible to measure U_1 up to local contraction ratio 10.7, which corresponds to 5 mm
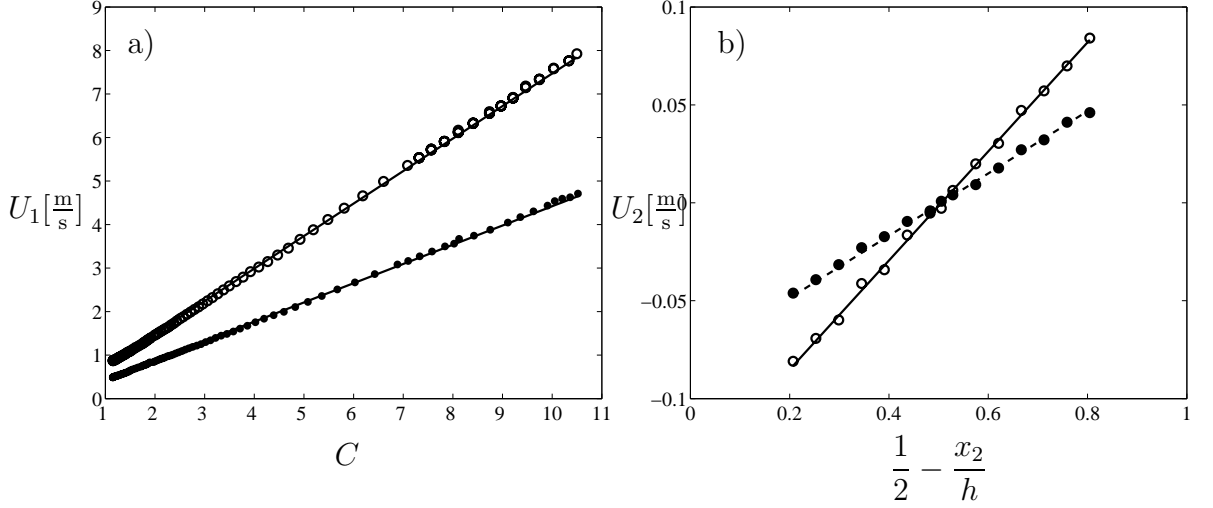
Figure 13: a) Measured x_1- component of mean velocity along the contraction centerline, Re $= 85 \times 10^3$ ($\bullet$) and Re $= 150 \times 10^3$ (o) compared to potential theory (—). b) Measured x_2- component of mean velocity at $C = 1.11$ for Re $= 85 \times 10^3$ ($\bullet$) and Re $= 150 \times 10^3$ (o) compared to potential theory (—).

upstream at the nozzle exit.

The mean velocity components, U_1 and U_2 can be closely approximated with the velocity components based on a simple quasi-one-dimensional potential flow provided by equations 8 and 9. The accuracy of the potential flow models are demonstrated in figure 13. Agreement between the models and experimental results can be attributed to the presence of uniform streamwise velocity profiles (i.e. $\partial U_1/\partial x_2 \approx 0$ and $\partial U_1/\partial x_3 \approx 0$) at the core region of the contraction, low turbulent intensities, and presence of a thin relaminarized boundary layer along the walls (Parsheh, 2001). The velocity components based on potential flow are used in the fiber orientation analysis throughout this paper.

Mean flow behind the grid

The condition of the flow immediately upstream of the grid and downstream of the grid in the constant cross-section channel is illustrated in figures 14 and 15, respectively. The streamwise component of mean velocity is strongly non-uniform upstream of the grid. Downstream of the grid, the streamwise mean velocity profile becomes increasingly uniform. Figures 16 and 17a show the mean streamwise velocity profile in the x_2 and x_3 directions inside the contraction for the Reynolds numbers studied. It is seen that the flow is uniform in the core region of the contraction. This observation will be important in developing the orientation model in the following sections. Figure 17b shows the profile of normalized mean streamwise velocity component in the x_2-direction normalized with the predicted velocity based on potential flow. This shows a slight deviation from potential flow theory in the core region. The boundary layer, δ_p, on the contraction top and bottom wall may be estimated by the development of a turbulent boundary layer on a flat plate given by

$$\delta_p = \frac{0.37\, l_p}{\mathrm{Re}_\delta^{1/5}}, \tag{16}$$

and

$$\mathrm{Re}_\delta = \frac{\rho\, \bar{U}_1\, l_p}{\mu}, \tag{17}$$

where l_p is the distance along a flat plate and $\bar{U}_1$ the average streamwise velocity along the plate. The estimated boundary layer thickness δ_p for $\mathrm{Re}_\delta = 63 \times 10^3$ is 14.3 mm at the contraction outlet. The actual boundary layer should be smaller due to the

presence of a pressure gradient in the streamwise direction. However, this estimate implies the boundary layer could have a significant influence on the mean velocity profile. The streamwise velocity profile for turbulent channel flow is approximated by

$$\frac{U_1}{U_1^*} = \frac{1}{k}\ln\frac{x_2\,U_1^*}{\nu} + \mathrm{A},\tag{18}$$

where $U_1^* = \sqrt{\tau_o}\rho$ and k, A are constants equal to 0.4 and 5.5, respectively (Nikuradse, 1933). The wall shear stress, τ_o, in a rectangular channel is modelled by

$$\tau_o = 0.0396\rho^{3/4}U_1^{7/4}\mu^{1/4}\frac{4hw}{h+w},\tag{19}$$

where h and w are the local contraction height and width, respectively. The predicted turbulent streamwise velocity profile in the x_2 direction is illustrated in figure 17b. The model gives a relatively good fit for the streamwise velocity profile in the x_2 direction at position $C = 1.18$. However, the model is valid only for fully developed turbulent channel flow and cannot accurately predict the accelerating flow in a planar contraction.
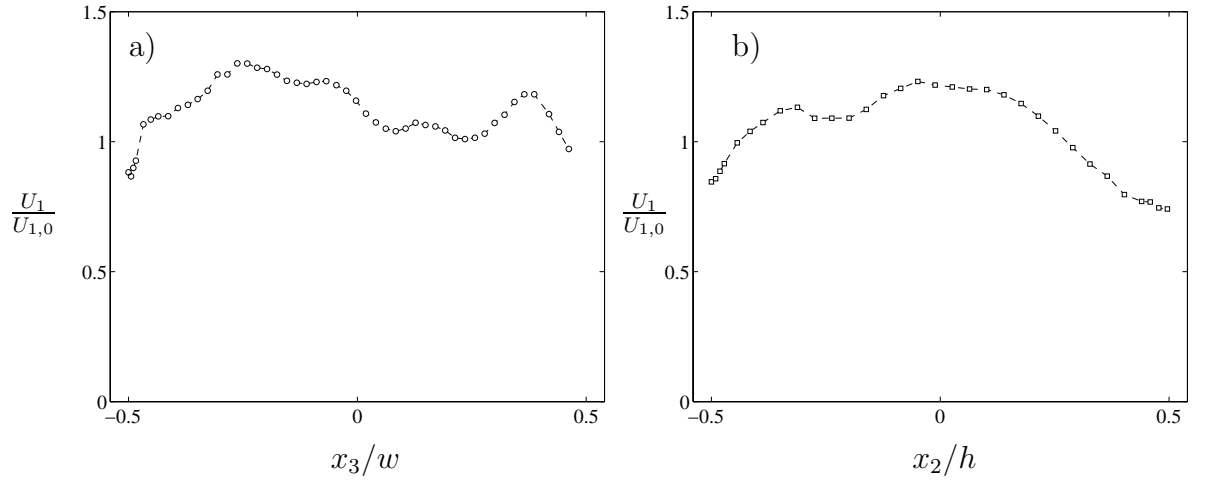
Figure 14: a) Measured streamwise mean velocity profile immediately upstream of the grid at $x_2 = 0$, $-46.8L < x_3 < 46.8L$, and $x_1 = -144L$ (o). b) Measured streamwise mean velocity profile immediately upstream of the grid at $-58L < x_2 < 58L$, $x_3 = 0$, and $x_1 = -144L$ ($\square$).
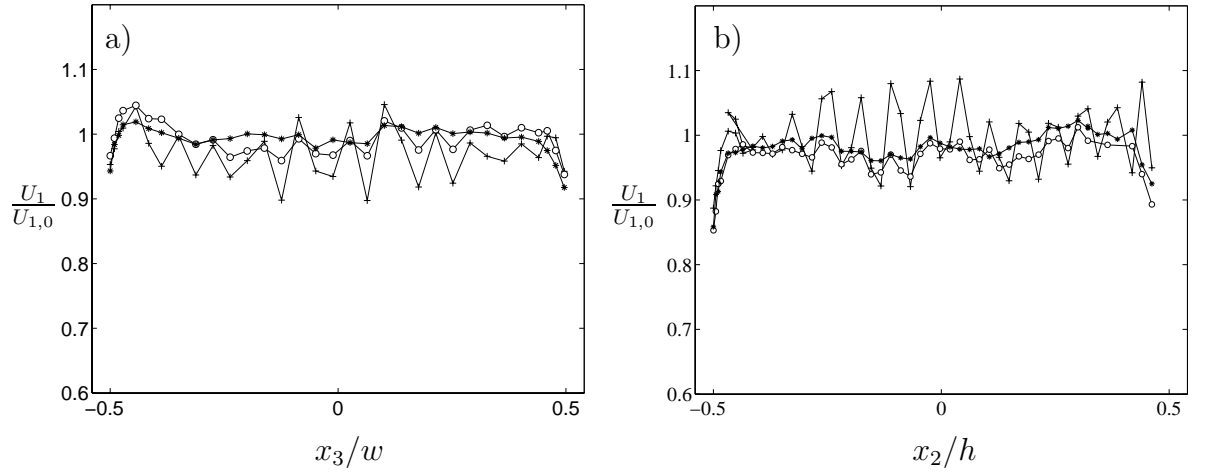
Figure 15: a) Measured streamwise mean velocity profile immediately downstream of the grid at $x_2 = 0$, $-46.8L < x_3 < 46.8L$, and $x_1 = -40L$ (*), $x_1 = -54L$ (o), $x_1 = -74L$ (+). b) Measured streamwise mean velocity profile immediately downstream of the grid at $-58L < x_2 < 58L$, $x_3 = 0$, and $x_1 = -40L$ (*), $x_1 = -54L$ (o), $x_1 = -74L$ (+).
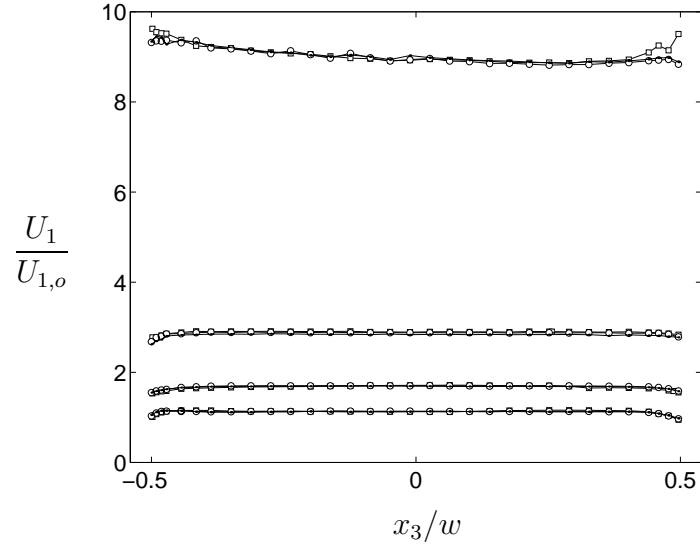
Figure 16: Mean streamwise velocity x_3-profile at C=1.18, 1.65, 2.8, and 9 at Re $=85 \times 10^3$ ($\square$), Re = 127×10^3 (o), Re = 150×10^3 (.)
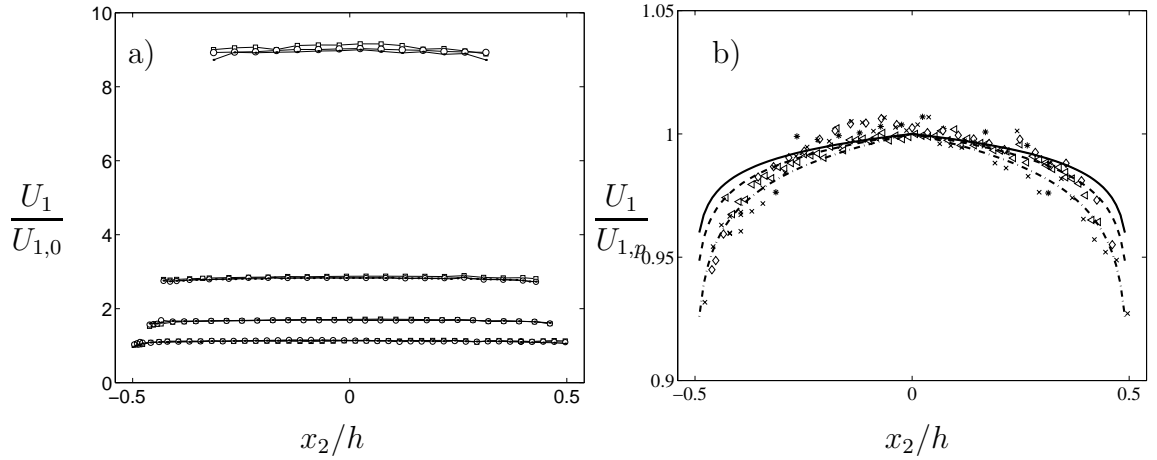
Figure 17: a) Mean streamwise velocity x_2-profile at C=1.18, 1.65, 2.8, and 9 at Re = 85×10^3 ($\square$), Re = 127×10^3 (o), Re = 150×10^3 (.). b) Normalized mean streamwise velocity profile in the x_2- direction for C=1.18 measured (x) model (see equation 18(-.-), C=1.65 measured ($\Diamond$) model (- -), C=2.8 measured ($\triangleleft$) model (—), and C=9 measured (*) at Re =85×10^3.

63

CHAPTER 4

THEORETICAL BACKGROUND

In this section we discuss the theoretical background for the dynamics of fiber orientation in laminar flow followed by application of existing fiber orientation models in turbulent flow. In this study the fibers can be assumed to be rigid since the viscous drag force is insufficient to deform the fibers. To verify this point, let us consider the dimensionless parameter $Z = 2\pi\mu(\partial U_1/\partial x_1)(2L)^4/\text{Bln}(2a_p)$, which represents the ratio of viscous drag force to the elastic recovery force of the fiber in dilute suspensions (Becker & Shelley, 2001). In this equation, B is the effective bending rigidity which is equal to the product of the Young's modulus and the second moment of area, $I = \pi d^4/64$. For a typical rayon fiber with 57μm diameter and 3.2 mm length and a Youngs modulus 2 GPa, the maximum value of Z is $O(10^{-2})$. This shows that stresses are insufficient to deform the rayon fibers.

4.1 Flow induced fiber orientation

The three-dimensional orientation of a single fiber is described by the angles (ϕ, θ) defined in figure 18. The unit orientation vector, $\mathbf{p}$, represented in cartesian coordi-
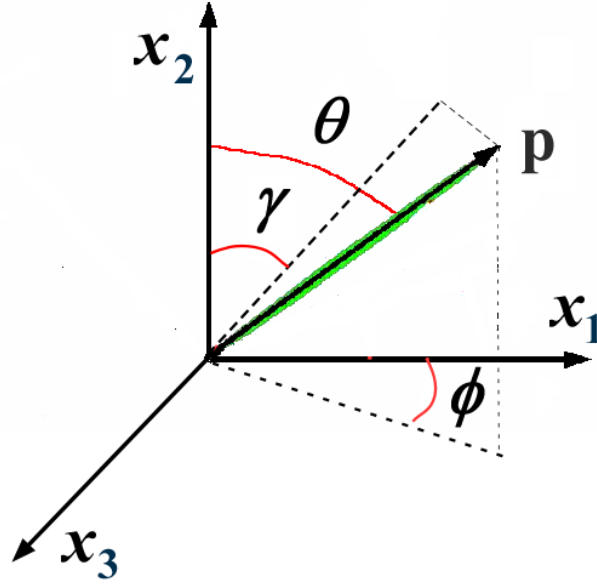
Figure 18: Coordinate system for three-dimensional fiber orientation.

nates given by

$$\mathbf{p} = \begin{pmatrix} \sin\theta\,\cos\phi \\ \cos\theta \\ \sin\theta\,\sin\phi \end{pmatrix} \tag{20}$$

Jeffery's equation gives the motion of inertialess ellipsoidal particles in flows with constant mean velocity gradient. The time rate of change of the unit orientation vector, p_i, for a single ellipsoidal particle Jeffery (1922) is given by

$$\frac{\partial p_i}{\partial t} = \Omega_{ij} p_j + \lambda (E_{ij} p_j - E_{kl} p_k p_l p_i), \tag{21}$$

65

where t denotes time, and the antisymmetric part, Ω_{ij}, and symmetric part, E_{ij}, of the velocity gradient tensors are given by

$$\Omega_{ij} = \frac{1}{2} \left(\frac{\partial U_i}{\partial x_j} - \frac{\partial U_j}{\partial x_i} \right), \tag{22}$$

$$E_{ij} = \frac{1}{2} \left(\frac{\partial U_i}{\partial x_j} + \frac{\partial U_j}{\partial x_i} \right), \tag{23}$$

and λ defined as

$$\lambda = \frac{a_p^2 - 1}{a_p^2 + 1}. \tag{24}$$

The hydrodynamic interaction coefficient, λ, is a dimensionless description of the geometry of an ellipsoid, which is approximately equal to one for high aspect ratio fibers.

The general equations for the time rate of change of the orientation angles, ϕ and θ, in three-dimensional flow are given by

$$\begin{aligned}
\frac{d\phi}{dt} = &\frac{1}{2} \left[\frac{\partial U_1}{\partial x_3} - \frac{\partial U_3}{\partial x_1} + \left(\frac{\partial U_2}{\partial x_3} - \frac{\partial U_3}{\partial x_2} \right) \cos\phi \cot\theta - \left(\frac{\partial U_1}{\partial x_2} - \frac{\partial U_2}{\partial x_1} \right) \sin\phi \cot\theta \right] + \\
&\frac{\lambda}{2} \left[\left(\frac{\partial U_1}{\partial x_3} + \frac{\partial U_3}{\partial x_1} \right) \cos 2\phi + \left(\frac{\partial U_3}{\partial x_2} + \frac{\partial U_2}{\partial x_3} \right) \cos\phi \cot\theta + \\
&\left(\frac{\partial U_1}{\partial x_2} + \frac{\partial U_2}{\partial x_1} \right) \sin\phi \cot\theta - \left(\frac{\partial U_2}{\partial x_2} - \frac{\partial U_1}{\partial x_1} \right) \sin 2\phi \right],
\end{aligned} \tag{25}$$

$$\begin{aligned}
\frac{d\theta}{dt} = &\frac{1}{2} \left[-\left(\frac{\partial U_2}{\partial x_3} - \frac{\partial U_3}{\partial x_2} \right) \sin\phi + \left(\frac{\partial U_2}{\partial x_1} - \frac{\partial U_1}{\partial x_2} \right) \cos\phi \right] + \\
&\frac{\lambda}{2} \left[\left(\frac{\partial U_2}{\partial x_1} + \frac{\partial U_1}{\partial x_2} \right) \cos\phi \cos 2\theta - \frac{1}{2} \left(\frac{\partial U_1}{\partial x_3} + \frac{\partial U_3}{\partial x_1} \right) \sin 2\phi \sin 2\theta - \right.
\end{aligned} \tag{26}$$

66

$$\left(\frac{\partial U_3}{\partial x_2} + \frac{\partial U_2}{\partial x_3} \right) \sin\phi \cos 2\theta + \frac{1}{2} \left(\frac{\partial U_1}{\partial x_1} - \frac{\partial U_3}{\partial x_3} \right) \cos 2\phi \sin 2\theta +$$

$$\frac{3}{2} \left(\frac{\partial U_1}{\partial x_1} + \frac{\partial U_3}{\partial x_3} \right) \sin 2\theta \bigg],$$

(Goldsmith & Mason 1967). The three-dimensional orientation development of large aspect ratio fibers, $\lambda \approx 1$, for flow through planar contractions, simplifies to

$$\frac{\mathrm{d}\phi}{\mathrm{d}t} = \frac{\partial U_2}{\partial x_1} \cot\theta \sin\phi - \frac{\partial U_1}{\partial x_1} \cos\phi \sin\phi, \qquad (27)$$

$$\frac{\mathrm{d}\theta}{\mathrm{d}t} = \frac{1}{2} \frac{\partial U_2}{\partial x_1} \cos\phi(1 + \cos 2\theta) + \frac{1}{4} \frac{\partial U_1}{\partial x_1} \cos 2\phi \sin 2\theta + \frac{3}{4} \frac{\partial U_1}{\partial x_1} \sin 2\theta, \qquad (28)$$

The time rate of change of the angle, γ, between the x_2- axis and the line of projection on the $x_1 - x_2$ plane (see figure 18), is given by

$$\frac{\mathrm{d}\gamma}{\mathrm{d}t} = -\frac{\partial U_2}{\partial x_1} \sin^2\gamma - \frac{\partial U_1}{\partial x_1} \sin(2\gamma), \qquad (29)$$

In addition to the trivial steady state solution, $\gamma = 0$, the other stable steady state solution is given when the fibers align with the streamlines.

Equations 27 and 28 can be greatly simplified when applied to the center symmetry plane. Therefore the fiber orientation measurements are focused in the region $|x_2| \leq L/2$, where L is the fiber length. In this region the analysis can be simplified since for most fibers $|\cot\theta/\cos\phi| \leq 20.2$ when $x_1 = 0$. The first term on the right hand side of equations 27 and 28 is at least one order of magnitude smaller than the other

terms when

$$\frac{1}{\Gamma_c} \leq \left| \frac{\cot \theta}{\cos \phi} \right| \leq \Gamma_c, \tag{30}$$

where

$$\Gamma_c = \frac{h(x_1)}{40 x_2 \tan \beta}. \tag{31}$$

Considering a random orientation distribution, at least 90% of fibers satisfy equation 30 at $x_1 = 0$ inside the region where $|x_2| \leq L$ for the contraction in figure 4. Since only a small fraction of fibers do not satisfy the above criteria, their relative contribution to the overall orientation distribution is negligible. For the range of angles outlined above, equations 27 and 28 can be approximated by

$$\frac{\mathrm{d}\phi}{\mathrm{d}t} = -\frac{1}{2} \left(\frac{\partial U_1}{\partial x_1} \right) \sin 2\phi, \tag{32}$$

$$\frac{\mathrm{d}\theta}{\mathrm{d}t} = \frac{1}{4} \left(\frac{\partial U_1}{\partial x_1} \right) \cos 2\phi \sin 2\theta + \frac{3}{4} \left(\frac{\partial U_1}{\partial x_1} \right) \sin 2\theta. \tag{33}$$

It is apparent from the above equations that ϕ is independent of θ, however, the evolution of θ depends on ϕ through cos2ϕ. The solution of equations 32 and 33 for the three-dimensional orientation distribution function in a planar contraction is shown in figure 19. As these equations imply, fibers rotate toward the stable steady state solution, $\phi = 0^\circ$ and $\theta = 90^\circ$, with angular velocity components $\mathrm{d}\theta/\mathrm{d}t \geq \mathrm{d}\phi/\mathrm{d}t$. However, the angular velocity component $\mathrm{d}\phi/\mathrm{d}t$ or $\mathrm{d}\theta/\mathrm{d}t$ is zero when the initial fiber

68
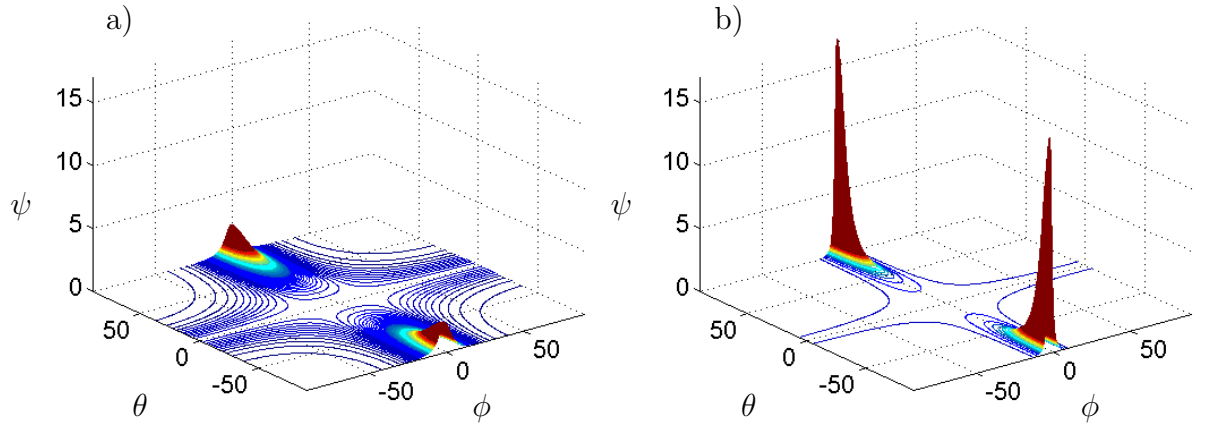
Figure 19: a) Stokes flow solution of the orientation distribution function at the contraction centerline at $C = 3.1$ a) and $C = 6.05$. b)

angle, $\phi_0 = 90^\circ$ or $\theta_0 = 0^\circ$, respectively. Solution of equation 32 is given by

$$\tan(\phi) = \tan(\phi_o)e^{-\epsilon}, \tag{34}$$

where

$$\epsilon = \int_{x_{1,o}}^{x_1} \frac{1}{U_1} \left(\frac{\partial U_1}{\partial x_1} \right) \mathrm{d}x_1, \tag{35}$$

The subscript 'o' denotes the initial condition and ϵ is the total dimensionless acceleration imposed on the flow from $x_{1,o}$ to x_1 or C_o to C. The acceleration parameter, ϵ, was constant and 3.1×10^{-6}. This equation relates the planar evolution of the orientation angle of a single fiber, ϕ, to the convective acceleration in the contraction. The solution to the equation can be obtained analytically considering potential flow. Thus, given the initial angle distribution at position x_0, one can obtain the angle distribution at any downstream position in $x_1 - x_3$ plane along the centerline. The rate of rotation of fibers toward the streamwise direction is exponential in the applied

69

total acceleration.

When there are many fibers suspended in flow, the most complete description of orientation state is the orientation probability distribution function $\psi(\mathbf{p}, t)$ defined by

$$\int_{\mathbf{p}} \psi(\mathbf{p}, t) \mathrm{d}\mathbf{p} = 1, \tag{36}$$

where $\mathbf{p}$ is defined as the unit orientation vector along the streamwise axis of the fiber (Dinh & Armstrong, 1984). The planar distribution function for fibers aligned along the $x_1 - x_3$ plane (i.e. $\theta = 90^\circ$) is given by

$$\int_0^{2\pi} \psi(\phi, t) \mathrm{d}\phi = 1. \tag{37}$$

Based on conservation principles in $\mathbf{p}$ space, the distribution function must satisfy the continuity equation given by

$$\frac{\mathrm{D}\psi}{\mathrm{D}t} + \triangledown(\dot{\mathbf{p}}\psi) = 0, \tag{38}$$

where $\triangledown$ is the gradient operator in orientation space (i.e. the gradient operator of the surface of a unit sphere).

For initially random distribution of fibers in a laminar contraction flow, following Dinh & Armstrong (1984) and based on equations 5, 8, 9, and 38, the orientation

distribution function for finite aspect ratio fibers is given by

$$\psi(\phi,\theta,t) = \frac{1}{4\pi} \left[\left(\lambda e^{-2\epsilon} + \xi^2\right) \sin^2\theta \cos^2\phi + \xi e^{\epsilon} \sin^2\theta \sin 2\phi + \lambda e^{2\epsilon} \sin^2\theta \sin^2\phi + \lambda \cos^2\theta \right]^{-3/2}$$

(39)

where

$$\xi = \frac{\partial U_2/\partial x_1}{2\partial U_1/\partial x_1}(e^{-\epsilon} - e^{\epsilon}).$$

(40)

Analogous to suspension flows with fiber-fiber interaction and Brownian motion, a Fokker-Planck type equation governs the orientation distribution of fibers in turbulent flow. The change of orientation distribution function $\psi(\mathbf{p},t)$ in turbulent flow can be modelled by

$$\frac{\mathrm{D}\psi}{\mathrm{D}t} = \nabla.\left(\dot{\mathbf{p}}\psi - \mathbf{D_r}.\nabla\psi\right),$$

(41)

where $\mathbf{D_r}$ is the rotational diffusion coefficient tensor (see e.g. Doi and Edwards 1988; Advani and Tucker 1987; Krushkal and Gallily; Olson and Kerekes 1998; Koch 1995). In this equation, the translational diffusion is neglected because the fiber concentration in the suspension flow is assumed to be uniform. The rotational diffusion tensor, $\mathbf{D_r}$, may be replaced with a scalar diffusion coefficient D_r for isotropic rotational diffusion of fibers.

The orientation distribution function provides the most general description of fiber orientation state. However, numerical simulations of the evolution of ψ are computationally expensive. Therefore, a more compact description of orientation state is desirable. Advani and Tucker (1987) show that even-order tensors give a concise description of ψ. The second- and fourth-order planar orientation tensors in

71

the $x_1 - x_3$ plane are defined as

$$a_{ij} = \int_0^{2\pi} \psi(\phi) p_i p_j \mathrm{d}\,\phi, \qquad (42)$$

and

$$a_{ijkl} = \int_0^{2\pi} \psi(\phi) p_i p_j p_k p_l \mathrm{d}\,\phi, \qquad (43)$$

respectively. These symmetric tensors represent moments of the orientation distribution function. The only non-zero components of the second order orientation tensor representing isotropic orientation in the $x_1 - x_3$ plane are $a_{11} = a_{33} = 1/2$. Advani & Tucker (1987) showed that higher order tensors lead to a more accurate representation of ψ. The equation for the development of the second order orientation tensor, a_{ij}, can be derived by combining equations 41 and 42. This evolution equation for planar orientation is given by

$$\frac{\mathrm{D}a_{ij}}{\mathrm{D}t} = \left(\Omega_{ik} a_{kj} - a_{ik}\Omega_{kj}\right) + \lambda\left(E_{ik}a_{kj} + a_{ik}E_{kj} - 2E_{kl}a_{ijkl}\right) + 2D_r(\delta_{ij} - 2a_{ij}). \quad (44)$$

Here, the symmetric orientation tensor, a_{ij}, is a function of time and position. By solving this equation, the fiber orientation can be predicted. In this expression, the fourth-order tensor component, a_{ijkl} is unknown. A closure approximation is required which relates fourth-order tensor components to the lower-order tensor components. A number of closure approximations have been put forth to predict the effect of flow field on fiber orientation using the orientation tensor approach (Doi 1978, Hinch and Leal 1976, Advani and Tucker 1990). These closure approximations are reviewed in

72

more detail in the following sections.

Approximate closure relations

The overall effect of errors induced by the closure approximations in complex suspension flows is important. These errors may be large enough to lead to inaccurate orientation predictions, regardless of the model used.

Linear closure approximation: Considering only the linear terms resulting from combining products of the second order tensor, a_{ij} and the unit tensor δ_{ij} a linear closure approximation is given by

$$\hat{a}_{ijkl} = -\frac{1}{24}(\delta_{ij}\delta_{kl}+\delta_{ik}\delta_{jl}+\delta_{il}\delta_{jk})+\frac{1}{6}(a_{ij}\delta_{kl}+a_{ik}\delta_{jl}+a_{il}\delta_{jk}+a_{kl}\delta_{ij}+a_{jl}\delta_{ik}+a_{jk}\delta_{il}) \quad (45)$$

(Hand, 1962). This expression is exact for weak flows with perfectly randomly distributed fibers. This model satisfies all the symmetry and projection properties of the second and fourth order orientation tensors. However, the model performs poorly at intermediate to highly aligned orientation states.

Quadratic closure approximation: The quadratic closure approximation is one of the most widely used and simplest closure models. The fourth order tensor may be represented by the dyadic product of two second order tensors given by

$$\hat{a}_{ijkl} = a_{ij}a_{kl}, \quad (46)$$

and is exact for strong flows where fibers are uniformly aligned in one direction (Doi, 1981). The model is shown to be inadequate for orientation predictions for weak flows with random to intermediately aligned orientation state (Advani & Tucker 1990). This model does not satisfy all the symmetry conditions and only two of the six projection properties.

Composite closure approximation Additional closure approximations have been put forth seeking to improve the robustness of the linear and quadratic models. Hinch & Leal combined the desirable features of the linear and quadratic approximation to form a composite closure approximation which is exact for both limits of orientation state given by

$$\hat{a}_{ijkl} = \frac{2}{5}(\delta_{ij}a_{kl} - a_{ij}\delta_{kl}) - \frac{1}{5}a_{ij}a_{kl} + \frac{3}{5}(a_{ik}a_{jl} - a_{il}a_{jk}) - \frac{2}{5}\sum_{m=1}^{3}(\delta_{ij}a_{km}a_{ml} + a_{im}a_{mj}\delta_{kl}).$$

(47)

The composite closure approximation fulfills two of the six symmetry properties and no projection properties.

Hybrid closure approximation The linear and quadratic models may also be combined to arrive at the following expression

$$\hat{a}_{ijkl} = (1 - f)\breve{a}_{ijkl} + f\acute{a}_{ijkl},$$

(48)

where

$$f = Aa_{ij}a_{ji} - B$$

(49)

74

(Advani & Tucker, 1990), $\breve{a}_{ijkl}$ and $\acute{a}_{ijkl}$ denote the approximation of a_{ijkl} by linear and quadratic models, respectively. For planar orientation, A and B are constants equal to 2 and 1. Strongly aligned fiber suspensions are represented well by the hybrid closure approximation.

Orthotropic closure approximation   Recently, a new set of closure approximations is introduced for predicting flow-induced fiber orientation. It is known that an approximate fourth order orientation tensor is orthotropic. This result leads to a new set of closure approximations for predicting flow-induced fiber orientation. Orthotropic closure models using the orientation tensor in its diagonal form require the principal axis of the fourth order tensor to be the same as the principal axis of the second order tensor. The advantage of this approach is that the orthotropic orientation tensor becomes diagonal, where many of its components are zero.

Due to the normalization and symmetry requirements the fourth order orientation tensor has

three independent components which may be expressed as

$$A_{11} = f_{11}(a_{11}, a_{22}) \quad A_{22} = f_{22}(a_{11}, a_{22}) \quad A_{33} = f_{33}(a_{11}, a_{22}). \tag{50}$$

This is because the fourth order tensor is orthotropic each principle fourth order component is a function of two principle values of the second order tensor.

The orthotropic smooth and fitted closure approximations are given by

$$
\begin{pmatrix} \hat{a}_{1111} \\ \hat{a}_{2222} \\ \hat{a}_{3333} \end{pmatrix} = \begin{pmatrix} -0.15 + 1.15\,a_{11} - 0.10\,a_{33} \\ 0.60 - 0.60\,a_{11} - 0.60\,a_{33} \\ -0.15 + 0.15\,a_{11} + 0.90\,a_{33} \end{pmatrix},
\tag{51}
$$

and

$$
\begin{pmatrix} \hat{a}_{1111} \\ \hat{a}_{2222} \\ \hat{a}_{3333} \end{pmatrix} = \begin{pmatrix} 0.061 + 0.371a_{11} + 0.555a_{11}^2 - 0.369a_{33} + 0.318a_{33}^2 + 0.371a_{11}a_{33} \\ 1.229 - 2.054a_{11} + 0.822a_{11}^2 - 2.261a_{33} + 1.054a_{33}^2 + 1.820a_{11}a_{33} \\ 0.125 - 0.389a_{11} + 0.259a_{11}^2 - 0.086a_{33} + 0.796a_{33}^2 + 0.545a_{11}a_{33} \end{pmatrix},
\tag{52}
$$

respectively. Both these closures have all the symmetry and normalization properties of the exact fourth order tensor.

4.2   Models of turbulence in contractions

The following is a brief review of the basic equations and theoretical background of turbulent flow inside a contraction. Prandtl (1933) put forth the first theory on the change of intensity of turbulent vortices, by applying Kelvin's circulation theorem for flow in a three-dimensional axisymetric contraction. The transverse component of a turbulent vortex is represented by a small rectangle $(\Delta x_1, \Delta x_3)$, and the streamwise component is represented by $(\Delta x_3, \Delta x_2)$. As the fluid is contracted, the lengths of

76

the sides of the rectangles vary with the local contraction ratio, C, given by,

$$\Delta x_1 \propto C, \tag{53}$$

$$\Delta x_2, \Delta x_3 \propto \sqrt{C}. \tag{54}$$

Kelvin's circulation theorem requires conservation of circulation over each rectangular loop with velocity, $U_i = (U_{1,0} + \Delta U_1, \Delta U_2, \Delta U_3)$. Therefore, the fluctuating velocity components change according to,

$$u_1' \propto \frac{1}{C}, \tag{55}$$

$$u_2', u_3' \propto \sqrt{C}, \tag{56}$$

where u_1', u_2' and u_3' are the fluctuating instantaneous fluid velocity components in the streamwise and lateral directions. The local contraction ratio, C, is analogous to the total extensional strain imparted on a fluid element at a given position inside the nozzle. These relationships, known as Prandtl's formulaes for axisymmetric contractions, predict that the downstream component of turbulence decays proportionally with the inverse of the contraction, while the transverse components increase with the half-power of the contraction.

It was shown that if the flow turbulence at the inlet to an axisymmetric nozzle is isotropic, (i.e. $u_1' = u_2' = u_3'$), and the distortion of the flow field is instantaneous, meaning the generation of turbulence in the contraction process is neglected, then as flow passes through the contraction the value of the mean-square streamwise velocity

77

fluctuation, $\overline{u_1'^2}$, should decrease and the transverse velocity fluctuation, $\overline{u_2'^2}$ and $\overline{u_3'^2}$, should increase under the same condition. However, turbulent intensity of both the streamwise and transverse velocity fluctuations with respect to U_1, decrease with increasing contraction.

A more accurate estimate is achieved by considering the vorticity equation for an incompressible fluid without mean rotation given by

$$\frac{D\omega_i'}{Dt} = \omega_j \frac{\partial U_i}{\partial x_j} + \omega_j \frac{\partial u_i'}{\partial x_j} + \nu \frac{\partial^2 U_i}{\partial x_j^2}, \tag{57}$$

where t denotes time, ω' is the vorticity due to velocity fluctuations, U_i is the mean velocity, u_1' is the fluctuating velocity, and ν is the kinematic viscosity. The rate of change of vorticity is due to vorticity production from the straining of turbulent eddies by the mean velocity gradients $\omega_j'(\partial U_i/\partial x_j)$, vorticity transfer due to eddy interaction $\omega_j'(\partial u_i'/\partial x_j)$, and vorticity diffusion due to viscosity, $\nu(\partial^2 U_i/\partial x_j^2)$. The nonlinear terms in the vorticity equation represents energy transfer between different length scales. The above equation reduces to Cauchy's equations if the deformation due to mean velocity gradients occurs so rapidly that the orientation of a vortex filament remains constant in passing through the contraction and viscosity effects are assumed negligible. Neglecting viscous dissipation of turbulent energy should not lead to significant error, since most of the turbulent kinetic energy is associated with large eddies.

Applying Cauchy's equations to predict fluctuating velocity components yields linear or rapid distortion theory (Taylor , 1935). Linear theory predicts the development

of turbulence in axisymmetric contractions as.

$$\frac{\overline{u_1'^2}}{u_{1,0}'^2} = \frac{3}{4C^2}(\ln 4C^3 - 1), \tag{58}$$

$$\frac{\overline{u_2'^2}}{u_{2,0}'^2} = \frac{\overline{u_3'^2}}{u_{2,0}'^2} = \frac{3C}{4}. \tag{59}$$

The subscript '0' denotes the inlet of the contraction, C is the contraction ratio, and U_1 is the streamwise velocity component at the flow axis.

If u_1', u_2' and u_3' denote the fluctuating velocity of a fluid element moving with instantaneous velocity $u_i = (U_1 + u_1', U_2 + u_2', U_3 + u_3')$ in a planar contraction shown in figure 4 then the conservation of circulation applied to this fluid element leads to

$$u_1' \propto \frac{1}{C}, \tag{60}$$

$$u_2' \propto C, \tag{61}$$

$$u_3' \propto 1, \tag{62}$$

For a distortion in which one of the extension ratios remain constant, as in planar contractions, the approximated expressions for development of the normal Reynolds stress components according to RDT become

$$\frac{\overline{u_1'^2}}{u_{1,0}'^2} = \frac{3}{4}C^{-1}(\ln 4C - 1), \tag{63}$$

$$\frac{\overline{u_2'^2}}{\overline{u_{2,0}'^2}} = \frac{3}{4}C + \frac{3}{8}C^{-1}(\ln 4C - \frac{1}{2}), \qquad (64)$$

$$\frac{\overline{u_3'^2}}{\overline{u_{3,0}'^2}} = \frac{3}{4}C - \frac{3}{8}C^{-1}(\ln 4C - \frac{3}{2}), \qquad (65)$$

where the subscript '0' denotes the value at the position where the distortion first was applied. Equation 63 implies that the streamwise turbulent energy decreases monotonically as the flow develops downstream. For large C the asymptotic effect on the turbulent components is the same as the effect of a large axisymmetric contraction. Thus, for large C, equations 64 and 65 are approximated by

$$\sqrt{\overline{u_2'^2}}, \sqrt{\overline{u_3'^2}} \propto \sqrt{C}, \qquad (66)$$

which is analogous to Prandtl's formulas for axisymmetric contractions. This similarity is possibly due to the fact that the vorticity ultimately is everywhere parallel to the line of the greatest extension and the u_2'- and u_3'- components are produced by more or less axisymmetric vortices (Batchelor & Proudman, 1954). Noting that in the contraction $U_1 \propto C$, the development lateral components of turbulent intensities according to RDT becomes

$$\frac{\sqrt{\overline{u_2'^2}}}{U_1}, \frac{\sqrt{\overline{u_3'^2}}}{U_1} \propto C^{-1/2}. \qquad (67)$$

CHAPTER 5

RESULTS & DISCUSSION

The main interest of this work is to model the evolution of fiber orientation state in a planar contraction based on turbulent flow kinematics. In order to make predictions, we must first understand the interaction or coupling of turbulence and rotational dispersion. In the following sections, measurements of turbulent flow field and fiber orientation distribution are presented. Also, the relative significance of the streamwise mean velocity gradient and turbulent parameters on the evolution of fiber orientation distribution in the contraction is investigated.

5.1 Turbulence in planar contraction flow

Before considering the effect of turbulence on fiber orientation, the turbulent quantities in the contraction must be characterized. It is known that integral time scale, integral length scale and components of fluctuation velocity are important turbulent parameters that influence the rotational diffusion of fibers (Olson, 1998). Since the performance of turbulent models for planar contraction flow has not been clarified earlier, existing turbulence models are compared to the measured data. The effect of

contraction angle, inlet turbulent intensity and flow Reynolds number on development

of components of fluctuation velocity are investigated.

A nearly homogenous, isotropic grid turbulent flow is introduced at the contraction inlet. At this position, the variations between the rms-velocity components are within $\pm$ 5% outside the boundary layer. It has been observed that the mean velocity components can be closely approximated with the velocity components based on a simple quasi-one dimensional potential flow, provided by equations 8 and 9 and demonstrated in figure 13 . This can be attributed to the presence of uniform streamwise velocity profiles $\partial U_1/\partial x_2$ and $\partial U_1/\partial x_3$ at the core region of the contraction, low turbulent intensity components, and presence of a thin relaminarized boundary layer along the walls (Parsheh, 2001). The velocity components based on potential flow are used in the fiber orientation analysis throughout this paper.

The decay of turbulent intensity behind a uniform grid in a straight channel has been approximated by several investigators. One such model for flow in a straight channel is given by Roach (1987),

$$\frac{\sqrt{\overline{u_1'^2}}}{U_1} = c_0 \left(\frac{l_g}{b}\right)^{-\frac{5}{7}},\tag{68}$$

where l_g is the downstream distance from the grid, b is the grid bar width, and c_o is a constant based on grid geometry. Several investigators have reported different values for the -5/7 exponent. For example, Groth & Johansson (1988) obtained -0.50 and Westin et. al. (1994) obtained -0.62. If it is assumed that decaying turbulence can be predicted by a κ-epsilon model, the exponent can be derived if the turbulent diffusion
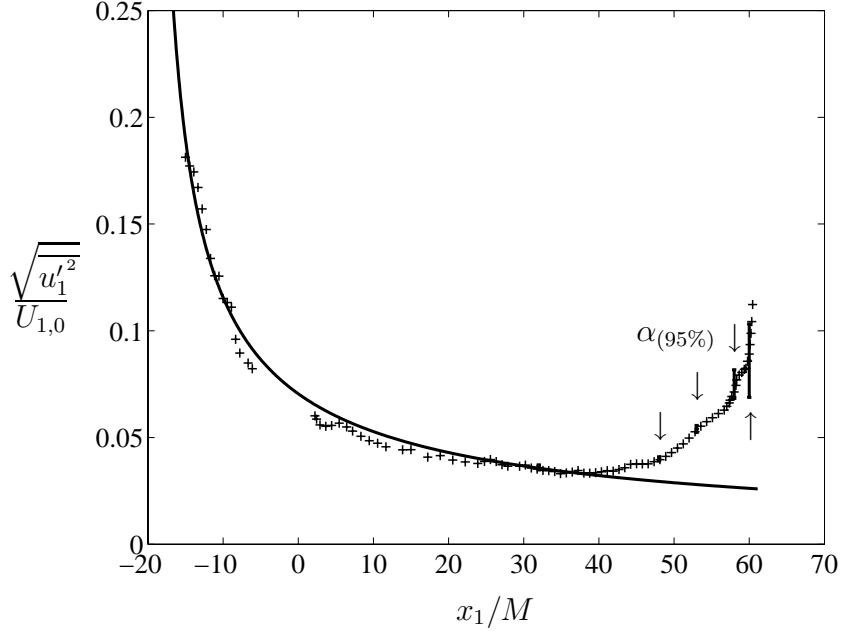
Figure 20: Development of normalized measured streamwise rms-velocity component behind the monoplanar grid (x) compared to grid turbulence decay in a straight channel based on Roach, 1987 (—). ($R^2 = 0.99$ for $-15 \leq x_1/M \leq 40$) (Error bars represent 95% confidence intervals, $\alpha_{(95\%)}$, of the measurements)

terms are neglected giving an exponent of -0.52 (Parsheh, 2001). Figure 20 shows

that, for flow at the contraction centerline, this model agrees well with the measured

data for up to $l_g = 40M$ (40 mesh sizes), where $c_o = 1.13$ as specified by Roach.

The R^2 value is 0.99 indicating the model accounts for 99% of the variability in the

measurements. The slight deviation between the measured results and the model

given by equation 68 is most likely due to dependence of c_0 on Reynolds number for

$Re > 10^4$. The agreement between development of grid turbulence in constant cross-

section channels and in the contraction suggests that the production of turbulence

is very small for $C < 2$. The general energy production term in the Reynolds stress

transport equation is given by

$$P_{ij} = -\overline{u_i' u_j'} \left(\frac{\partial U_i}{\partial x_j} + \frac{\partial U_j}{\partial x_i} \right), \tag{69}$$

Considering the velocity gradient tensor for flow in a planar contraction given by equation 5, the normal components of the energy production for turbulent flow at the contraction centerline are given by

$$P_{11} = -2\overline{u_1'^2} \frac{\partial U_1}{\partial x_1}, \tag{70}$$

$$P_{22} = 2\overline{u_2'^2} \frac{\partial U_1}{\partial x_1}, \tag{71}$$

$$P_{33} = 0. \tag{72}$$

The production of turbulent kinetic energy is given by

$$K = \left(\overline{u_2'^2} - \overline{u_1'^2} \right) \frac{\partial U_1}{\partial x_1}, \tag{73}$$

where turbulent kinetic energy is defined as

$$K \equiv \frac{1}{2} (\overline{u_1'^2} + \overline{u_2'^2} + \overline{u_3'^2}). \tag{74}$$

Considering a homogeneous, isotropic turbulent flow at inlet, equations 70 and 71 imply that the component of fluctuation velocity in the x_1-direction is likely to

decrease, and in the x_2-direction to increase, because of the negative and positive sign of the production terms in these directions, respectively. This is in agreement with linear theory. In addition, the production of turbulent kinetic energy is expected to be almost zero, since $\overline{u_1'^2}$ and $\overline{u_2'^2}$ are nearly equal in magnitude (see equation 73). This implies that for isotropic turbulent flow at inlet, the turbulent kinetic energy is expected to decrease due to negligible production and finite viscous dissipation. Further downstream, where the flow becomes significantly anisotropic, the production term becomes larger than the rate of dissipation. This relation is consistent with the measurement of components of fluctuation velocity as a function of contraction ratio, C, from inlet to the outlet of the contraction.

The effect of contraction on development of turbulent characteristics is studied experimentally. In the following paragraphs, the results of LDV measurements of turbulent flow parameters inside the contraction are considered. Figure 21 shows the development of measured rms-velocity components in the case Re $= 85 \times 10^3$ and l_r $= 20$ and the streamwise component in the case Re $= 85 \times 10^3$ and $l_r = 60$. Here, l_r is defined as the distance from the grid to the contraction inlet normalized by grid mesh size, M. The development of streamwise and lateral rms-velocity components are characterized by a minimum at $C = 2.1$ and $C = 1.7$, respectively. However, the minimum value of the streamwise component when $l_r = 60$ occurs at $C = 1.7$. This implies that the location of the minimum value is dependent on inlet turbulence conditions. Because of nearly isotropic flow at inlet, at $C < 2$ the production of turbulent kinetic energy is almost zero according to equation 73. The turbulence level
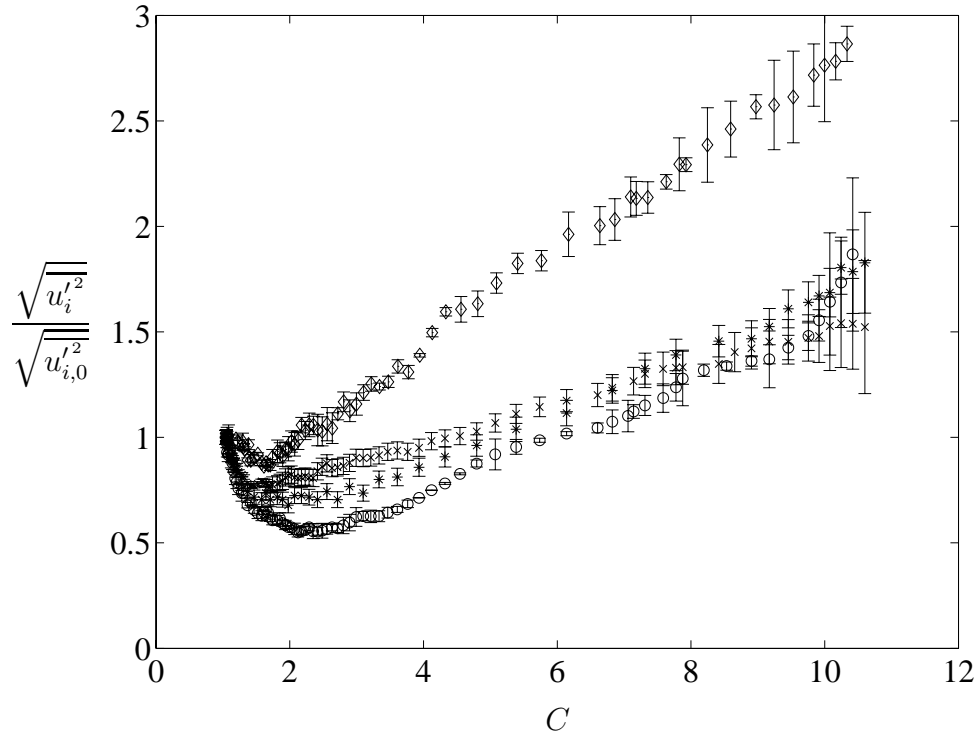
Figure 21: Development of normalized rms-velocity components along the channel centerline at Re $= 85 \times 10^3$, x_1- component, $l_r = 20$ (o), x_2- component, $l_r = 20$ (x), x_3- component, $l_r = 20$ (*), and x_1- component, $l_r = 60$ ($\diamond$). (Error bars represent 95% confidence intervals of the measurements)

in the x_1-direction should decrease whereas in the x_2-direction should increase, since the production terms in the x_1- and x_2-directions have opposite signs. Therefore, the x_1- and x_2- components of rms-velocity should not become larger than the x_3- component. This ambiguous result, shown in figure 21, is likely due to the large variability in rms-velocity near the contraction outlet. The total kinetic energy production is the sum of two terms with different signs. This implies that when an isotropic turbulent flow enters the contraction, the production of the turbulent kinetic energy would be zero immediately downstream of the contraction inlet. This leads to decay of turbulent intensity due to dissipation. Further downstream, the

86

turbulent kinetic energy increases because of anisotropy due to higher Reynolds stress component in the x_2-direction than that in the x_1- direction. This effect becomes amplified further downstream at the high contraction ratio region. The increase in the streamwise component of the turbulent kinetic energy is most likely because of inter-component distribution of energy. It is also observed that the streamwise and lateral components of turbulent kinetic energy increase along the contraction for $C > 2$. The monatonic increase of the streamwise turbulent kinetic energy for $C > 2$ is in contrast with linear theory. This development of lateral components of fluctuation velocity is in agreement with linear theory. The influence of contraction geometry half angle, β, on turbulent characteristics is found in Appendix A. Also, a detailed study of the measurement uncertainty of turbulent flow parameters is available in Appendix C.

Components of fluctuation velocity at the centerline of a two-dimensional contraction were measured in order to evaluate the accuracy of existing turbulence models. Based on the equations governing turbulent fluctuations in inhomogenous turbulent flow, a model for the development of the streamwise component of fluctuation velocity in contraction flow is given by

$$\overline{u_1'^2}_{\,\omega_o} \propto \frac{2\pi^2}{\omega_o} \left[\Upsilon \frac{\Gamma(2\eta+1)}{2l_r^{2\eta+1}} + \frac{\Gamma(\eta+1)}{2} \left(\frac{R}{2\sigma} \right)^{\eta+1} \frac{1}{U_1^2} + \frac{U_1^2}{2\eta+2} \right], \qquad (75)$$

where ω_o is a constant, R is the dimensionless Reynolds number, σ is the dimensionless time of flight, l_g is the downstream distance from grid to the contraction inlet, Γ represents the gamma function (Tsuge, 1984). This model is valid assuming that the cascade of energy into eddies is small compared to the production of energy

due to the flow, and that the mean flow is time independent reduces the evolution equation to a linear equation. The first term on the right hand side of the above equation represents the decay of streamwise component of turbulent energy generated by the grid. The second term represents the contribution of small scale eddies, (i.e. $\kappa >> 1$), which decreases as C^{-2} as predicted by classical theory, where κ is the dimensionless wavenumber. The decay of these eddies due to dissipation is a function of Reynolds number and time elapsed since production. The third term represents the contribution of large scale eddies, (i.e. $\kappa < 1$), which increases as C^2. This term is independent of Reynolds number and time elapsed and depends only on the current value of the mean velocity. In this study, the instantaneous velocity signal is measured using LDV. This model is based on the power spectrum for nearly isotropic homogenous grid generated turbulence provided by Uberoi & Corssin, 1953. The adjustable parameters, Υ and η, are chosen to fit the inlet turbulent condition. Figure 22 shows that predictions based on equation agree qualitatively with measurements. However, the model underpredicts the rate of decay of grid generated turbulence, which leads to the deviation between the model and measurements. The advantage of this model is the ability to predict the increase in large scale eddies with increasing C. For the region $C > 3$, the model predicts that the majority of turbulent energy is represented by these large scale eddies.

The turbulent intensity at the contraction inlet was changed by repositioning the grid relative to the contraction inlet. In the following paragraphs, the effect of inlet turbulent length scale on turbulent flow characteristics in a planar contraction
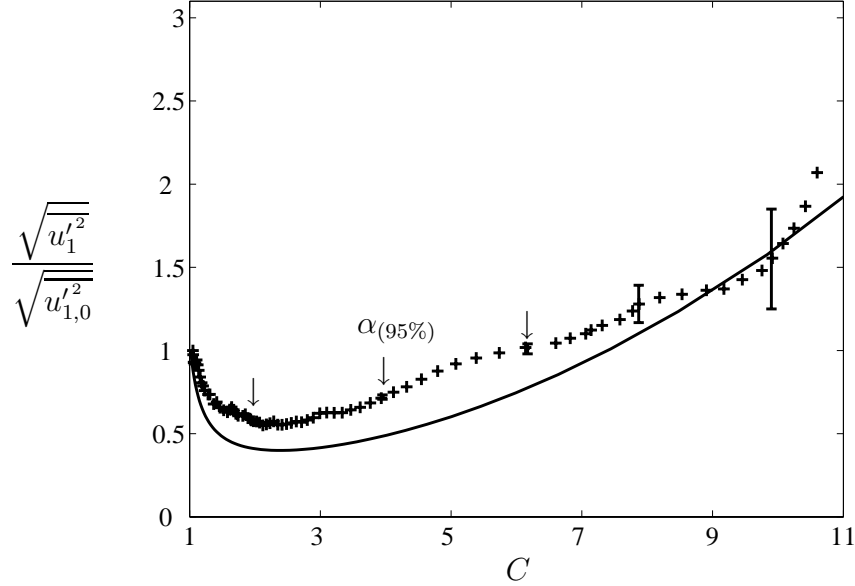
Figure 22: Prediction of normalized streamwise fluctuation velocity component at $Re = 85 \times 10^3$: model(—)(Tsuge, 1984), measured (+). (Error bars represent 95% confidence intervals, $\alpha_{(95\%)}$, of the measurements)

is investigated. The downstream development of the streamwise turbulent intensity component along the contraction centerline for $Re = 85 \times 10^3$ and $l_r = 20$ and for $Re = 85 \times 10^3$ and $l_r = 60$ are shown in figure 23. Moving the grid position further downstream from $l_r = 60$ to $l_r = 20$ nearly doubles the inlet turbulent intensity. The turbulent intensity for case $Re = 170 \times 10^3$ and $l_r = 20$ follows approximately the corresponding values for the case $Re = 85 \times 10^3$ and $l_r = 20$. The streamwise turbulent intensity, $T_1 \equiv \sqrt{\overline{u_1'^2}}/U_1$, decreases monotonically to less than 1.5% at the contraction outlet. The development of normalized turbulent intensity, $T_1^* \equiv (T_1 - T_{1,e})/(T_{1,0} - T_{1,e})$ with respect to $C^* \equiv C-1$, for different flow Reynolds numbers ($Re = 85 \times 10^3$ and $Re = 85 \times 10^3$), contraction half angles, and inlet turbulent conditions is shown in figure 24. The quantities $T_{1,0}$ and $T_{1,e}$ represent the turbulent intensity at the inlet and outlet, respectively. These cases closely follow
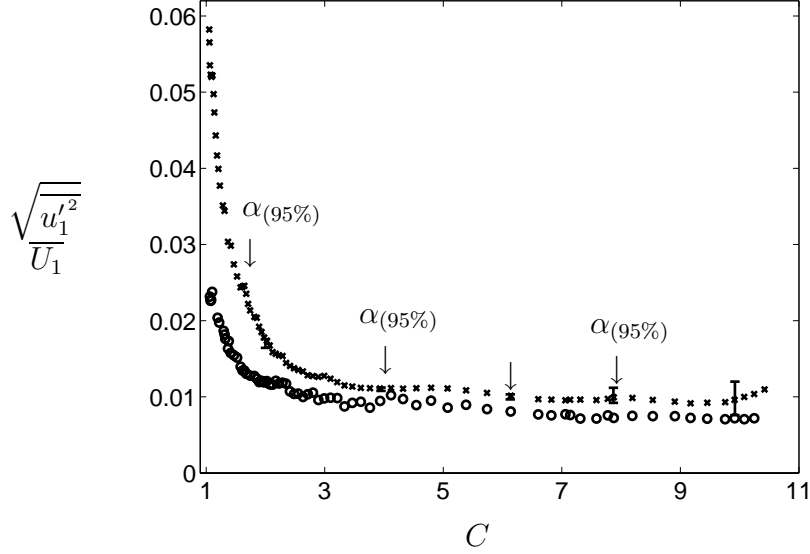
Figure 23: Downstream development of streamwise component of turbulent intensity along the channel centerline $Re = 85 \times 10^3$ and $l_r = 60$ (o), $Re = 85 \times 10^3$ and $l_r = 20$ (x). (Error bars represent 95% confidence intervals of the measurements)

an exponential decaying function given by, $e^{-1.6C^*}$, based on a leased squares fit to the measurements. The exponential decay closely follows the power law decay for grid generated turbulence given by Roach at $C < 2$. In the region $C > 2$, turbulent production and transfer of energy between components leads to slightly better agreement with measurements for the exponentially decaying function. Since the turbulent energy is spread over a broad frequency band, it is necessary to investigate the Eulerian integral time and length scales. Correlations of the instantaneous velocity signal separated in space and time contain a great deal of information about the underlying structure of turbulent flows. The Eulerian integral length scale is an important fundamental turbulence parameter which is known to influence the rotational diffusion of fibers. Physically, it represents the length scale of the most energy rich eddies
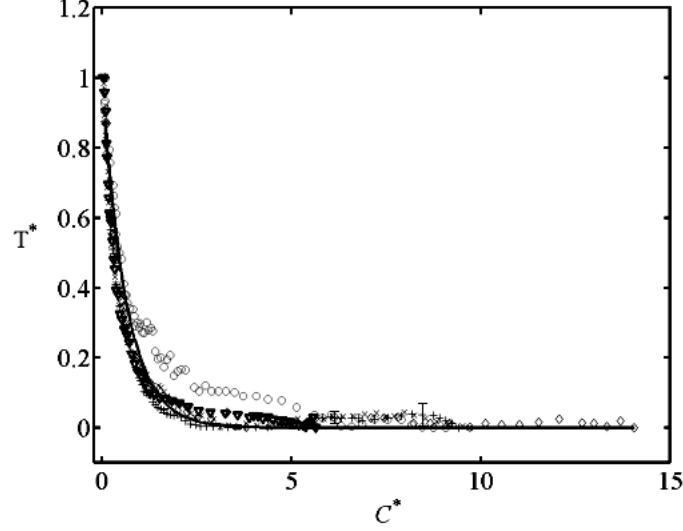
Figure 24: Streamwise component of turbulent intensity along the contraction centerline for $\mathrm{Re} = 85 \times 10^3$, $l_r = 60$, and $\beta = 8.4^o$ (o); $\mathrm{Re} = 85 \times 10^3$, $l_r = 20$ and $\beta = 8.4^o$ (+); $\mathrm{Re} = 170 \times 10^3$, $l_r = 20$ and $\beta = 8.4^o$ (×); $\mathrm{Re} = 85 \times 10^3$, $l_r = 20$ and $\beta = 8.15^o$ ($\triangledown$); $\mathrm{Re} = 85 \times 10^3$, $l_r = 20$, and $\beta = 8.8^o$ ($\lozenge$); the exponential decaying curve fitted to data, $\mathrm{e}^{-1.6C^*}$ (—). (Error bars represent 95% confidence intervals of the measurements)

comprising the turbulent motion. The streamwise integral time scale, τ, is defined as

$$\tau = \int_0^\infty \mathrm{R}_{11}(\Delta t)\mathrm{d}(\Delta t),\tag{76}$$

where the autocorrelation coefficient, R_{11}, is given by

$$\mathrm{R}_{11}(\Delta t) = \frac{\overline{u_1'(t)u_1'(t+\Delta t)}}{\overline{u_1'}^2}.\tag{77}$$

Direct measurement of length scales requires the simultaneous acquisition of at

least two spatially separated velocity measurements. However, indirect measurement

of integral length scales may be obtained by Taylor's approximation, which allows

91

estimation of turbulent length scales from measurement of temporal time scales using a single-point method (Liou & Santavicca, 1985). The change in spatial form of a fluid element during its motion past a fixed probe may be considered so small that the fluid element is effectively 'frozen', provided that the flow field is isotropic and homogenous, the mean velocity in the flow field is stationary, and the velocity fluctuation is very small compared to the mean velocity. If these conditions are met, the signal changes with time are due only to spatial non-uniformities being convected past the beam intersection at speed U_1.

Taylor's hypothesis is given by

$$\Delta t = \int_{x_{1,1}}^{x_{1,2}} \frac{\mathrm{d}x_1}{U_1(x_1)}, \tag{78}$$

where $x_{1,2}$ denotes the point of measurement and $x_{1,1}$ is the unknown upstream position. Taylor's approximation is valid for nearly isotropic turbulence far behind a periodic grid (Uberoi & Corrsin, 1953). The integral length scale, Λ, can be estimated from the integral time scale, by

$$\Lambda = \int_0^\infty \mathrm{R}_{11}(\Delta x_1)\mathrm{d}(\Delta x_1), \tag{79}$$

where $\Delta x_1 = x_{1,2} - x_{1,1}$. The cross-correlation coefficient, R_{11}, evaluated from the time the instantaneous streamwise velocity signal is collected from LDV measurements (see figure 25). This figure clearly shows the dissipation of small scale eddies and production of large scale eddies with increasing C. The time and length scales

92
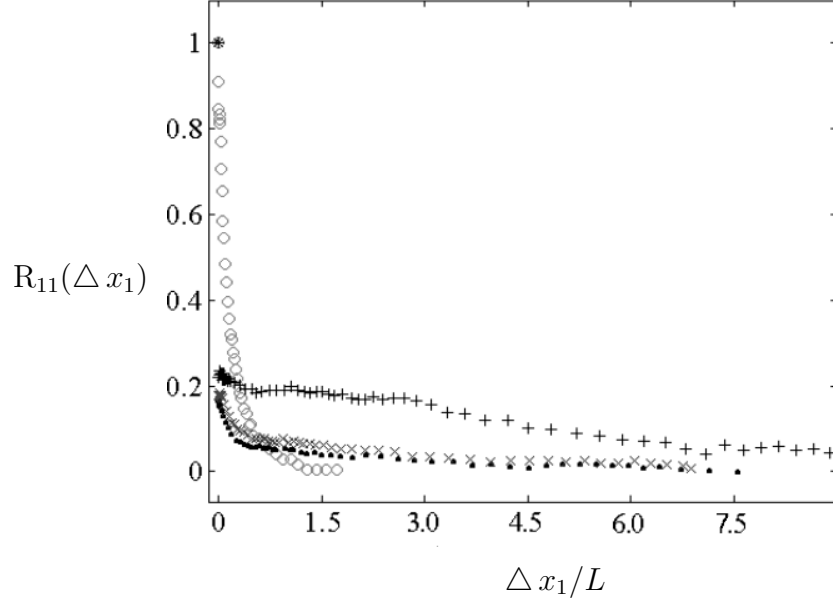
Figure 25: Cross-correlation coefficient $R_{11}(\triangle x_1)$ at $C = 1.05$ (o), $C = 2.17$ (●), $C = 4.77$ (x) and $C = 8.3$ (+) for Re $= 85 \times 10^3$.

are approximated based on equations 76 and 79. The variation of these scales along the contraction is presented in figures 26 and 27. The integral length scale of the streamwise component of fluctuation velocity, Λ, increases by a factor of seven in the contraction, independent of the Reynolds number. This increase in the scale is due to dissipation of small eddies and stretching of turbulent eddies in the contraction. It is observed that the integral length scale is of the order of the fiber length at the channel inlet, and becomes very small in comparison to the scale of a fibers at higher contraction ratios. The integral length scale is observed to range between $0.8L$ and $3.4L$ for the conditions investigated. The downstream increase in the length scale is due to dissipation of small eddies and stretching of turbulent eddies in the con-traction. Furthermore, the integral time scale increased from $2L/U_{1,0}$ at the inlet to $11L/U_{1,0}$ at the outlet. Based on a paired t-test of the mean, there is a 28% and

93
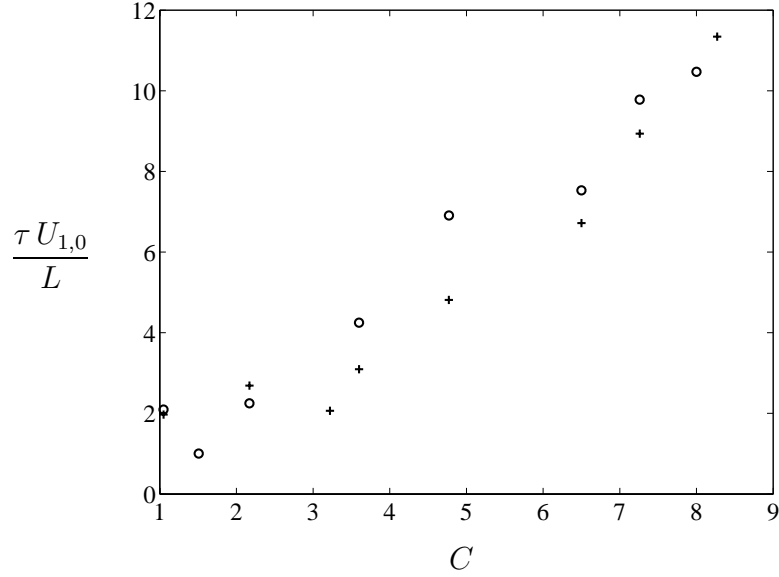
Figure 26: Downstream development of the integral time scale normalized with inlet mean streamwise velocity, $U_{1,0}$, and fiber half length, L, for Re=85 x 10^3 (+); Re = 150 x 10^3 (o).
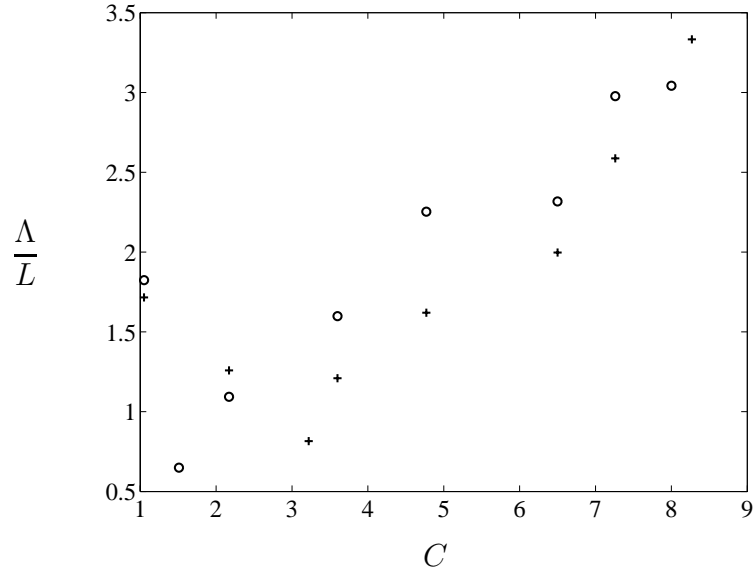
Figure 27: Downstream development of integral length scale normalized with fiber half length, L, for Re = 85 x 10^3 (+), Re = 150 x 10^3 (o).

21% probability that the integral time and length scales are independent of Reynolds number, respectively.
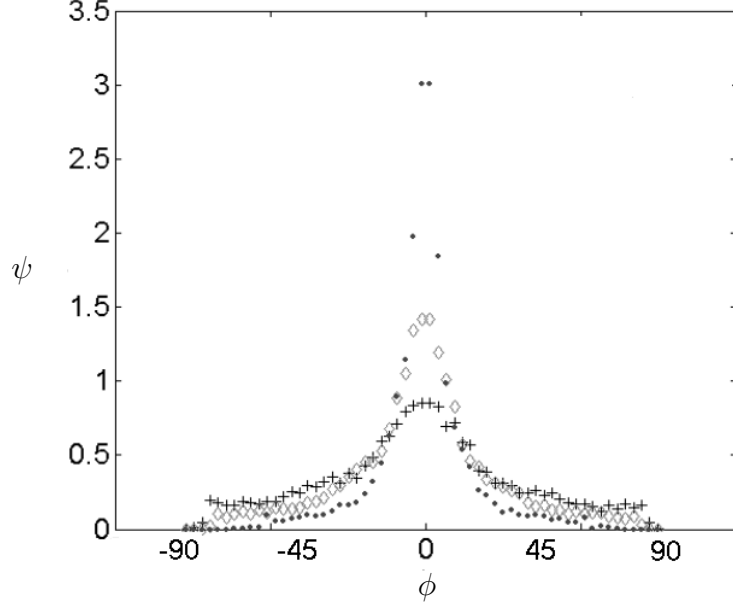
Figure 28: Downstream development of the normalized orientation distribution, ψ, at $C = 2.2$ (+), $C = 3.6$ ($\Diamond$), and $C = 8.5$ ($\bullet$) for Re $= 85 \times 10^3$.

5.2 Flow induced orientation in a planar contraction

In the following paragraphs, the results of direct measurement of flow-induced orientation in a planar contraction are presented. In order to provide thorough analysis of the results, the dynamics of fiber orientation in laminar flow is considered. This is followed by application of existing fiber orientation models in turbulent flow.

The measured orientation distribution function, ψ, at different downstream positions in the contraction is shown in figure 28. These results show that the fibers become more oriented in the stream-wise direction when the contraction ratio increases. This is expected as the rate of rotation of fibers towards the steamwise direction is exponential in the applied total acceleration.

Analytical theory for flow-induced orientation state based on Stokes flow was also compared with the results of the experiments. The theory predicts fiber orientation

96

distribution in the contraction plane, $x_1 - x_3$ plane, for two-dimensional flow. The mean velocity components at the core region of the contraction, U_1 and U_2, can be closely approximated with the velocity components based on a simple quasi-one-dimensional potential flow. The velocity components based on potential flow are used in the fiber orientation analysis throughout this paper.

In this study, the single component of the fourth order orientation tensor, a_{1111}, is used to quantify the development of orientation anisotropy. The value of this component varies between 0 and 1.0 when all fibers are oriented in the x_2- and x_1- direction, respectively. For a random distribution of fibers this value is 0.375. This parameter is used to compare downstream development of $\psi(\phi)$ based on equations 27 and 28, and based on equation 32. An initially randomly oriented fiber suspension flow is modelled along a plane parallel to the contraction centerplane at $x_2 = L$. The results are presented in figure 29. The overlap between the computed orientation parameters implies that equations 32 and 33 are a good approximation to equations 27 and 28, and therefore, do not introduce significant error to the analysis.

5.3 Evaluation of rotational diffusion coefficient, D_r, from turbulence measurements

The focus of this study is to model the orientation distribution of rigid fibers due to turbulence in planar contraction flow. However, it is known that fiber inertia influences the dynamics of many dilute suspension flows (Koch, 2001). In this work, fibers are similar in density to the fluid in order to minimize the effect of inertia. The density ratio of a suspension of rayon fibers in water is 1.16. The magnitude of
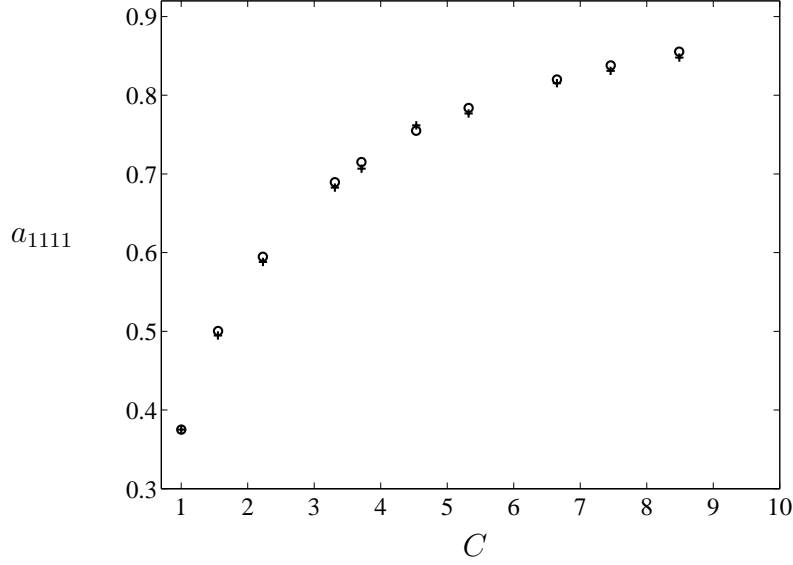
Figure 29: Development of fiber orientation parameter, a_{1111}, for ϕ along a line parallel to the centerline at $x_2/L = 1$ for Stokes flow computation based on equation 32 (o), and based on equations 27 and 28 (+).

Re and Re_f are of $O(10^5)$ and $O(10^2)$ at the contraction outlet, respectively. Fiber inertia may still be important considering, $\text{Re}_f > 1$.

The Stokes number is useful in predicting how closely suspended fibers follow the flow. Stokes number, St, is defined as the ratio of particle response time, τ_p, to the system response time, τ_a. Suspensions with St < 1 are characterized by fiber motion that closely follows the fluid motion. The particle response time and system response time for the suspension flow considered in this work are given by,

$$\tau_p = \frac{d^2}{\nu},\tag{80}$$

and

$$\tau_a = \left(\frac{\partial U_1}{\partial x_1}\right)^{-1},\tag{81}$$

98

respectively. The Stokes number is given by,

$$\text{St} = \frac{\tau_p}{\tau_a} = \frac{d^2 \frac{\partial U_1}{\partial x_1}}{\nu}. \tag{82}$$

The particle response time is 3.9×10^{-3} sec. and the system response time varies from 1.23 sec. to 1.1×10^{-2} sec.. Consequently, the Stokes number increases exponentially from 3.2×10^{-3} at the contraction inlet to 0.34 at the outlet. In the region near the contraction inlet, $\text{St} << 1$, indicating that fiber inertia has a negligible effect on fiber motion. Fiber inertia has only a slight effect in the region of strong streamwise rate of strain immediately upstream of the contraction outlet. Therefore, it is understood that fiber inertia has a negligible effect on orientation in these experiments. A more detailed investigating of the influence of inertia and the fiber slip velocity is located in Appendix D.

Analogous to suspension flows with Brownian motion, the time rate of change of the orientation distribution function $\psi(\mathbf{p}, t)$ in turbulent flow is modelled by a Fokker-Planck type equation (see Doi & Edwards, 1988, Advani & Tucker 1987 and Olson & Kerekes 1998), given by

$$\frac{\text{D}\psi}{\text{D}t} = D_r \bigtriangledown^2 \psi - \bigtriangledown(\dot{\mathbf{p}}\psi), \tag{83}$$

where D_r is the rotational diffusion coefficient. In this equation, translational diffusion is neglected because the fiber concentration in the suspension flow is assumed to be uniform. Depending on the flow conditions, the diffusion term on the right hand side

of equation 83 represents the randomizing effect of either the Brownian motion (Doi
& Edwards 1988) or the turbulent eddies (Olson & Kerekes 1998). In the present
study, this model implies that fiber orientation development is an interplay between
the arranging effect of the mean velocity gradient field and the randomizing effect of
the turbulent eddies.

The evolution of ψ along the contraction centerplane is obtained from a convection-
dispersion equation given by

$$\frac{\partial \psi}{\partial x_1} = \frac{D_r}{U_1} \frac{\partial^2 \psi}{\partial \phi^2} + \frac{1}{U_1} \frac{\partial U_1}{\partial x_1} \frac{\partial}{\partial \phi} \left(\frac{1}{2} \psi \sin(2\phi) \right). \tag{84}$$

Orientation measurements are compared with theory in order to better understand
the effect of turbulence on the rotational dispersion of fibers in suspension. For the
flow at the contraction centerline, the convection-dispersion equation is solved using
a finite difference approximation. In this computation, the flow is one-dimensional
in the streamwise direction. The values of U_1 and $\partial U_1 / \partial x_1$ at the fiber center are
used in this computation. The purpose of this analysis is to predict D_r, which is
determined by a least square fit of the model to the measured ψ. Therefore, the
measured orientation distribution function at $C = 1.1$ is used as the initial profile
in the model. It is observed that the orientational diffusion is highly dependent on
inlet turbulence properties and local contraction ratio. In this figure, the computed
orientation parameter is shown versus the contraction ratio at the center of mass of
the fiber. After considering several functional forms, $D_r(C)$ is approximated by an

exponentially decaying function. This function is given by

$$D_r = \frac{\sqrt{\overline{u'^2_{1,0}}}}{2L} e^{-0.95\,C} \tag{85}$$

where $\sqrt{\overline{u'^2_{1,0}}}$ denotes the streamwise component of rms-velocity at the inlet. The exponent -0.95 gives the best fit to measured cases. Figure 30 shows development of measured orientation parameter, a_{1111}, for the three measured cases. The measured values or orientation tensor components may be found in Appendix C. The model for D_r is shown to be accurate in predicting orientation anisotropy for a given inlet flow condition.

It is interesting to consider why this exponential decaying form of D_r works so well to predict the rotational diffusion of fibers. First, we know that the couple necessary to rotate a slender fiber in Stokes flow scales as L^3 (Batchelor, 1971). The integral time scale τ is given by ΛU_1 in the model by Olson & Kerekes. Therefore, $\overline{u'^2_1} \tau \Lambda/(2L)^3$ can be written as $\sqrt{\overline{u'^2_1}}\,\mathrm{T}_1 \Lambda^2/(2L^3)$. This relation may be approximated by $\sqrt{\overline{u'^2_1}}\,\mathrm{T}_1/(2L)$, since Λ is the same order of magnitude as L throughout the contraction. Also, we have shown that normalized turbulent intensity, T^*, decays exponentially to the $-1.6C^*$ power. Therefore, the model proposed in equation 85 is consistent with turbulence measurements and existing theory. This model works well for the range of flow Reynolds number, contraction half angle, and inlet turbulent conditions. However, it is well known that grid generated turbulence decays as a function of streamwise position from the grid, l_g. Therefore, it is likely that the model presented above will yield accurate predictions of orientation state over a

101
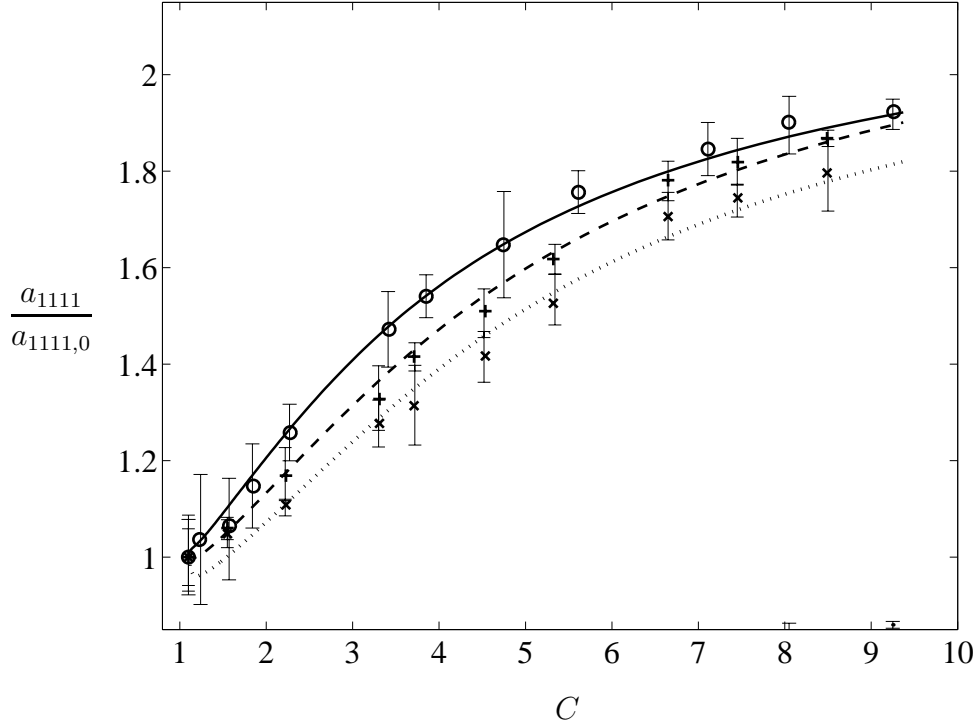
Figure 30: Comparison of experimental a_{1111}, for $Re = 85 \times 10^3$ and $l_r = 60$ measured (x) model (...), $Re = 85 \times 10^3$ and $l_r = 20$ measured (o) model (—) and $Re = 170 \times 10^3$ and $l_r = 20$ measured (+) model (- -) using the measured distribution at $C = 1.1$ as the initial value. All graphs are normalized by the measured value at $C = 1.1$, $a_{1111,0}$. (Error bars represent 95% confidence intervals of the measurements)

finite range of contraction half angle. Further work needs to be done to determine the range of contraction half angles, fiber length, flow Reynolds number, and inlet turbulent conditions for which equation 85 is valid.

5.4 Effect of turbulence on orientation

In the present study, turbulent flow characteristics along the centerline of the contraction were measured to determine the influence of turbulence on fiber orientation development. The rotational diffusion coefficient, D_r, has been modelled by several investigators. Krushkal & Gallily used a relationship based on Kolmogorov's local isotropy hypothesis for small eddies and from dimensional analysis derived the fol-

lowing expression

$$D_r \approx \left(\frac{\epsilon_t}{\nu}\right)^{1/2} \tag{86}$$

where ϵ_t is the dissipation rate of turbulent energy per unit mass, given by

$$\epsilon_t = \nu \sum_{i,j} \overline{\left(\frac{\partial u_i'}{\partial x_j}\right)^2}, \tag{87}$$

(Hinze, 1975). Olson (2001) proposed the rotational diffusion coefficient is given by

$$D_r \approx 0.7 \left(\frac{4\epsilon_t}{15\nu}\right)^{1/2}. \tag{88}$$

Olson & Kerekes (1998) suggest that for long fibers in isotropic turbulent flow, the rotational diffusion coefficient is given by

$$D_r = 24\overline{u_1'^2}\frac{\tau}{(2L)^2}\frac{\Lambda}{(2L)}\left(\mathrm{erf}\left(\frac{\pi^{1/2}(2L)}{2\Lambda}\right) + \frac{16}{\pi^2}\left(\frac{\Lambda}{2L}\right)^3\left(1 - \mathrm{e}^{-\pi(2L)^2/4\Lambda^2}\right)\right.$$
$$\left.+ \frac{2}{\pi}\frac{\Lambda}{2L}\left(\mathrm{e}^{-\pi(2L)^2/4\Lambda^2} - 3\right)\right) \tag{89}$$

This model implies D_r is a function of the integral time scale, τ, integral length scale, Λ, and streamwise component of fluctuation velocity. The models given by equations 86 and 90 are evaluated from the measured turbulent characteristics in the contraction. It was observed that at the region close to the contraction inlet, D_r based on the model given by equation 90 is at the same order of magnitude as the

value calculated by equation 84. However, these two values of D_r are not exactly the same, which may be explained by the fact that the above model is not valid when the integral length scale Λ is larger than the fiber length scale, L. The accuracy of the rotational diffusion model given by equation 86 is evaluated using the measured streamwise velocity time signal to estimate ϵ_t. It is assumed that small scale eddies are locally isotropic in the contraction. The value of D_r based on this model is two orders of magnitude larger than the value obtained from measured orientation distribution by equation 84.

In the following paragraphs, the effect of turbulence on the development of orientation distribution function is investigated. This is done by comparing a_{1111} with a_{1111} for Stokes flow evaluated by equations 37, 43 and 84 (denoted by $a_{1111,s}$). The orientation distribution function measured at $C = 1.1$ is used as initial condition for evaluation of $a_{1111,s}$. Figure 31 shows the development of orientation parameter given by Stokes flow and a_{1111}. Stokes flow overpredicts the orientation anisotropy in the contraction, due to the absence of turbulence. The small deviation between the computed orientation distribution functions by Stokes flow in figure 31 is due to unequal anisotropy of the initial profiles. The orientation distribution, ψ , measured downstream of the contraction inlet, $C = 1.1$, is slightly anisotropic and differs between each case. The anisotropy in orientation distribution at this position can be attributed to the small flow contraction in the straight channel due to boundary layer growth. It is of particular interest to study the development of a_{1111} through the contraction in terms of the Reynolds number. As shown in figure 31, increasing the
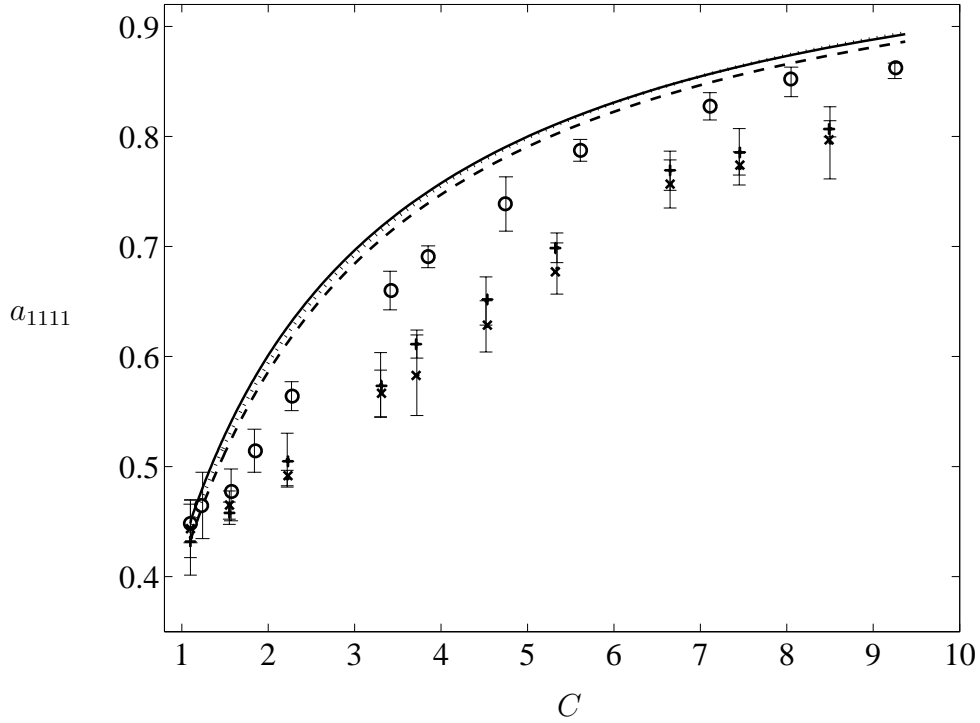
Figure 31: The comparison of the development of experimentally obtained values of a_{1111} and the development of a_{1111} when $D_r = 0$ (Stokes flow) calculated from initial ψ for the three cases. Re $= 85 \times 10^3$ and $l_r = 60$: measured (x) , computed $(- -)$; Re $= 85 \times 10^3$ and $l_r = 20$: measured (o), computed $(—)$; Re $= 170 \times 10^3$ and $l_r = 20$: measured (+), computed (...). (Error bars represent 95% confidence intervals of the measurements)

Reynolds number from 85×10^3 to 170×10^3 with $l_r = 20$ leads to a slight decrease in orientation anisotropy. This is in agreement with many other investigations of similar problems (*i.e.* Olson et. al., 2004).

The effect of turbulent characteristics at the contraction inlet on orientation distribution is studied by changing the grid position relative to the contraction inlet, l_r, while keeping the Reynolds number constant at 85×10^3. At $l_r = 60$, due to lower turbulent intensity along the contraction centerplane, a larger number of fibers align with the streamwise direction compared to $l_r = 20$. This leads to a higher value of orientation parameter in this set-up.

It is important to identify the region in the contraction where rotational diffusion has a significant influence on the dynamics of fiber orientation. Figure 32 shows the downstream development of the ratio of a_{1111} and evaluated orientation parameter in Stokes flow, $a_{1111,s}$, for case Re $= 85 \times 10^3$ and $l_r = 60$. The measured ψ at $C = 1.6$ is used as the initial profile for Stokes flow evaluation. As it is seen from this figure, the orientation parameter, a_{1111}, nearly follows the Stokes flow development at $C > 1.6$. To show the actual comparison of the orientation distribution functions, the normalized polar diagram of the measured and computed distribution functions at $C = 3.4$ and $C = 5.6$ are presented in figures 33 and 34, respectively. The two plots nearly overlap confirming the conclusion from figure 32. Similarly, the development of orientation distribution at Re $= 85 \times 10^3$ and Re $= 170 \times 10^3$ for $l_r = 20$ follow the Stokes flow development at $C > 3.3$, as shown in figure 35. Comparison of the results in figures 32 and 35 shows that for the case when $l_r = 60$, the randomizing effect of
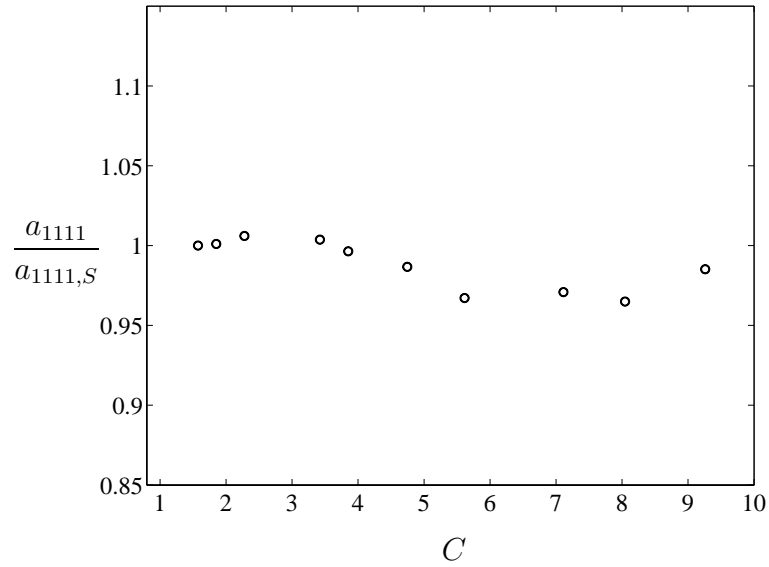
Figure 32: Development of the ratio of experimentally obtained values of a_{1111} to prediction by Stokes flow, where measured ψ at $C = 1.6$ is used as the initial profile for case Re $= 85 \times 10^3$ and $l_r = 60$.
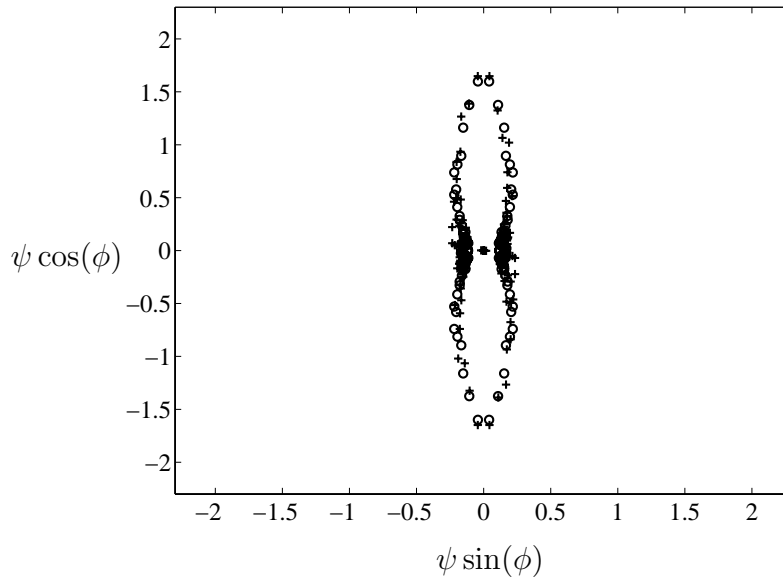
Figure 33: Measured (o) and computed (+) orientation distribution function at contraction ratio 3.4 and Re $= 85 \times 10^3$ and $l_r = 60$.
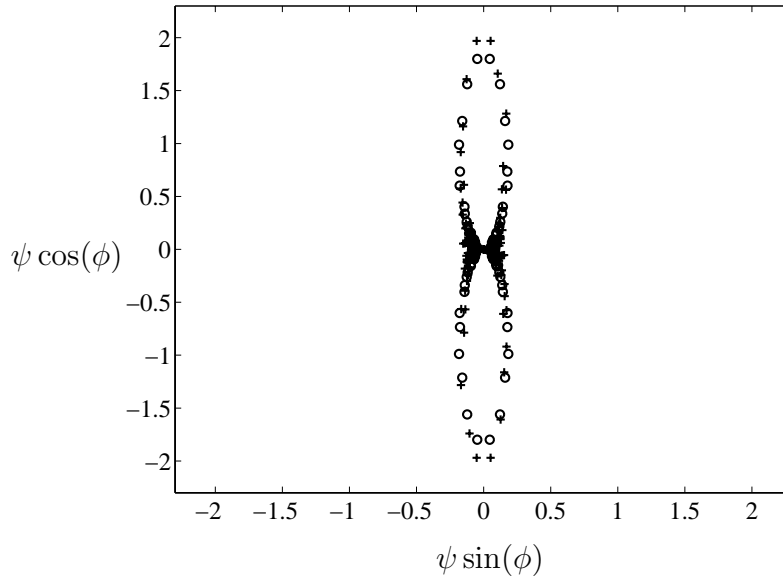
Figure 34: Measured (o) and computed (+) distribution functions at contraction ratio 5.6 and Re $= 85 \times 10^3$ and $l_r = 60$.
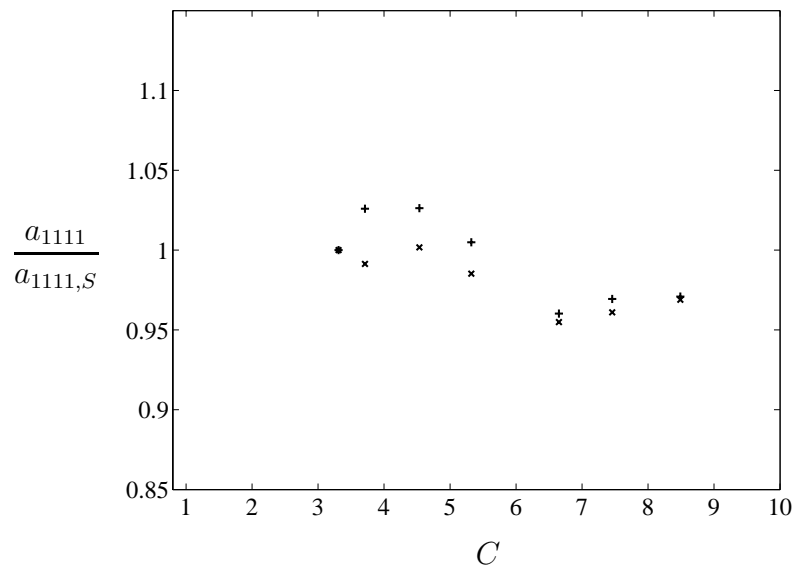
Figure 35: Development of the ratio of experimentally obtained values of a_{1111} prediction by Stokes flow, where measured ψ at $C = 3.6$ is used as the initial profile for cases Re $= 85 \times 10^3$ and $l_r = 20$ (+), Re $= 170 \times 10^3$ and $l_r = 20$ (x).
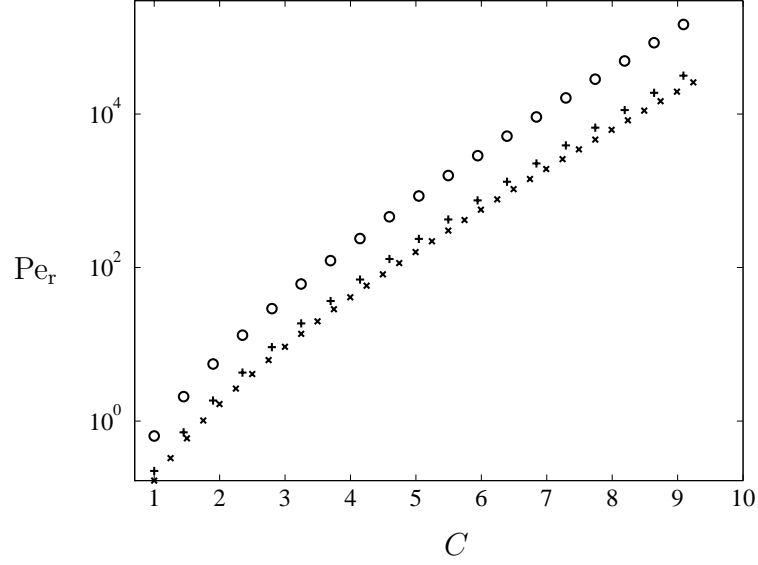
Figure 36: Development of Pe_r in the contraction for cases $\text{Re} = 85 \times 10^3$ and $l_r = 60$ (o); $\text{Re} = 85 \times 10^3$ and $l_r = 20$ (+); and $\text{Re} = 170 \times 10^3$ and $l_r = 20$ (x).

turbulent becomes insignificant further upstream (i.e., lower contraction ratio) due to the relatively lower turbulent intensity at the inlet.

For the cases investigated, relative importance of turbulence disappears when the streamwise turbulent intensity falls below 1.5%. The rotational Péclet number, Pe_r, compares the relative influence of the mean gradient component and the rotational diffusion (Krushkal & Gallily). This parameter is defined as,

$$\text{Pe}_\text{r} = \frac{\partial U_1 / \partial x_1}{D_r}. \tag{90}$$

where $\partial U_1 / \partial x_1$ is the characteristic velocity gradient.

Figure 36 shows the development of Pe_r along the contraction centerline for the measured cases. The values of D_r computed from equations 32 and 85 are used to evaluate Pe_r. The results show that the effect of turbulence on the orientation

109
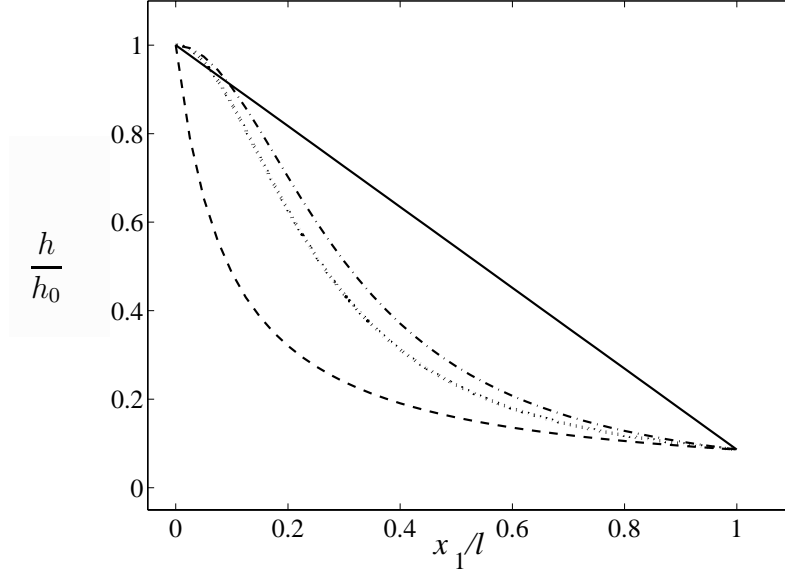
Figure 37: Contraction geometries considered; flat plate, equation 91 (—), constant rate of strain, equation 92 ($---$), linear rate of strain, equation 93 (- · -), quadratic rate of strain, equation 94 ($\cdots$).

.

development becomes insignificant when $Pe_r > 10$ (see figures 32, 35 and 36).

5.5 Effect of contraction shape

In the following paragraphs we examine the effect of contraction shape on orientation anisotropy. The inlet height, h_0, the contraction length, l, and the maximum contraction ratio, $C_{\max}$, are constant for the contractions considered. It has been shown that the production of turbulence has a negligible effect on orientation anisotropy. Therefore, the turbulent rotational diffusion coefficient is assumed to be dependent only on the inlet conditions. The value of D_r is evaluated, according to equation 85, based on the inlet turbulent conditions for case $l_r = 20$. As a result, the value of D_r and ϵ are independent of contraction shape for a given C. In this analysis, the resulting orientation anisotropy inside the contraction with flat walls, constant

rate of strain, linear rate of strain, and quadratic rate of strain are compared. The equation of local height for these contractions is given by

$$h = h_0 - 2x_1 \tan \beta, \tag{91}$$

$$h = \frac{h_0 l}{(C_{\max} - 1)x_1 + l}, \tag{92}$$

$$h = \frac{h_0 l^2}{(C_{\max} - 1)x_1^2 + l^2}, \tag{93}$$

$$h = \frac{2h_0 l^3}{3(C_{\max} - 1)l x_1^2 - (C_{\max} - 1)x_1^3 + 2l^3}, \tag{94}$$

respectively. Figure 37 shows the geometry of these contractions. Equation 84 is solved for flow at the contraction centerline using a finite difference approximation with isotropic inlet fiber orientation. The orientation parameter, a_{1111}, versus the contraction length and the contraction ratio is shown in Figs. 38 and 39, respectively. The contraction with flat walls has the smallest orientation anisotropy at the outlet. However, the contraction with constant rate of strain has the largest anisotropy. This is likely the result of different flow dynamics at the region immediately downstream of the inlet. To show the actual comparison of the orientation anisotropy in these cases, the orientation distribution function of contraction with constant rate of strain and flat walls at $C = 11.2$ are presented in figure 40. At $C > 3$ the randomizing
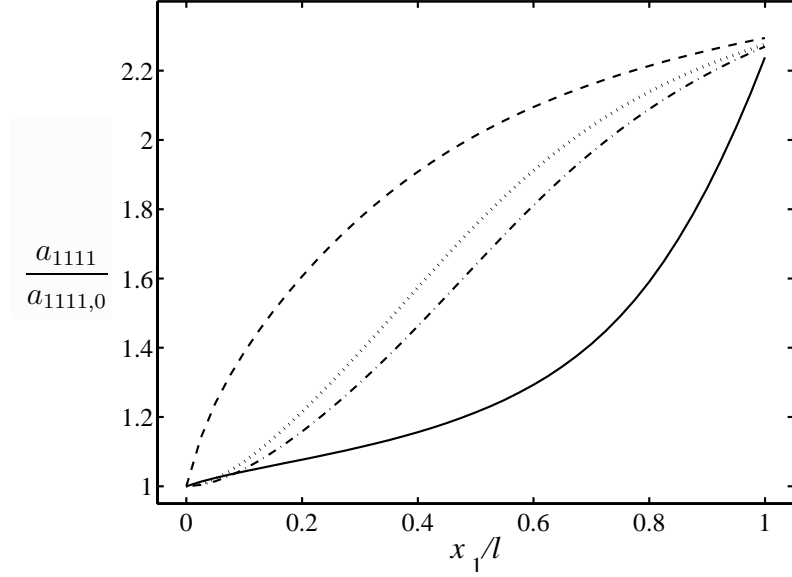
Figure 38: The orientation parameter a_{1111} for flat plate, equation 91, (—), constant rate of strain, equation 92, (− − −), linear rate of strain, equation 93, (- · -), quadratic rate of strain, equation 94, (· · ·).
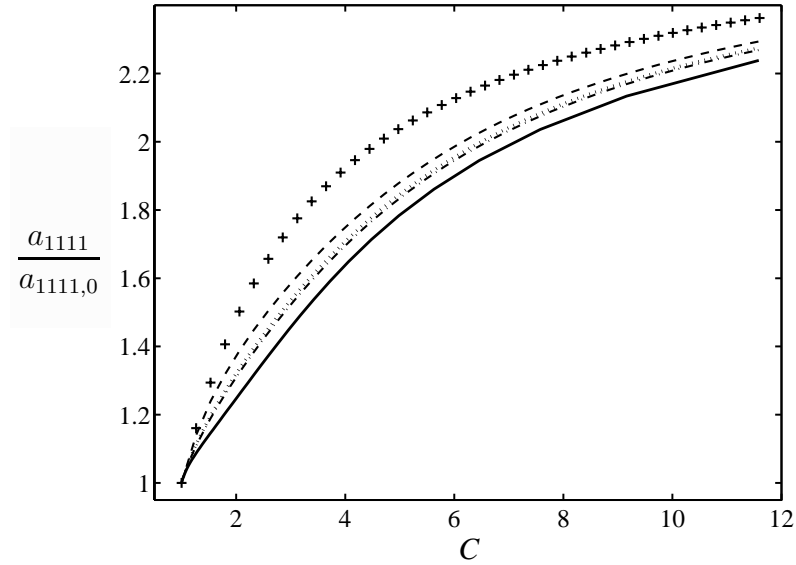
Figure 39: The orientation parameter a_{1111} versus C for flat plate, (—), constant rate of strain (− − −), linear rate of strain (- · -), and quadratic rate of strain (· · ·). Development of a_{1111} in Stokes flow, $D_r = 0$, for all cases (+).
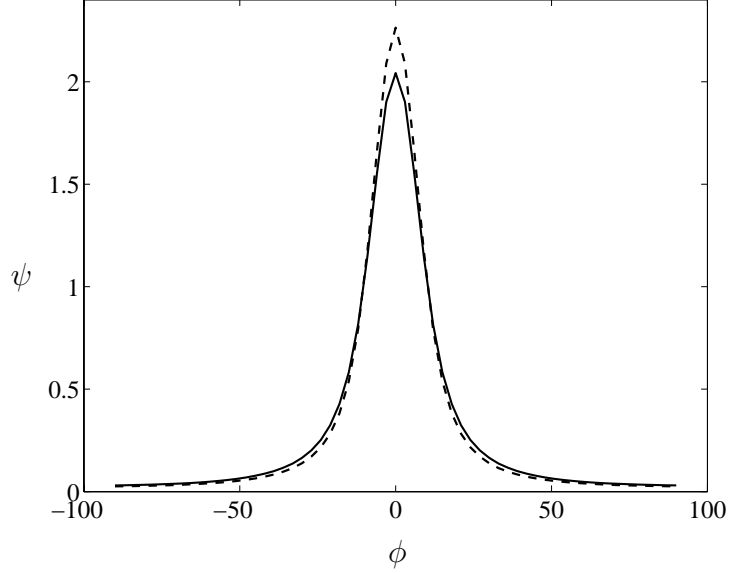
Figure 40: The orientation distribution function at $C = 11.2$ for flat plate (—), constant rate of strain $(- - -)$.

effect of turbulence is negligible compared to the orienting effect of flow acceleration. Therefore, in this region a_{1111} develops similarly for the contractions considered, as seen in figure 39. Thus, the orientation anisotropy follows the development of Stokes flow. At $C < 3$, where D_r is large, strong turbulence has more time to interact with fibers for contractions with low initial rate of strain. This rotational Péclet number, $\mathrm{Pe_r}$ more effectively describes the shape effect. The downstream variation of $\mathrm{Pe_r}$ for the studied contractions is presented in figure 41. Turbulence has negligible effect on orientation anisotropy when $\mathrm{Pe_r} > 10$. Smaller value of $\mathrm{Pe_r}$ at $C < 3$ results in a smaller orientation anisotropy at the outlet.

It should be noted that in Stokes flow, where $D_r = 0$, the development of a_{1111} is only a function of C and is independent of contraction shape. This is attributed to the fact that the change of orientation angle in Stokes flow is only dependent on the dimensionless acceleration, ϵ. The value of ϵ is identical in all contractions for a

113
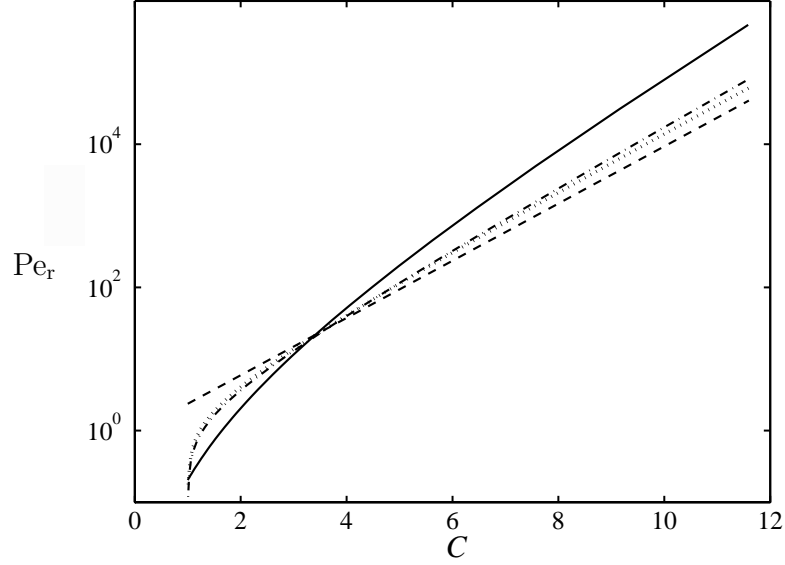
Figure 41: The rotational Péclet number for flat plate (—), constant rate of strain
($---$), linear rate of strain (- $\cdot$ -), quadratic rate of strain ($\cdots$).

given contraction ratio.

5.6 Accuracy of closure approximations in planar extensional flow

In this section, components of the a_{ijkl} tensor obtained by measuring the pla-
nar orientation state at the contraction centerline are presented. In addition, the
measured a_{ij} tensor is used to calculate a_{ijkl} based on the closure approximations
presented in the theory section.

The orientation of large aspect ratio fibers, $\lambda \approx 1$, for flow through planar con-
tractions, after simplifications and considering $\partial U_2 / \partial x_1 \approx 0$ is given by equations
32 and 33. The values of U_1 and $\partial U_1 / \partial x_1$ are computed at the center of each fiber
and are assumed to be constant along the fiber. Solution of equation 32 is given by
equation 34. Figures 42 and 43 show that both the fitted orthotropic and natural
closure approximations give accurate prediction of the measured normal components

114
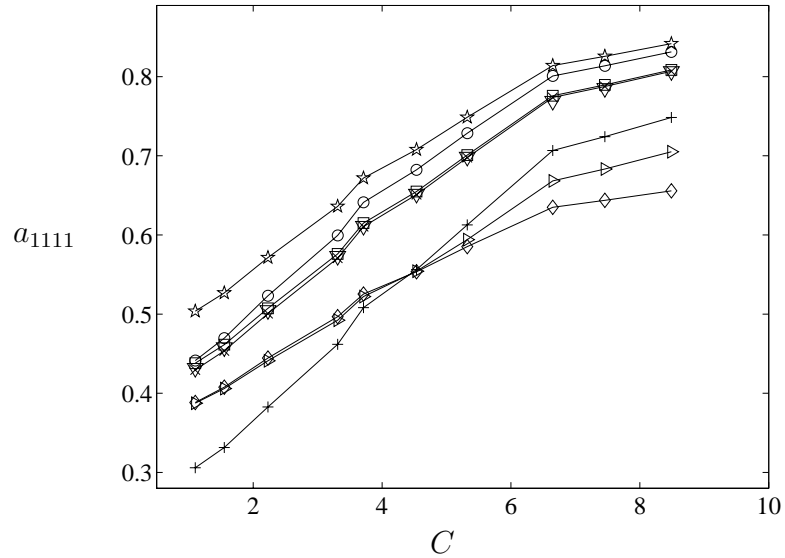
Figure 42: Measured a_{1111} for case $l_r = 20$ ($\triangle$) compared to predictions based on linear ($\diamond$), quadratic ($+$), hybrid ($\triangleright$), composite ($\star$), orthotropic interpolation (o), orthotropic fitted ($\square$), and natural (x) closure approximations.
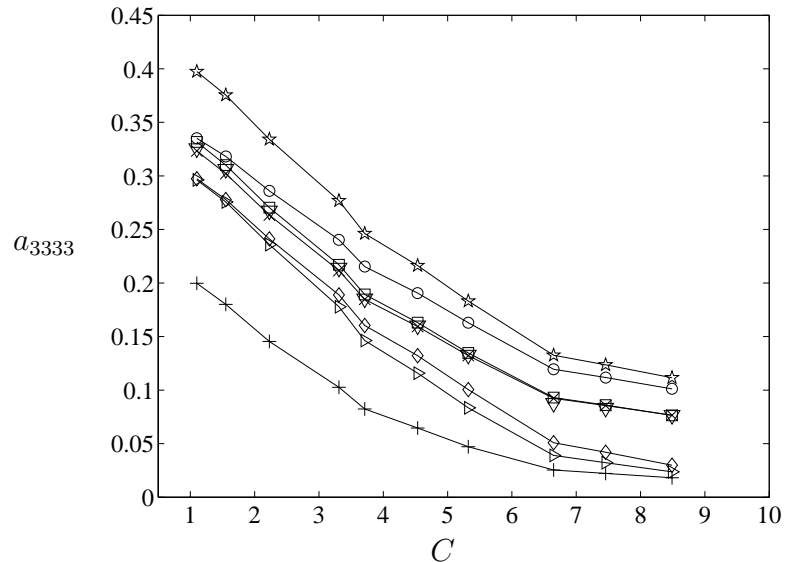
Figure 43: Measured a_{3333} for case $l_r = 20$ ($\triangle$) compared to predictions based on linear ($\diamond$), quadratic ($+$), hybrid ($\triangleright$), composite ($\star$), orthotropic interpolation (o), orthotropic fitted ($\square$), and natural (x) closure approximations.

of the orientation tensor, a_{1111} and a_{3333} for case $l_r = 20$. One of the most inaccurate predictions is given by the hybrid closure approximation. Interestingly, the hybrid closure approximation is one of the most widely used approximations to simulate the flow induced development of suspension microstructure. The same behavior has been observed when approximated a_{1111} and a_{3333} of case $l_r = 60$ were investigated. However, a least-squares fit of orthotropic model to the measured cases gave slightly different coefficients given by

$$
\begin{pmatrix} a_{1111} \\ \\ a_{3333} \end{pmatrix} = \begin{pmatrix} 0.101 + 0.413a_{11} + 0.498a_{11}^2 - 0.392a_{33} + 0.321a_{33}^2 + 0.305a_{11}a_{33} \\ \\ 0.141 - 0.395a_{11} + 0.2518a_{11}^2 + 0.084a_{33} + 0.786a_{33}^2 + 0.567a_{11}a_{33} \end{pmatrix}
$$

(95)

It should be noted that since θ is not measured only two normal components of a_{ijkl} have been investigated. The deviation between the predicted and measured orientation is represented by the error parameter, e_{ijkl}, defined as

$$
e_{ijkl} = \frac{(a_{ijkl} - \hat{a}_{ijkl})^2}{a_{ijkl}^2}
$$

(96)

where the repeated index do not imply summation. Figures 44 and 45 show the relative performance of orthotropic closure fitted to the measurements versus the fitted closure of Cintra and Tucker (1995). Predictions based on equation 95 give slightly more accurate orientation predictions in planar extensional flows. Cintra and Tucker's closure is based on a best fit of both extensional and shear flows. Therefore, coefficients given by equation 95 yield slightly more accurate prediction for plain strain
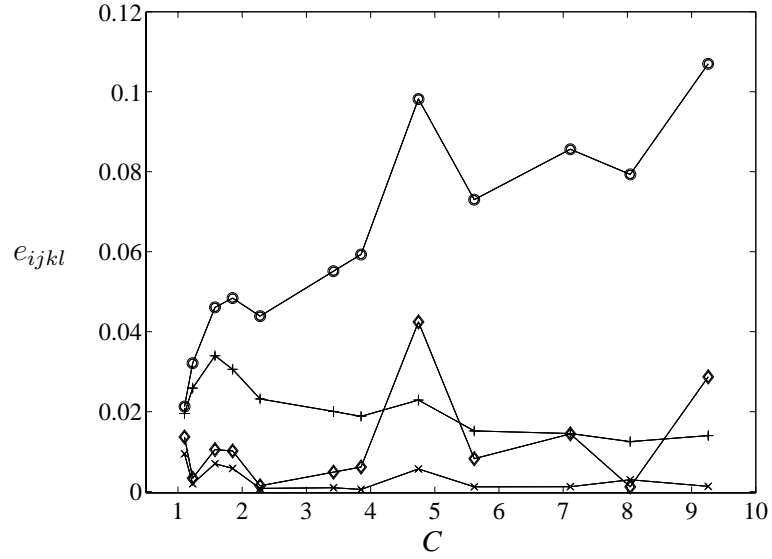
Figure 44: Normalized error in case $l_r = 60$; ($\times$) e_{1111} by present model, ($\diamond$) e_{3333} by present model, ($+$) e_{1111} by Cintra and Tucker (1995), ($\circ$) e_{3333} by Cintra and Tucker (1995).

flow. Even in orientation anisotropy predicted by Stokes flow, the coefficients presented here shows a better accuracy as illustrated in figure 46. In order to obtain ODF of Stokes flow prediction, equation 34 is used to calculate ϕ at different downstream positions.
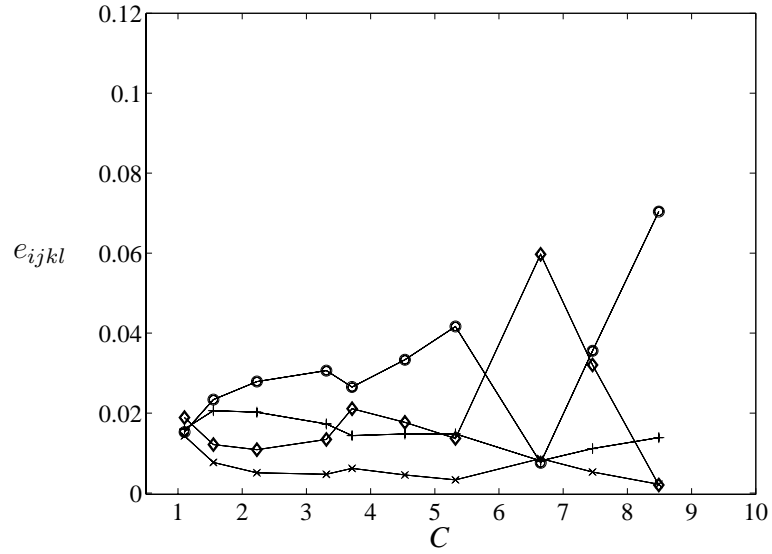
Figure 45: Normalized error in case $l_r = 20$; ($\times$) e_{1111} by present model, ($\diamond$) e_{3333} by present model, ($+$) e_{1111} by Cintra and Tucker (1995), ($\circ$) e_{3333} by Cintra and Tucker (1995).
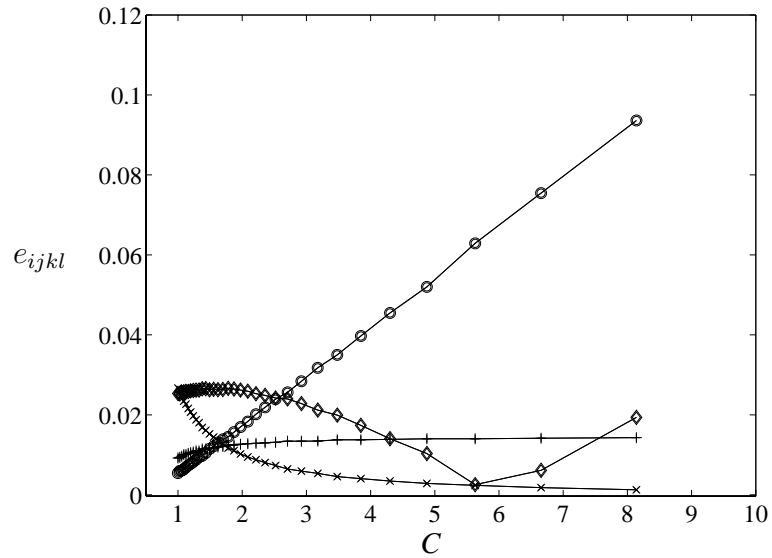
Figure 46: Normalized error for Stokes flow model; ($\times$) e_{1111} by present model, ($\diamond$) e_{3333} by present model, ($+$) e_{1111} by Cintra and Tucker (1995), ($\circ$) e_{3333} by Cintra and Tucker (1995).

118
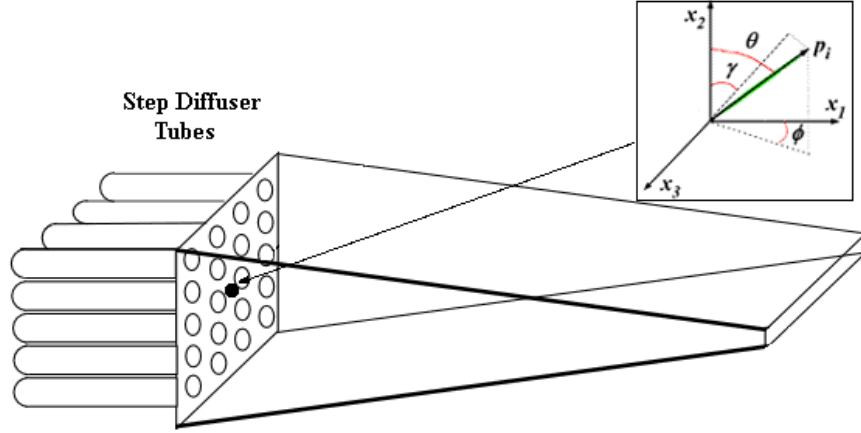
Figure 47: Schematic of the step diffuser generated turbulence experimental set-up with coordinate system.

5.7 Comparison of grid generated turbulence to step-diffuser turbulence

Previously, we have considered the influence of turbulence on the rotational diffusion of fibers for an idealized version of systems used in paper manufacture. Grid generated turbulence is characterized by nearly isotropic turbulence and uniform streamwise velocity gradients in the x_2- and x_3- directions (see figure 47). However, a typical flow geometry encountered in modern paper forming operations consists of a series of step-diffuser tubes which generate high intensity anisotropic turbulence and non-uniform streamwise velocity gradients in the x_2- and x_3- directions. Therefore, it is of practical interest to investigate turbulent flow characteristics representative of condition found in industry.

In the following paragraphs, the development of nearly homogenous isotropic turbulence at the inlet is compared to step diffuser generated turbulence. Inlet turbulence is generated by a five row, four single step tube bank.

Figure 48 shows the uniformity of the streamwise component of mean velocity for

119
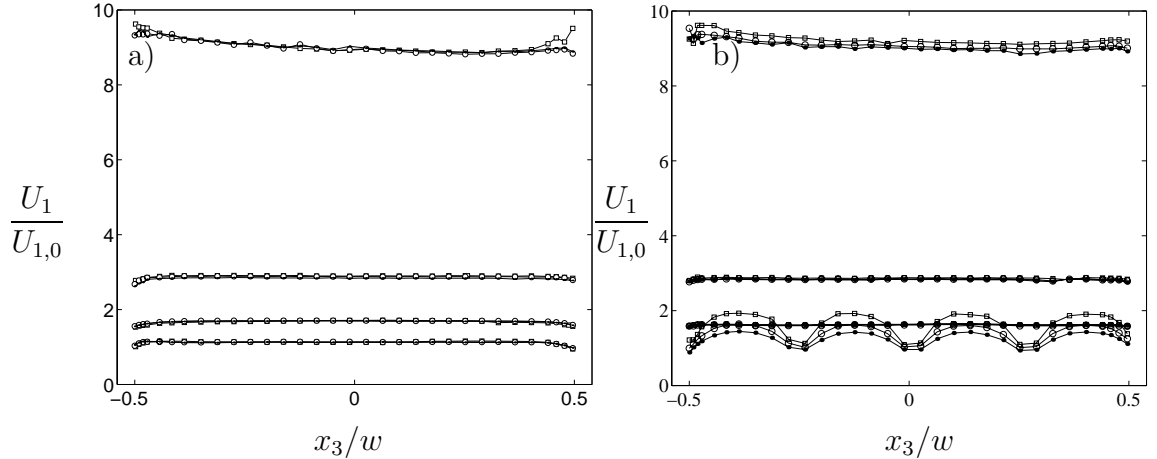
Figure 48: a) Mean streamwise velocity x_3-profile for grid generated turbulence at C=1.18, 1.65, 2.8, and 9.0 at Re $=85 \times 10^3$ (.), Re $= 127 \times 10^3$ (o), Re $= 150 \times 10^3$ ($\square$). b) Mean streamwise velocity x_3-profile for step diffuser generated turbulence at C=1.18, 1.65, 2.8, and 9.0 at Re $=85 \times 10^3$ (.), Re $= 127 \times 10^3$ (o), Re $= 150 \times 10^3$ ($\square$).

both grid generated and step diffuser generated turbulence for the Reynolds numbers considered in this study. The grid generated turbulence is uniform in the contraction except near the sidewalls near the outlet where the streamwise velocity profile reverts near the sidewalls. This is most likely due to the pressure drop at the contraction outlet. The step diffuser turbulence is characterized by strong jet interaction near the contraction inlet. However, in the region $C > 1.65$, the mean streamwise velocity profile becomes uniform. In this region the application of the model given by equations and is likely valid.

Turbulence characteristics inside the contraction vary between grid generated turbulence and step diffuser generated turbulence. Figures 49, 50 and 51 show the development of streamwise and lateral components of fluctuation velocity, respectively. The step diffuser generated turbulence shows a minimum in lateral fluctuation velocity components at $C = 2.4$ as opposed to $C = 2.0$ for the case of grid gener-

ated turbulence. Production of turbulent energy is nearly zero near the inlet of the contraction for grid generated turbulence due to nearly isotropic turbulence. Step diffuser generated turbulence is anisotropic therefore some production of turbulent energy is taking place near the contraction inlet. However, due to the presence of large scale eddies generated by the step diffuser tubes and the large turbulent intensity at the inlet, the decay of components of fluctuation velocity because of dissipation is dominant. Therefore, the dissipation of turbulent energy and production of turbulent energy become equal further downstream in the contraction. At $C > 2.8$, the turbulent energy increases for both cases because of anisotropy due to higher Reynolds stress component in the x_2- and x_3- directions than that in the x_1-direction. This effect becomes amplified further downstream at the high contraction ratio region. The increase in the streamwise component of the turbulent kinetic energy is most likely because of inter-component distribution of energy. The inlet region of the step diffuser turbulence is characterized by significant streamwise velocity gradients in x_2-direction. However, the rotational Péclet number is less than one at the inlet based on $\partial U_1 / \partial x_3$ and equation 85. Therefore, the model presented above for orientation diffusion due to turbulence in grid generated turbulence is likely accurate for dilute step diffuser generated turbulence assuming mean streamwise velocity gradient is known.
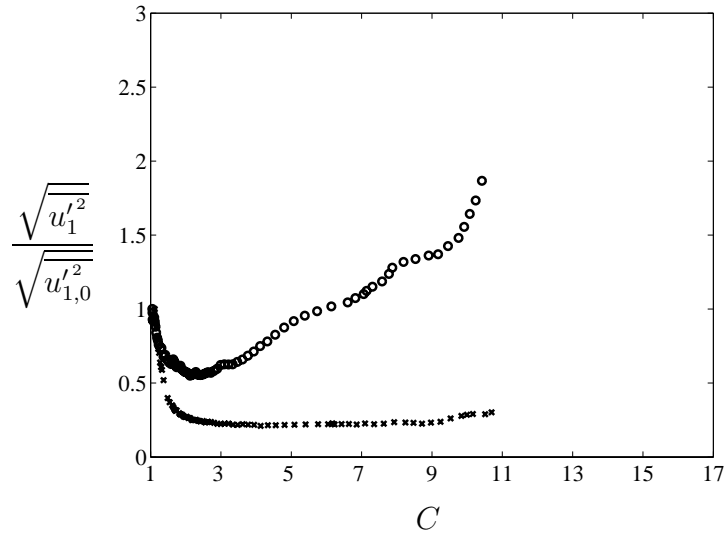
Figure 49: Development of normalized streamwise component of fluctuation velocity for grid generated turbulence $l_r = 20$ (o) and step diffuser generated turbulence (x) at $\text{Re} = 85 \times 10^3$.
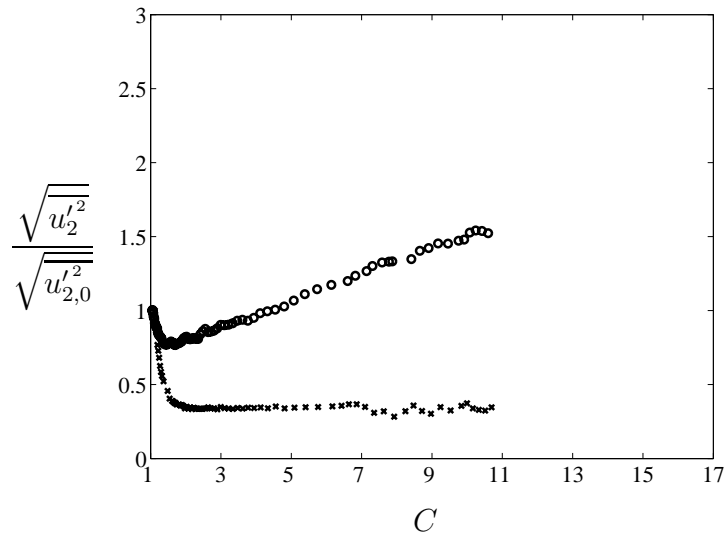
Figure 50: Development of normalized x_2- component of fluctuation velocity for grid generated turbulence $l_r = 20$ (o) and step diffuser generated turbulence (x) at $\text{Re} = 85 \times 10^3$.
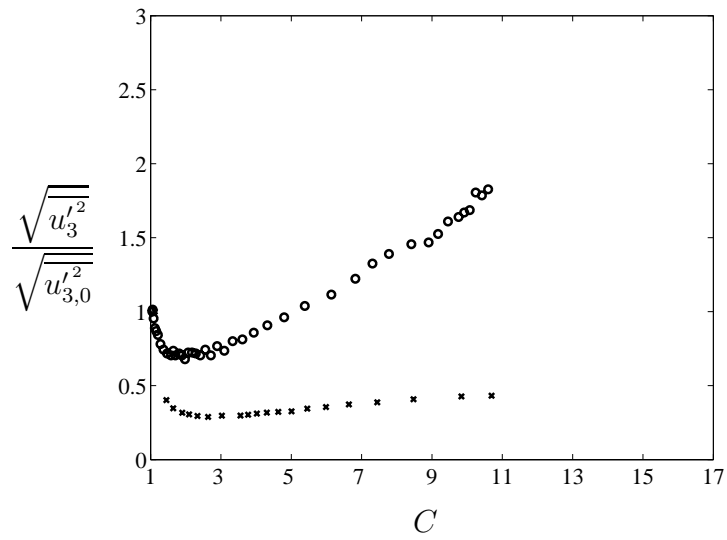
Figure 51: Development of normalized x_3- component of fluctuation velocity for grid generated turbulence $l_r = 20$ (o) and step diffuser generated turbulence (x) at Re $= 85 \times 10^3$.

CHAPTER 6

CONCLUSIONS

To date, a limited body of work is available considering the coupling of turbulence and rotational diffusion of fibers in practical suspension flow. In this work, the influence of turbulence on the development of the orientation distribution of a suspension of stiff fibers at high Reynolds number in a planar contraction is investigated. A dilute nearly density matched suspension is considered such that fiber-fiber interactions and the effect of fiber inertia are negligible.

Nearly isotropic homogenous turbulence with uniform mean velocity profile is introduced at the contraction inlet. It is observed that the development of the streamwise component of the fluctuation velocity up to contraction ratio 2 closely follows the development of decaying grid turbulence in a straight channel. The streamwise and lateral components of fluctuation velocity decrease to a minimum value downstream of the contraction inlet. The location of the minimum of velocity components depends on the position of the grid relative to the contraction inlet. The integral length scale of turbulence was found to be of the order of the fiber length at the contraction inlet, and increases with increasing contraction ratio.

The main results have shown that a Fokker-Planck type equation accurately models the orientation state of fibers in turbulent inhomogenous flow. The downstream development of orientation distribution shows that the rotational diffusion coefficient D_r decays exponentially with local contraction ratio, C, and is dependent on inlet turbulent characteristics. This suggests that the influence of turbulent energy production of fiber dynamics in the contraction is negligible. This is attributed to the small production of turbulent energy at $C < 2$, where turbulence closely follows the decay of grid generated turbulence in a rectangular channel, and the large streamwise rate of strain at large C which offsets the effect of turbulence. The development of orientation distributions function implies a rather weak dependence on Re for range of Re considered. Furthermore, the results show that the influence of turbulence on fiber rotation is negligible for $\text{Pe}_r > 10$.

The influence of turbulent parameters on rotational dispersion of fibers near the contraction inlet is predicted within an order of magnitude by the model put forth by Olson & Kerekes (1998). The model proposed by Krushkal & Gallily is shown to overpredict fiber rotational diffusion by two orders of magnitude. However, both models specify that the integral length scale Λ must be much larger than the fiber length scale, L, which is not valid for the suspension flow considered. The exponential decay of D_r disagrees with previously reported results (Olson *et al.* 2004), where D_r remains constant in the contraction according to their results. A model for D_r is proposed based on the observation that rotational diffusion is primarily dependent on inlet turbulent characteristics and local contraction ratio, and the components of

fluctuation velocity develop similarly for the range of Re, β, and l_r considered in this study. The model is limited to initially homogeneous, isotropic turbulent flow with uniform mean velocity profiles and negligible turbulent production near the inlet.

Based on this model, the fiber orientation in a contraction of arbitrary shape may be predicted by solving the Fokker-Planck equation for a given inlet turbulent condition. The orientation anisotropy parameter, a_{1111}, obtained from the moments of the orientation distribution function, is shown to vary with the contraction shape. Predictions show that the outlet anisotropy is maximum for contractions with high initial rate of strain. The development of orientation anisotropy is governed by the rotational Péclet number, Pe_r representing the interplay between the randomizing effect of turbulence and the orienting effect of streamwise mean rate of strain. The relative importance of turbulence disappears when the streamwise turbulent intensity falls below 1.5%. In the region $C > 4$, Pe_r indicates that turbulence has a negligible effect on fiber orientation and a_{1111} follows predictions based on Stokes flow. In the region $C < 3$, $\text{Pe}_r < 1$ indicating that turbulence strongly influences the orientation in this region.

Comparison of the measured a_{ijkl} at the centerline of a planar contraction to their approximations showed that natural and orthotropic approximations are the most accurate models. However, by fitting orthotropic model to measured a_{ijkl}, new coefficients have been obtained. It is shown that for planar contraction flow, orthotropic approximation with these coefficients better predicts the orientation state. It is interesting to investigate the performance of these coefficients in other flows.

The development of orientation distribution function follows that of high aspect ratio axisymmetric particles in Stokes flow when the rotational Péclet number is larger than 10.

There has been some disagreement among previous investigators as to the appropriate choice of length scale to evaluate the microscopic Reynolds number. Results show that the orientation distribution function at large C develops closely to the prediction based on Stokes flow. Based on this result and estimates of the fiber slip velocity, it is clear that fiber inertia played a negligible role in the experiments. Therefore, fiber diameter is the appropriate length scale to determine the microscopic Reynolds number and thus the effect of inertia.

The model for D_r in planar contraction flow is based on an idealized version of systems used in manufacturing. Semi-dilute suspension flows found in the paper industry are extremely complex due to the non-ideal nature of pulp fibers. These fibers are often irregularly shaped, flexible, with irregular, electrostatically charged surfaces. In addition, we have shown that the inlet flow to the converging zone of a typical hydraulic headbox is non-uniform. Turbulence is produced in the region $C < 2$ due to the presence of mean streamwise velocity gradients in the x_2 and x_3 directions. Therefore, prediction of flow induced microstructure in the converging zone is likely to have some error originating from the production of turbulent energy in the region $C < 2$. Accurate predictions of orientation state are expected in the region, $C > 2$, since the mean velocity gradients are nearly uniform.

APPENDIX A

EFFECT OF CONTRACTION HALF ANGLE

The effect of contraction half-angle, β, on the development of turbulent parameters inside a planar contraction is investigated. The values of β considered in this work ranged from $\beta = 8.16^o$ to $\beta = 8.63^o$. These values correspond to $C_{max} = 7.3$ and $C_{max} = 16.7$, respectively. Although the difference appears small, the total convective acceleration at the contraction outlet for the second case is more than double that of the first case. In this series of experiments, the flow Reynolds numbers are nearly constant and the same grid set-up was used. Figure A.1 shows the development of normalized streamwise rms-velocity component for the three different contraction angles considered. It appears that the contraction half-angle has no clear effect on development of streamwise rms-velocity component for the cases studied. This is in agreement with linear theory. However, Tsuge shows that the development of streamwise turbulent intensity in a planar contraction is a function of residence time. This is explained by the fact that the residence time for the low contraction case is only slightly more than the residence time for the high contraction case. The residence time effect should be more pronounced when changing Re Figure A.2 shows the

$$\frac{\sqrt{\overline{u_1'^2}}}{\sqrt{\overline{u_{1,0}'^2}}}$$
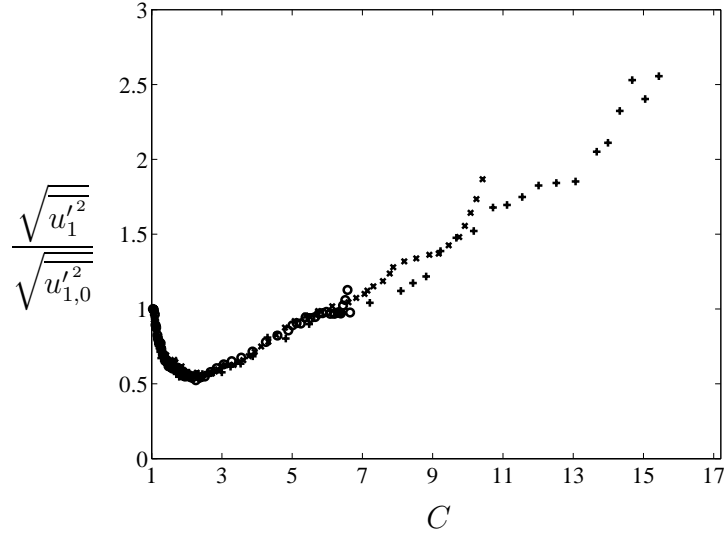
Figure A.1: Effect of contraction half-angle on the grid generated x_1-component of fluctuating velocity for $\beta = 8.16^o$ (o), $\beta = 8.63^o$ (x), $\beta = 8.89^o$ (+) for $l_r = 20$ and $\mathrm{Re} = 85 \times 10^3$.

development of normalized streamwise turbulent intensity for the three contraction angles considered. Again, it is seen that the three cases fall on the same curve signifying that the development dependens only upon the total applied strain. This is in agreement with the results reported by previous investigators.
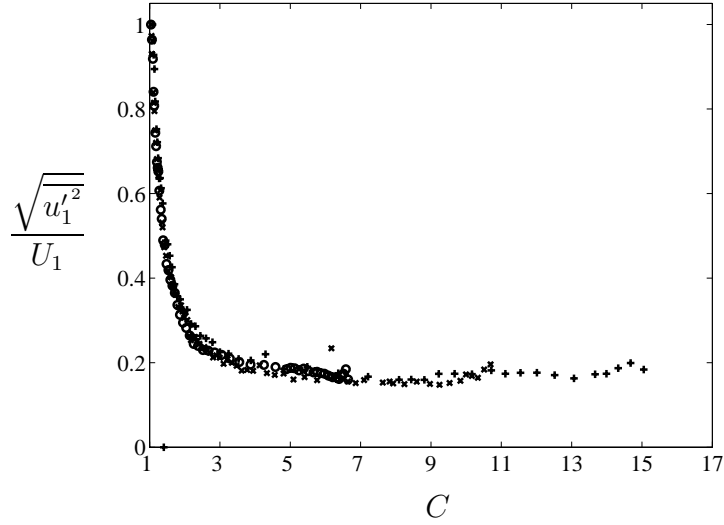
Figure A.2: Effect of contraction half-angle on the grid generated x_1-component of turbulent intensity for $\beta = 8.16^o$ (o), $\beta = 8.63^o$ (x), $\beta = 8.89^o$ (+) for $l_r = 20$ and Re $= 85 \times 10^3$.

Figure A.3 shows the development of normalized x_2-component of rms-velocity for the contraction angles considered. Figures A.4, 47, A.5, A.6, show the development of the x_2- and x_3- components of fluctuation velocity and turbulent intensity with changing contraction angle. Results are similar to the results mentioned earlier. The development of normalized x_2-component of turbulent intensity for the contraction angles considered. Figure A.5 shows the development of normalized x_3-component of fluctuation velocity for the contraction angles considered. Figure A.6 shows the development of normalized x_3- component of turbulent intensity for the contraction angles considered.
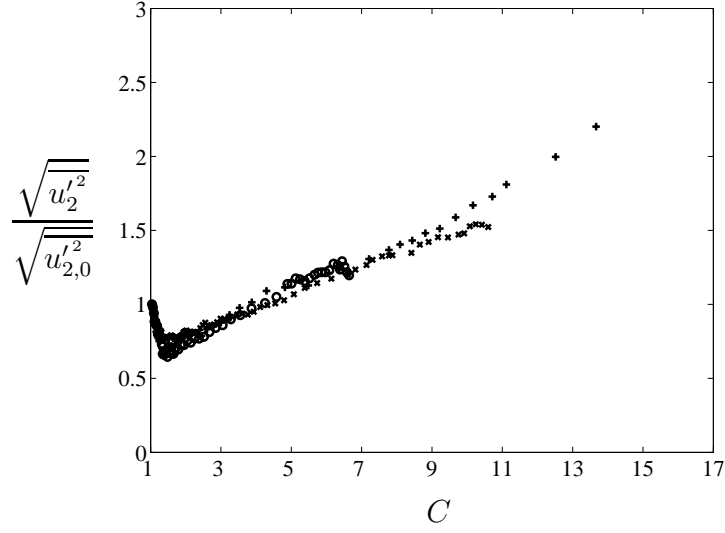
Figure A.3: Effect of contraction half-angle on x_2-component of rms-velocity for $\beta = 8.16^o$ (o), $\beta = 8.63^o$ (x), $\beta = 8.89^o$ (+) for $l_r = 20$ and Re $= 85 \times 10^3$.
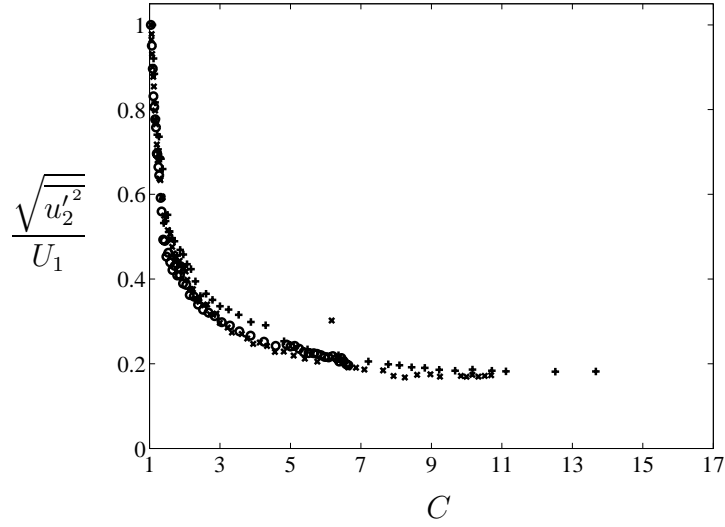
Figure A.4: Effect of contraction half-angle on x_2-component of intensity for $\beta = 8.16^o$ (o), $\beta = 8.63^o$ (x), $\beta = 8.89^o$ (+) for $l_r = 20$ and Re $= 85 \times 10^3$.
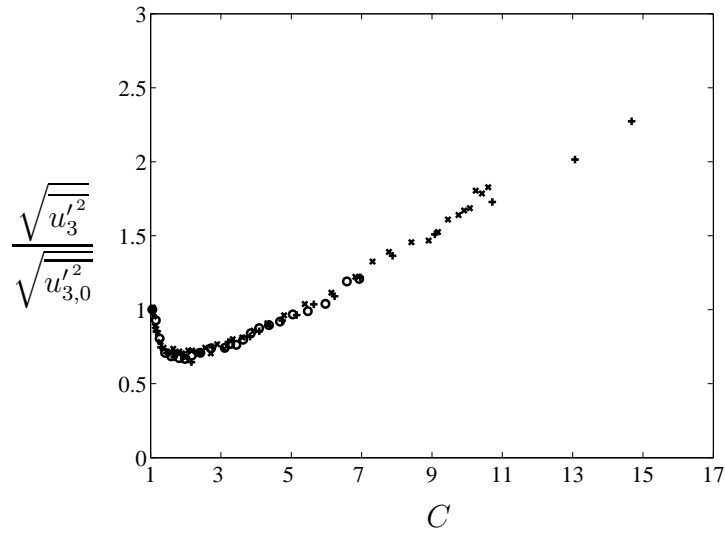
Figure A.5: Effect of contraction half-angle on x_3- component of fluctuation velocity for $\beta = 8.16^o$ (o), $\beta = 8.63^o$ (x), $\beta = 8.89^o$ (+).
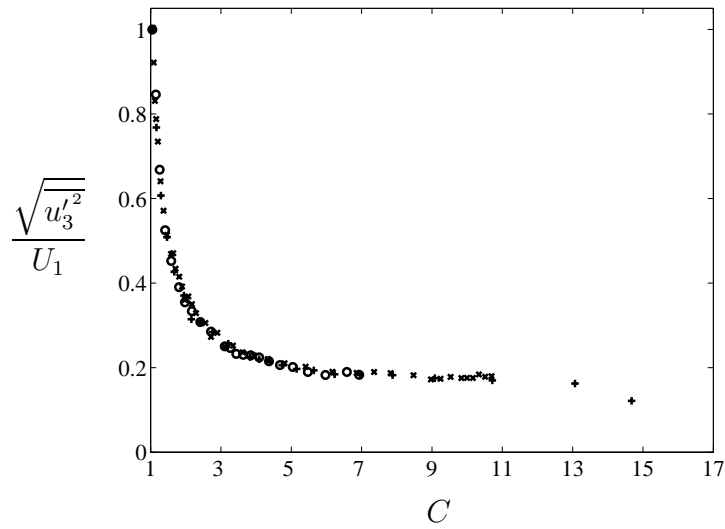
Figure A.6: Effect of contraction on x_3- component of turbulent intensity $\beta = 8.16^o$ (o), $\beta = 8.63^o$ (x), $\beta = 8.89^o$ (+) for $l_r = 20$ and Re $= 85 \times 10^3$.

APPENDIX B

ERRORS AND UNCERTAINTY

In the following paragraphs we consider the accuracy and reproducibility of fiber orientation state and the turbulent velocity field measurements presented above. Important sources of error originate from alignment of the ldv and high speed camera with the test section as well as precision error.

For each turbulent parameter the total uncertainty, $\delta_{T,i}$, is a function of the bias limit, B_i, and precision limit, P_i, given by

$$\delta_{T,i} = \sqrt{B_i^2 + P_{95\%,i}^2} \tag{B.1}$$

We assume that the source of uncertainty is independent and may be represented by a Gaussian distribution. Although there are many possible sources of error originating from fundamental ldv principles (*i.e.* fringe spacing and transmitting angle) and data acquisition procedures, we will focus on the likely most significant sources of error. Error propagation analaysis states that the total uncertainty in the measured U_1 and

Table B.1: Uncertainty in measured streamwise mean velocity component, U_1 for grid generated turbulence and $l_r = 20$ and $\mathrm{Re} = 85 \times 10^3$

C	$(\frac{\partial U_1}{\partial x_1} \delta x_{1,a})^2 \left(\frac{\mathrm{m}^2}{\mathrm{s}^2}\right)$	$(\frac{\partial U_1}{\partial x_1} \delta x_{1,b})^2 \left(\frac{\mathrm{m}^2}{\mathrm{s}^2}\right)$	$P^2_{95\%,U_1} \left(\frac{\mathrm{m}^2}{\mathrm{s}^2}\right)$	$\delta_{T,U_1} \left(\frac{\mathrm{m}}{\mathrm{s}}\right)$
2	3.2×10^{-4}	5.6×10^{-4}	2.05×10^{-5}	0.030
4	5.3×10^{-3}	0.009	8.41×10^{-5}	0.119
6	0.025	0.045	1.82×10^{-4}	0.266
8	0.282	0.141	3.2×10^{-4}	0.651

$\sqrt{\overline{u_1'^2}}$ is given by

$$\delta_{T,U_1} = \left[\left(\frac{\partial U_1}{\partial x_1} \delta x_{1,a} \right)^2 + \left(\frac{\partial U_1}{\partial x_1} \delta x_{1,b} \right)^2 + P^2_{95\%,U_1} \right]^{1/2}, \qquad (\mathrm{B.2})$$

and

$$\delta_{T,\sqrt{\overline{u_1'^2}}} = \left[\left(\frac{\partial \sqrt{\overline{u_1'^2}}}{\partial x_1} \delta x_{1,a} \right)^2 + \left(\frac{\partial \sqrt{\overline{u_1'^2}}}{\partial x_1} \delta x_{1,b} \right)^2 + P^2_{95\%,\sqrt{\overline{u_1'^2}}} \right]^{1/2}, \qquad (\mathrm{B.3})$$

where $\delta x_{1,a}$ is the uncertainty in x_1- position due initial alignment at the origin, $\delta x_{1,b}$ is the uncertainty in x_1- due to horizontal misalignment, while $P^2_{95\%,U_1}$ and $P^2_{95\%,\sqrt{\overline{u_1'^2}}}$ are the random errors associated with the measurements. Tables B.1 and B.2 summarize the estimated uncertainty in the measurements.

Results show that the majority of error in measurements of mean and turbulent

Table B.2: Uncertainty in measured streamwise fluctuation velocity component, $\sqrt{\overline{u_1'^2}}$ for grid generated turbulence and $l_r = 20$ and $\text{Re} = 85 \times 10^3$.

C	$(\frac{\partial\sqrt{\overline{u_1'^2}}}{\partial x_1}\delta x_{1,a})^2$ $\left(\frac{\text{m}^2}{\text{s}^2}\right)$	$(\frac{\partial\sqrt{\overline{u_1'^2}}}{\partial x_1}\delta x_{1,b})^2$ $\left(\frac{\text{m}^2}{\text{s}^2}\right)$	$P^2_{95\%,\sqrt{\overline{u_1'^2}}}$ $\left(\frac{\text{m}^2}{\text{s}^2}\right)$	$\delta_{T,\sqrt{\overline{u_1'^2}}}$ $\left(\frac{\text{m}}{\text{s}}\right)$
2	4.06×10^{-8}	7.22×10^{-8}	2.54×10^{-7}	6.05×10^{-4}
4	2.03×10^{-7}	3.61×10^{-7}	3.37×10^{-7}	9.50×10^{-4}
6	4.70×10^{-7}	8.36×10^{-7}	5.82×10^{-7}	1.40×10^{-3}
8	1.14×10^{-6}	2.02×10^{-6}	9.39×10^{-7}	2.00×10^{-3}

flow parameters is due to misalignment of the beam intersection in the x_1- direction, primarily at high C. Uncertainty in the streamwise location, $\delta x_{1,a}$, is introduced each time the ldv position is set to 0 relative to the contraction outlet. The contraction inlet may be referenced to accuracy approximately ± 0.3 mm. giving a conservative estimate of $\delta x_{1,a}$ to be 0.6 mm. If the beam fails to enter the contraction normal to the sidewall, then the ldv measurement of U_1 will be located at a different x_1 position than expected. The angle of misalignment was deduced from the differences in x_1 positions along the near and side walls. The uncertainty in the location of the probe volume due to horizontal misalignment, $\delta x_{1,b}$ is estimated to be 0.8 mm. The streamwise rate of strain, $\frac{\partial U_1}{\partial x_1}$ is evaluated based on equation 8. However, a polynomial fit of $urms(x_1)$ is required to estimate $\frac{\partial\sqrt{\overline{u_1'^2}}}{\partial x_1}$.

The precision of the mean and fluctuation velocity is evaluated by varying the

135

sample size, M_s, for a fixed number of events, k, at a single position. The precision error is given by

$$P_{95\%,i} = t_{e,k-1} \frac{\sigma_s}{k-1},$$ (B.4)

which represents the error associated with considering a finite number of instantaneous velocity measurements to calculate turbulent flow statistics. In this equation k is the event number consisting of M_s instantaneous velocity measurements, t_e is the t-statistic corresponding to the desired confidence interval and σ_s is the standard deviation of M_s samples. The standard error of the mean represents the 95% certainty that the mean will fall between the upper and lower limits of the error bars. The averaged results, $\bar{U}_1$, and $\sqrt{\overline{u_1'^2}}$ are given by

$$\bar{U}_1 = \frac{1}{k}\sum_1^k U_1, \quad \sqrt{\overline{u_1'^2}} = \frac{1}{k}\sum_1^k \sqrt{\overline{u_1'^2}}.$$ (B.5)

The precision error associated with the streamwise component of mean and fluctuation velocity is shown in figures B.1 and B.2, respectively. Based on this confidence interval, the uncertainty in U_1, and $\sqrt{\overline{u_1'^2}}$, are estimated to be $\pm$ 0.5 % and $\pm$ 3.5 %, respectively. Varying the sample size from 3,000 to 6,000 does no lead to significant differences in sampling error in U_1 or $\sqrt{\overline{u_1'^2}}$. Therefore, the choice of 4,500 samples per measurement location is justified.

The possible sources of error considered in measuring orientation anisotropy, a_{1111} are the bias error associated with imaging at a slight angle, β, to the x_1- and x_3- plane and precision error. Figure B.3 illustrates that the fiber image is a projection of
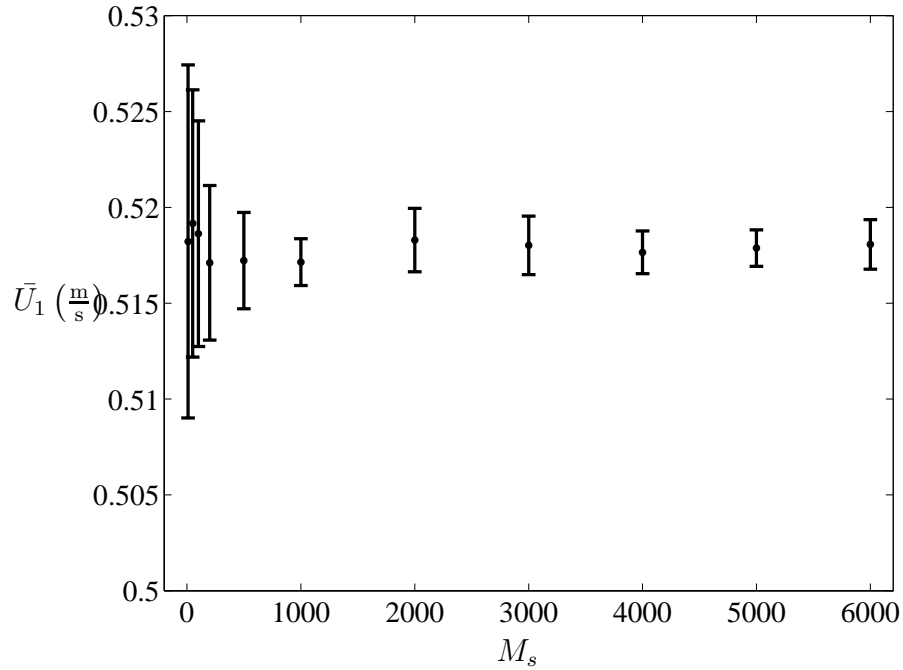
Figure B.1: Precision error at 95% confidence interval of mean streamwise velocity component as a function of sample number, M_s and total events, $k = 3$.
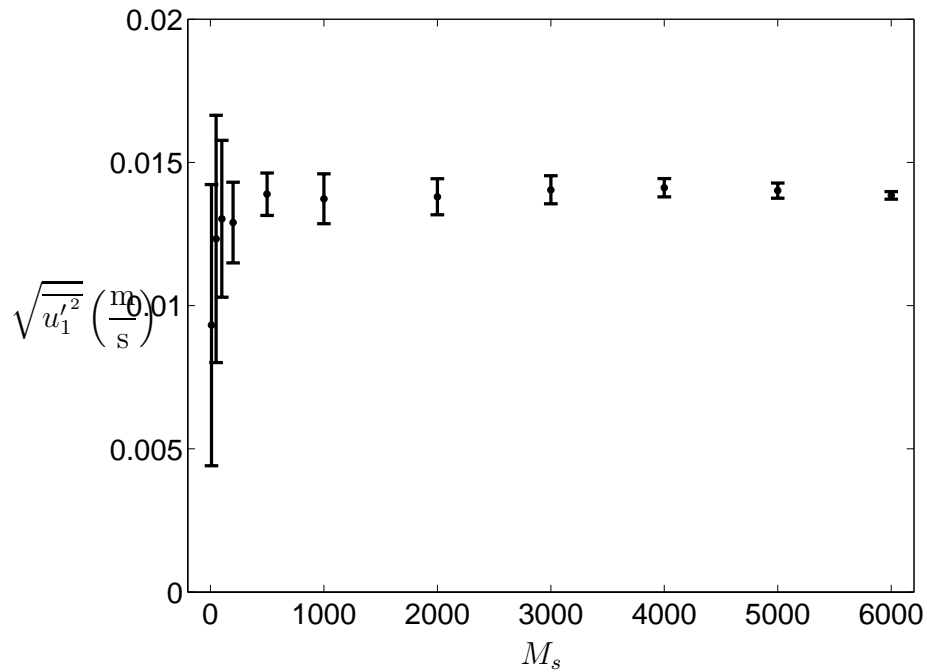
Figure B.2: Precision error at 95% confidence interval of streamwise component of fluctuation velocity as a function of M_s. ($k = 3$).
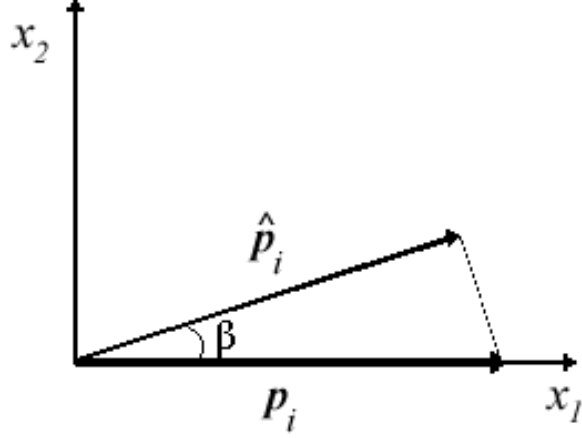
Figure B.3: Projection of fiber orientation vector, $\mathbf{p_i}$, onto plane parallel to top wall of planar contraction.

the x_1 component of the orientation vector, p_1 onto a plane parallel to the top wall $\hat{p}_1$.

The x_3- component of the orientation vector, p_3, remains unchanged leading a biased measured orientation angle, ϕ, which is always larger than the actual orientation angle. The magnitude of the deviation in p_1 is less than 1% for the contraction half angles, β, considered. However, the influence of this bias on measured a_{1111} needs to be quantified. This deviation is given by

$$\phi = \sin^{-1}(\sin\phi_m\cos\beta), \tag{B.6}$$

where ϕ_m is the measured orientation angle and ϕ is the exact orientation angle. Based on this relation, the bias error associated with the orientation measurements is approximately 1.6%. The total error in orientation anisotropy is given by

$$\delta_{T,a_{1111}} = \left[B^2_{a_{1111}} + P^2_{95\%,a_{1111}}\right]^{1/2}, \tag{B.7}$$

138
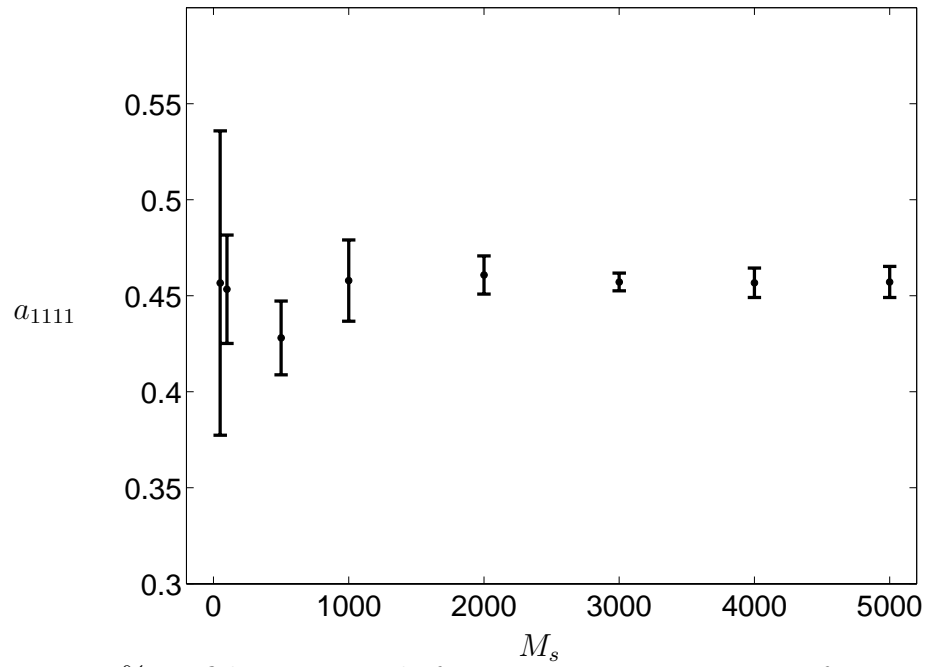
Figure B.4: 95% confidence interval of orientation anisotropy as a function of number of fibers sampled, M_s. $(k = 3)$

where the precision error, based on the results of figure B.4, is approximately $\pm 4.4\%$.

Table B.3 gives an overview of the bias and precision errors considered.

Table B.3: Uncertainty in measured orientation anisotropy parameter, a_{1111} for grid generated turbulence and $l_r = 20$ and $\mathrm{Re} = 85 \times 10^3$.

C	$B^2_{a_{1111}}$	$P^2_{95\%,a_{1111}}$	$\delta_{T,a_{1111}}$
2	7.21×10^{-5}	5.54×10^{-4}	0.025
4	1.30×10^{-4}	9.94×10^{-4}	0.036
6	1.60×10^{-4}	1.23×10^{-3}	0.037
8	1.85×10^{-4}	1.42×10^{-3}	0.040

APPENDIX C

ORIENTATION TENSOR COMPONENTS

Table C.1: Measured second and fourth order orientation tensor components for case $\text{Re} = 85 \times 10^3$ and $l_r = 20$.

C	a_{11}	a_{33}	a_{13}	a_{1111}	a_{3333}	a_{1133}
1.16	0.5531	0.4469	0	0.4318	0.3256	0.1213
1.55	0.5757	0.4243	0	0.4579	0.3064	0.1178
2.23	0.6186	0.3814	-0.0053	0.5048	0.2675	0.1139
3.31	0.6796	0.3204	-0.014	0.5733	0.2141	0.1063
3.71	0.7129	0.2871	0.0055	0.6113	0.1859	0.1016
4.53	0.7458	0..2542	-0.0143	0.6519	0.1602	0.0940
5.32	0.7829	0.2172	0.0099	0.6986	0.1329	0.0843
6.65	0.8407	0.1593	0	0.7692	0.0878	0.0715
7.46	0.8510	0.1490	0	0.7854	0.0833	0.0656
8.49	0.8651	0.1349	0	0.8067	0.0766	0.0584

Table C.2: Measured second and fourth order orientation tensor components for case $Re = 170 \times 10^3$ and $l_r = 20$.

C	a_{11}	a_{33}	a_{13}	a_{1111}	a_{3333}	a_{1133}
1.16	0.5622	0.4378	0	0.4436	– – –	– – –
1.55	0.5806	0.4194	0	0.4650	– – –	– – –
2.23	0.6058	0.3942	0	0.4917	– – –	– – –
3.31	0.6735	0.3265	0	0.5666	– – –	– – –
3.71	0.6888	0.3112	0	0.5828	– – –	– – –
4.53	0.7252	0.2748	0	0.6285	– – –	– – –
5.32	0.7665	0.2335	0	0.6770	– – –	– – –
6.65	0.8323	0.1675	0	0.7567	– – –	– – –
7.46	0.8430	0.1570	0	0.7739	– – –	– – –
8.49	0.8578	0.1413	0	0.7969	– – –	– – –

Table C.3: Measured second and fourth order orientation tensor components for case $Re = 85 \times 10^3$ and $l_r = 60$.

C	a_{11}	a_{33}	a_{13}	a_{1111}	a_{3333}	a_{1133}
1.16	0.5796	0.4204	0	0.4646	0.3054	0.1150
1.55	0.6223	0.3777	0	0.5144	0.2698	0.1079
2.23	0.6688	0.3312	0	0.5640	0.2265	0.1047
3.31	0.7494	0.2506	0	0.6599	0.1610	0.0895
3.71	0.7744	0.2256	0	0.6907	0.1419	0.0837
4.53	0.8091	0.1909	0	0.7387	0.1205	0.0704
5.32	0.8501	0.1499	0	0.7874	0.0873	0.0627
6.65	0.8798	0.1202	0	0.8274	0.0677	0.0524
7.46	0.8990	0.1010	0	0.8523	0.0544	0.0466
8.49	0.9052	0.0948	0	0.8623	0.0519	0.0429

APPENDIX D

INERTIA INDUCED FIBER DYNAMICS

A more precise approach to determine the influence of inertia is to calculate the fiber slip velocity from the equations of motion governing an isolated fiber suspended in an accelerating flow field. The fiber is considered to be a cylinder of uniform length, L, and diameter, d. The force balance in the x_1- direction for a cylinder with streamwise axis parallel to x_3- direction is given by,

$$U_f(x_1)\frac{\partial U_f(x_1)}{\partial x_1} = \frac{2\rho}{\pi \, d\rho_f}C_D(U_1(x_1) - U_f(x_1))^2, \qquad (D.1)$$

where C_D denotes the drag coefficient. The drag coefficient is a function of fiber Reynolds number based on the fiber slip velocity, fiber diameter, and the carrier fluid viscosity (Panton 1984). In this analysis, the free stream pressure gradient along the fiber diameter is assumed to be zero. Thus, the value of C_D for zero pressure gradient flow is used. The effect of turbulent eddies and interaction between fibers is not considered.

A finite difference approximation is used to solve equation D.1 for the fiber slip velocity, $(U_1 - U_f)$. Figure D.1 shows the effect of fiber diameter on its velocity along

143
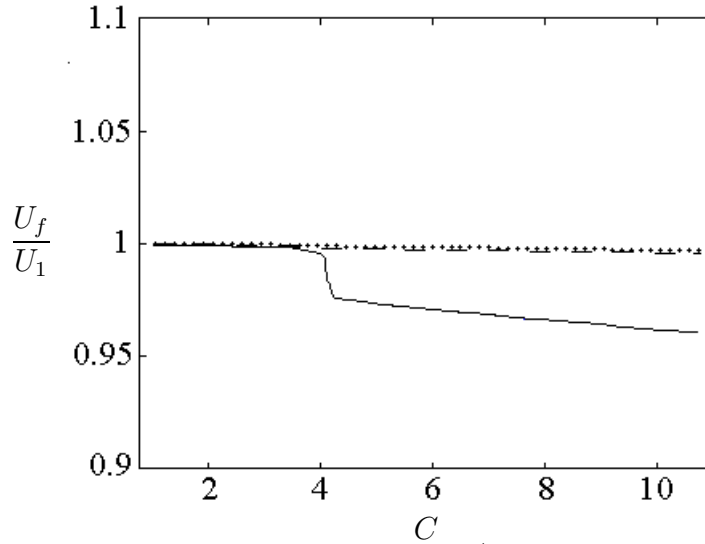
Figure D.1: The downstream development of U_f/U_1, d $= 0.57$ μm $(\cdots)$,5.7 μm (- -),
d $= 57$ μm (—), fiber aspect ratio, a_p, in these plots is constant $(a_p = 53)$.

the contraction. In these plots fiber aspect ratio is constant. This figure implies that

increasing fiber diameter leads to an increase in fiber slip velocity. The slip velocity is

largest at high contraction ratios where acceleration is high, however, for fibers used

in this study the slip velocity is almost negligible. The change in fiber length with

constant fiber diameter does not affect the slip velocity. The effect of change of fiber

density on slip velocity is shown in figure D.2. For heavier particles the slip velocity

is larger.

The drag force for a fiber in which the streamwise axis is aligned in x_1-direction

is much smaller compared to a fiber aligned in the x_3-direction.

However, considering fiber diameter as the length scale, Re$_f$ will be small enough

to imply no effect of fiber inertia. The force balance in the streamwise direction shows

that fiber velocity induced by the drag force is dependent on the fiber diameter, d , and

the liquid and fiber density ratio. Thus, the relative velocity of fiber and the carrier
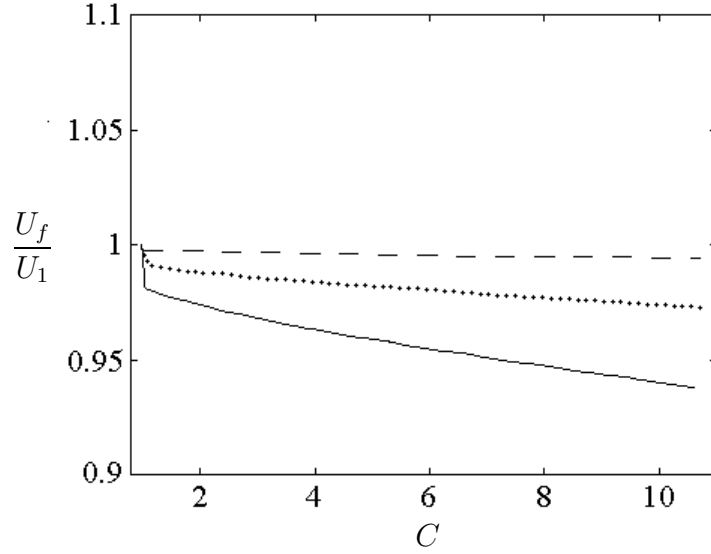
Figure D.2: The downstream development of U_f/U_1, $\rho_f/\rho = 1.16$ (- -), $\rho_f/\rho = 22.8$ ($\cdots$), $\rho_f/\rho = 114.0$ (—), aspect ratio, a_p, in these plots is constant ($a_p = 53$).

liquid is a function of fiber diameter only, since the ratio of fiber to liquid density is approximately equal to one. For the fiber dimensions and suspension properties used in this study, the slip velocity is very small. Assuming

Thus, it can be concluded that the effect of inertia is negligible if the Reynolds number based on the fiber diameter, and not length, is the appropriate parameter. This question will be addressed when the distribution of the measured orientation anisotropy is compared to the theories for inertialess fibers in suspension.

145

REFERENCES

Advani, S. & Tucker, C. 1987 The use of tensors to describe and predict fiber orientation in short fiber composites. *Journal of Rheology* **31**, 751.

Advani, S. & Tucker, C. 1990 Closure approximations for three-dimensional structure tensors. *Journal of Rheology* **34**, 367.

Advani, S. & Tucker, C. 1990 A numerical simulation of short fiber orientation in compression molding. *Polymer Composites* **11**, 164.

Aidun, C. & Lu, Y. 1995 Lattice Boltzmann simulation of solid particles suspended in fluid. *Journal of Statistical Physics* **81**, 49.

Aidun, C. Lu, Y. & Ding, E. 1998 Direct analysis of particulate suspensions with inertia using the discrete Boltzmann equation. *Journal of Fluid Mechanics* **373**, 287.

Akbar, S. & Altan, M. 1992 On the solution of fiber orientation in two-dimensional homogeneous flows. *Polymer Engineering and Science* **32**, 214.

Altan, M., Advani, S., Gueceri, S. & Pipes, R. 1989 On the description of the orientation state for fiber suspensions in homogenous flows. *Journal of Rheology* **33**, 1129.

Altan, M. & Rao, G. 1995 Constituve Equation for Concentrated Suspensions in Newtonian Liquids. *Journal of Rheology* **39**, 679.

Batchelor, G. 1970 Stress system in a suspension of force-free particles *Journal of Fluid Mechanics* **41**, 545.

Batchelor, G. 1971 The stress generated in a non-dilute suspension of elongated particles by pure straining motion. *Journal of Fluid Mechanics* **46**, 813.

Batchelor, G. & Proudman, I. 1954 The effect of rapid distortion of a fluid in turbulent motion. *Quarterly Journal of Mechanics and Applied Mathematics* **7**, 83.

Bay, R. & Tucker, C. 1992 Stereological measurement and error estimates for three-dimensional fiber orientation. *Polymer Engineering and Science* **32**, 240.

Becker, L. & Shelley, M. 2001 Instability of elastic filaments in shear flow yields first-normal-stress differences. *Physical Review Letters* **87**, 245.

Bernstein, O. & Shapiro, M. 1994 Direct determination of the orientation distribution function of cylindrical particles immersed in laminar and turbulent flow. *Journal of Aerosol Science* **25**, 113.

Brenner, H. 1964 The Stokes resistance of an arbitrary particle-II, An extension. *Chemical Engineering Science* **19**, 599.

Brenner, H. 1974 Rheology of a dilute suspension of axisymmetric Brownian particles. *International Journal of Multiphase Flow* **1**, 195.

Brenner, H. 1981 The translational and rotational motions of an n-dimensional hypersphere through a viscous fluid at small Reynolds numbers. *Journal of Fluid Mechanics* **111**, 197.

Bretherton, F. 1964 The motion of rigid particles in a shear flow at low Reynolds number. *Journal of Fluid Mechanics* **14**, 284.

Bunner, B. & Tryggvason, G. 1999 Direct numerical simulations of three-dimensional bubbly flows. *Physics of Fluids* **11**, 1967.

Chaffey, C., Takano, M. & Mason, S. 1965 Particle motions in sheared suspensions. XVI. Orientations of rods and disks in hyperbolic and other flows. *Canadian Journal of Physics* **43**, 1269.

Chiba, K. & Nakamura, K. 1998 Numerical solution of fiber suspension flow through a complex channel. *Journal of Non-Newtonian Fluid Mechanics* **78**, 167.

Chiba, K., Nakamura, K., & Boger, D. 1990 A numerical solution for the flow of dilute fiber suspensions through an axisymmetric contraction. *Journal of Non-Newtonian Fluid Mechanics* **35**, 1.

Cho, Y., Hartnett, J. & Kwack, E. 1980 Chemical effects in the flow of dilute polymer solutions. *Letters in Heat and Mass Transfer* **7**, 1.

Cintra, E. & Tucker, L. 1995 Orthotropic closure approximations for flow-induced fiber orientation. *Journal of Rheology* **39**, 1095.

Cox, R. 1970 The motion of long slender bodies in a viscous fluid. Part 1. general theory. *Journal of Fluid Mechanics* **44**, 791.

Cox, R. & Brenner, H. 1971 The rheology of a suspension of particles in a Newtonian fluid. *Chemical Engineering Science* **26**, 65.

Crowe C. 1982 Review - numerical models for dilute gas-particle flows. *Journal of Fluids Engineering, Transactions of the ASME* **104**, 297.

Crowe C., Chung J. & Troutt T. 1993 Particle dispersion by organized turbulent structures. Particulate Two-Phase Flow, ed. Chap. 18, 626.

Dinh, S. & Armstrong, R. 1984 A rheological equation of state for semiconcentrated fiber suspensions. *Journal of Rheology* **28**, 207.

Doi, M. & Edwards, S. 1978 Dynamics of rod-like macromolecules in concentrated solution. I. *Journal of Chemical Society of Faraday Transactions II.* **74**, 560.

Doi, M. 1981 Molecular dynamics and rheological properties of concentrated solutions of rodlike polymers in isotropic and liquid crystalline phases. *Journal of Polymer Science, Polymer Physics Edition* **19**, 229.

Doi, M. & Edwards, S. 1988 *Theory of Polymer Dynamics*, Oxford University Press.

Derbunovich, G., Zemskaya, A., Repik, E., & Sosedko, Y. 1987 Effect of flow contraction on the level of turbulence. *Izvestiya akademii Nauk SSSR* **2**, 289.

Durst, F., Melling, A. & Whitelaw, J. 1981 *Principles and Practice of Laser-Doppler Anemometry.* Academic Press, New York.

Elghobashi S. & Truesdell G. 1992 Direct simulation of particle dispersion in decaying isotropic turbulence. *Journal of Fluid Mechanics* **242**, 655.

Elghobashi S. & Truesdell G. 1993 On the two-way interaction between homogeneous turbulence and dispersed solid particles I: turbulence modification. *Physics of Fluids A* **5**, 1790.

Feng, J. & Leal, L. 1997 Simulating complex flows of liquid-crystalline polymers using the Doi theory. *Journal of Rheology* **41**, 1317.

Folgar, F. & Tucker, C. 1984 Orientation Behavior of Fibers in Concentrated Suspensions. *Journal of Reinforced Plastic Composites* **3**,98.

Giesekus, H. 1982 Simple constitutive equation for polymer fluids based on the concept of deformation-dependent tensorial mobility. *Journal of Non-Newtonian Fluid Mechanics* **11**, 69.

Givler, R. 1981 Numerically Predicted Fiber Orientation in Dilute Suspension Flow. Ph.D. thesis, University of Delaware.

Goldsmith, H. & Mason, S. 1967 The Microrheology of Dispersions, in F.R. Eirich, ed., *Rheology: Theory and Applications, Vol. IV*, Academic.

Goldstein, M. & Durbin, P. 1980 The effect of finite turbulence spatial scale on the amplification of turbulence by a contracting stream. *Journal of Fluid Mechanics* **98**, 473.

Goldstein, R. 1996 Fluid Mechanics Measurements, Taylor and Francis, London, U.K.

Gore R. & Crowe C. 1989 Effect of particle size on modulating turbulence intensity. *International Journal of Multiphase Flow* **15**, 279.

Gore, R. & Crowe, C. 1991 Modulation of turbulence by a dispersed phase. *Journal of Fluids Engineering, Transactions of the ASME* **113**, 304.

Groth, J. & Johansson, A. 1988 Turbulence reductions by screen. *Journal of Fluid Mechanics* **197**, 139.

Gupta, M. & Wang, K. 1993 Fiber orientation and mechanical properties of short-fiber-reinforced injection-molded composites: simulated and experimental results. *Polymer Composites* **14**, 367.

Hand, G. 1962 Theory of anisotropic fluids. *Journal of Fluid Mechanics* **13**, 33.

Harris, J. & Pittman, J. 1976 Alignment of slender rod-like particles in suspension using converging flow. *Transactions of Institution of Chemical Engineers* **54**, 73.

Hinch, E. & Leal, L. 1975 Constitutive equations in suspension mechanics. I. General formulation. *Journal of Fluid Mechanics* **71**, 481.

Hinch, E. & Leal, L. 1976 Constitutive equations in suspension mechanics. II. Approximate forms for a suspension of rigid particles affected by Brownian rotations. *Journal of Fluid Mechanics* **76**, 187.

Hetsroni G. 1989 Particles-turbulence interaction. *International Journal of Multiphase Flow* **15**, 735.

Huang, P., Hu, H. & Joseph, D. 1998 Direct simulation of the sedimentation of elliptic particles in Oldroyd-B fluids. *Journal of Fluid Mechanics* **362**, 297.

Hunt, J. & Carruthers, D. 1990 Rapid distortion theory and the problems of tur-

bulence. *Journal of Fluid Mechanics* **212**, 497.

Hussain, A. & Ramjee, V. 1976 Effects of the axisymmetric contraction shape on incompressible turbulent flow. *Journal of Fluids Engineering* **98**, 897.

Jeffery, G. 1922 The motion of ellipsoidal particles immersed in viscous fluid. *Proceedings of the Royal Society London A.* **102**, 161.

Kacir, L., Narkis, M. & Ishai, O. 1975 Orientation of short glass-giber composites, I preparation and statistical analysis of aligned fiber mats. *Polymer Engineering Science* **15**, 525.

Koch, D. & Rahnama, M. 1995 The effect of hydrodynamic interactions on the orientation distribution in a fiber suspension subject to simple shear flow. *Physics of Fluids* **7**, 487.

Krushkal, E. & Gallily, I. 1988 On the orientation distribution function of non-spherical aerosol particles in a general shear flow. *Journal of Aerosol Science* **19**, 197.

Kwak, D., Reynolds, W. & Ferziger, J. 1975 Three dimensional time dependent computation of turbulent ows.Stanford University Report TF-5, Department of Mechanical Engineering, Stanford University, Stanford, CA.

Ladd, A., Colvin, M. & Frenkel, D. 1988 Application of Lattice-gas cellular automata to the brownian motion of solids in suspension. *Physics Review of Letters* **60** 975.

Ladd, A. 1994 Numerical Simulations of Particulate Suspensions via a Discretized Boltzmann Equation. Part 2. Numerical Results. *Journal of Fluid Mechanics* **271**, 311.

Lee, M.& Reynolds, W. 1985 Numerical experiments on the structure of homogeneous turbulence. Department of Mechanical Engineering Report TF-24, Stanford University, Stanford, CA.

Liou, T. & Santavicca, D. 1985 Cycle resolved ldv measurements in a motored ic engine. *Journal of fluids Engineering, Transactions of the ASME* **107**, 232.

Lipscomb, G., Denn, M., Hur, D. & Bogar, D. 1988 The flow of fiber suspensions in complex geometries. *Journal of Non-Newtonian Fluid Mechanics* **26**, 297.

McComb, W. D. 1990 Physics of Turbulence. Clarendon Press.

Mewis, J. & Metzner, A. 1974 The rheological properties of suspensions of fibers in Newtonian fluids subjected to extensional deformations. *Journal of Fluid Mechan-*

ics **62**, 593.

Nikuradse, J. 1933 Stromungsgesotze in rauhen Rohren. *Forsch. Arb. Ing. Wes.* **361**.

Okagawa, A. & Mason, S. 1973 The kinetics of flowing dispersions VII. Oscillatory behavior of rods and discs in shear flow. *Journal of Colloid Interfacial Science* **45**, 330.

Olson, J. & Kerekes, R. 1998 The motion of fibers in turbulent flow. *Journal of Fluid Mechanics* **377**, 47.

Olson, J. 2001 The motion of fibers in turbulent flow, stochastic simulation of isotropic homogeneous turbulence. *International Journal of Multiphase Flow* **27**, 2083.

Olson, J., Frigaard, I., Candice, C., & Hamalainen J. P. 2004 Modelling a turbulent fiber suspension flowing in a planar contraction: The one-dimensional headbox. *International Journal of Multiphase Flow* **30**, 51.

Papanastasiou, A. 1985 Fiber orientation in complex flow fields. AIChE Annual Meeting, Chicago.

Parsheh, M. 2001 Flow in contractions with application to headboxes. Ph.D. thesis, Royal Institute of Technology, Sweden.

Pittman, J. & Kasiri, N. 1992 Motion of rigid rod-like particles suspended in non-homogeneous flow fields. *International Journal of Multiphase Flow* **18**, 1077.

Prandtl, L. 1933 Attaining steady air stream in wind tunnels. *NACA Rept.* 726.

Ribner, H. & Tucker, M. 1952 Spectrum of turbulence in a contracting stream. *National Advisory Committee for Aeronautics - Technical Notes* 2606.

Roach, P. 1987 The generation of nearly isotropic turbulence by means of grids. *Heat and Fluid Flow* **8**, 82.

Rogallo, R. & Moin, P. 1984 Numerical simulation of turbulent flow. *Annual Review of Fluid Mechanics* **16**, 99.

Shaqfeh, E. & Fredrickson, H. 1990 The Hydrodynamic Stress in a Suspension of Rods. *Physics of Fluids A* **2**, 7.

Shaqfeh, E. & Koch, D. 1990 Orientation dispersion of fibers in extensional flows. *Physics of Fluids A* **7**, 1077.

151

Smook, G. 1992 *Handbook for pulp and paper technologists.* Angus Wilde Publications, Vancouver.

Squires, K. & Eaton, J. 1990 Particle response and turbulence modification in isotropic turbulence. *Physics of Fluids A* **2**, 1191.

Taylor, G.I. 1935 Turbulence in a contracting stream. *ZAMM.* **15**, 91.

Townsend, A. 1954 The uniform distortion of uniform turbulence. *Journal of Mechanics and Applied Mathematics* **7**, 104.

Tsuge, S. 1984 Effect of flow contraction on evolution of turbulence. *Physics of Fluids* **27**, 1948.

Tucker, H. & Reynolds, A. 1968 The distortion of turbulence by irrotational plane strain. *Journal of Fluid Mechanics* **32**, 567.

Tulapurkara, D. & Ramjee, V. 1980 Effect of contraction on screen generated turbulence. *Aeronautics Journal* **84**, 190.

Uberoi, M. 1956 Effect of wind-tunnel contraction on free-stream turbulence. *Journal of Aerosol Science* **23**, 756.

Uberoi, M. & Corrsin, S. 1953 Diffusion of heat from a line source in isotropic turbulence. *NACA Rept.* 1142.

Ullmar, M. & Norman, B. 1997 Observation of fiber orientation in a headbox nozzle at low consistency. *Engineering and Papermakers Conference* 865.

Ullmar, M. 1998 On Fiber Alignment Mechanisms in a Headbox Nozzle. Licentiate Thesis, Royal Institute of Technology.

Verieye, V. & Dupret, F. 1993 Prediction of fiber orientation in complex injection molded parts. *American Society of Mechanical Engineers, Applied Mechanics Division, AMD* **175**, 139.

Vincent, M. & Agassant 1986 Experimental study and calculations of short glass fiber orientation in a center gated molded disc. *Journal of Polymer Composites*, **7**, 76.

Westin, K., Boiko, A., Klingmann, B. & Alfredsson, P. 1994 Experiments in a boundary layer subjected to free stream turbulence, Part 1. Boundary layer structure and receptivity. *Journal of Fluid Mechanics* **281**, 193.

Yarin L. & Hetsroni G. 1994 Turbulent intensity in dilute two-phase flows. *International Journal of Multiphase Flow* **20**, 27.

Yuan Z. & Michaelides E. 1992 Turbulence modulation in particulate flows - a theoretical approach. *International Journal of Multiphase Flow* **18**, 779.

Zettner C. & Yoda E. 2001 Moderate-aspect-ratio elliptical cylinders in simple shear with inertia. *Journal of Fluid Mechanics* **442**, 241.

VITA

Matthew L. Brown was born on July 19, 1973 in Farmington, ME to Barry and Avis Brown. He attended Mt. Blue High School in Farmington, ME, graduating in 1991. His fondness of physics and chemistry in high school lead him to study chemical engineering at the University of Maine at Orono, from which he was awarded a Batchelor of Science in 1995. After working in industry after graduation, Matthew decided to further himself by moving to Atlanta where he attended the Institute of Paper Science & Technology and received a Masters degree in 1998. Shortly after starting his doctoral studies at the Georgia Institute of Technology, Matthew married Liza Del Rosario on December 7, 1999. The two joyfully welcomed their son Luke into their family on August 16, 2003. In the Spring of 2005, he was awarded a Doctorate of Philosophy in Chemical Engineering. Upon graduation, his family relocated to Mehoopany, PA where he started his engineering career with Proctor & Gamble.